Stern-Gerlach Matter-Wave Interferometry

By

Or Dobkowski

Thesis submitted in partial fulfillment
of the requirements for the degree of
"DOCTOR OF PHILOSOPHY"

Submitted to the Senate of Ben-Gurion University of the Negev
March 2025
Beer-Sheva

Stern-Gerlach Matter-Wave Interferometry

By

Or Dobkowski

Thesis submitted in partial fulfillment
of the requirements for the degree of
"DOCTOR OF PHILOSOPHY"

Submitted to the Senate of Ben-Gurion University of the Negev

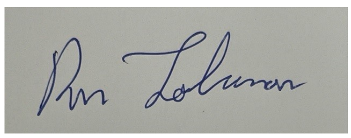

Signature of advisor: ____________________

Signature of Dean of the Kreitman School of Advanced Graduate Studies: ____________________

March 2025

Beer-Sheva

This work was carried out under the supervision of Prof. Ron Folman

In the Department of Physics

Faculty of Natural Sciences

Research-Student's Affidavit when Submitting the Doctoral Thesis for Judgment

I, Or Dobkowski, whose signature appears below, hereby declare that:

I have written this Thesis by myself, except for the help and guidance offered by my Thesis Advisors.

The scientific materials included in this Thesis are products of my own research, culled from the period during which I was a research student.

This Thesis incorporates research materials produced in cooperation with others, excluding the technical help commonly received during experimental work. Therefore, I am attaching another affidavit stating the contributions made by myself and the other participants in this research, which has been approved by them and submitted with their approval.

Date: 16.03.2025
Student's name: Or Dobkowski
Signature: ____אור____

Affidavit stating the contributions made by myself and by other participants in this research

I, Or Dobkowski, whose signature appears below, hereby declare that the scientific materials included in this Thesis are products of my own research, except for the following parts, which were produced in cooperation with others:

- The data taking for Ch. 4 was done in cooperation with Barak Trok.
- The data taking for Ch. 5, 6 was done in cooperation with Barak Trok and Peter Skakunenko
- The theory in Ch. 2 was done in cooperation with Yonathan Japha.
- The numerical simulations in Ch. 5, 6 were done Yonathan Japha.

Date: 16.3.2025	Name: Or Dobkowski	Signature:	
Date: 20.3.2025	Name: Barak Trok	Signature:	ברק טרוק
Date: 20.3.25	Name: Peter Skakunenko	Signature:	
Date: 20.3.25	Name: Yonathan Japha	Signature:	יונתן יפה

Abstract

The human effort to understand nature and the physical laws that describe it is a profound drama, featuring both humans and natural phenomena as main characters. One cannot tell this story without mentioning the phenomenon of free-falling objects – whether allegedly dropped from the Leaning Tower of Pisa or falling on the head of a man who will redefine physics.

Galileo's investigations of free-falling objects marked a pivotal moment in the quantitative analysis of motion. Newton's law of gravity is one of the most significant generalizations made bridging the earthly experiences of humans and the skies above. Years later, Albert Einstein, in his effort to extend special relativity to a general theory, experienced a breakthrough when imagining a person in free fall, leading to the realization that the individual would not perceive his own weight[1]. This insight led to the formulation of the equivalence principle, which underpins the general theory of relativity.

Another dramatic chapter unfolded with the birth of quantum mechanics, which predicts that massive particles possess wave properties, can be assigned a wavelength, and can be described by a wave function. The theory predicts that these so-called matter waves should exhibit the wave phenomena of superposition, resulting in constructive and destructive interference, depending on the relative phase of the parts of the superposition.

[1] "The breakthrough came suddenly one day. I was sitting on a chair in my patent office in Bern. Suddenly a thought struck me: If a man falls freely, he would not feel his weight. I was taken aback. This simple thought experiment made a deep impression on me. This led me to the theory of gravity." - Einstein, 1922 [1]

The phenomenon of matter-wave interference was first demonstrated in 1927 by electron diffraction experiments by G. P. Thomson and A. Reid (Diffraction of Cathode Rays by a Thin Film [2]) and Clinton Davisson and Lester Germer (Diffraction of Electrons by a Crystal of Nickel [3]). Later technological advancements led to the development of matter-wave interferometers, in which a matter-wave is split into two or more coherent beams, later recombined, resulting in interference. Matter-wave interferometers, and particularly atom interferometers, have enabled a range of technological applications and explorations of fundamental physics [4, 5].

Surprisingly, despite the rich history of matter-wave experiments and the many efforts to unite the theory of gravity with quantum mechanics, the quantum phase of a freely falling massive particle has yet to be directly measured.

In this work, we present a novel atom-interferometer that measures the phase accumulation of a freely falling particle. The interferometer is based on the Stern-Gerlach effect, leveraging a decade of Stern-Gerlach interferometry experiments in which the necessary techniques were developed [6]. The interferometer operates with ultra-cold atoms, coherently split into a superposition of free-fall and rest, using a set of magnetic gradients and microwave pulses.

At the core of the experiment is the atom chip [7–10], composed of nano-fabricated current-carrying wires. The atom chip enables fast and accurate control over the magnetic fields and serves two key functions. First, it provides the fast and accurate modulation of the magnetic field gradients required for the interferometer. Second, it ensures the precise preparation of atoms, including stable trapping, controlled release, and the collimation of the atom's expansion once released from the trap.

We are hopeful that this new experiment and its results will serve as a significant tool in probing the interface of quantum mechanics and gravity; for example, it was hypothesized that this phase is the manifestation of the equivalence principle in quantum mechanics [11] and is suggested as a probe of quantum gravity [12]. Beyond our measurement, we hope that the introduction of this new experimental scheme will serve as a base for further investigations of fundamental questions.

The thesis is organized as follows:

Ch. 1: Introduction to matter-wave interferometry and to the Stern-Gerlach interferometer.

Ch. 2: Theoretical background of the Stern-Gerlach interferometer and key experimental techniques used in this work

Ch. 3: An outline of the experimental apparatus, including the upgrades introduced during my PhD.

Ch. 4: An outline of the experimental procedure for achieving a Bose-Einstein condensation (BEC).

Ch. 5: The main result of this work - measurement of the quantum phase of a freely falling mass.

Ch. 6: Detailed description of the main result - both the experimental and theoretical aspects.

Publications

- O. Dobkowski, B. Trok, P. Skakunenko, Y. Japha, D. Groswasser, M. Efremov, C. Marletto, I. F. Guridi, R. Penrose, V. Vedral, W. P. Schleich, and R. Folman, "Observation of the quantum equivalence principle for matter-waves", arXiv preprint arXiv:2502.14535 (2025) [13].
- O. Amit, O. Dobkowski, Z. Zhou, Y. Margalit, Y. Japha, S. Moukouri, Y. Meir, B. Horovitz, and R. Folman, "Anomalous periodicity in superpositions of localized periodic patterns," New J. Phys. **24**, 073032 (2022) [14].
- Y. Margalit, O. Dobkowski, Z. Zhou, O. Amit, Y. Japha, S. Moukouri, D. Rohrlich, A. Mazumdar, S. Bose, C. Henkel, and R. Folman,"Realization of a complete Stern-Gerlach interferometer: Toward a test of quantum gravity" Science Advances **7**, eabg2879 (2021) [15].

Acknowledgments

I would like to thank the many people who have supported me throughout my journey in experimental physics and the completion of this thesis.

First and foremost, I express my deepest gratitude to my advisor, Prof. Ron Folman, for his unwavering support and encouragement throughout my doctoral research. Ron kept pushing me forward through the ups and downs of life and research and, most importantly, he put a "big red circle" around the most important goals of our research and my PhD.

I am deeply grateful to my colleagues in the Atom Chip group, with whom I had the pleasure of working, and to the members of BEC2 team who worked with me shoulder to shoulder—quite literally—at our experimental control desk and optical table. Yair, for passing on the BEC2 tradition and being both a great friend and mentor. We worked together in the lab for only a year, but our discussions and collaborations extended far beyond. Zhifan, for our joint work during my first year in the lab. Omer, for his hard work and dedication, and for being a great colleague throughout my M.Sc. Dima Kapusta for his contributions during his time at BGU. Barak and Peter, the final year of my PhD has been an adventure, and I had the privilege of sharing it with the best team I could have asked for. The results presented in this thesis would never have been possible without you.

Yaniv, for the days and nights of hard work and for bringing a unique perspective to every challenge we faced. Sergey Popov, for his help with the 2D-MOT assembly and for solving any technical challenge presented - with passion and precision. Zina Binshtok, for her incredible mastery of electronics, without which our experiments would not have been possible. Mark Keil, for his kind advice and mentoring on the challenges of science and life; this meant a lot. David Groswasser, for being in the right place at the right time, which changed the course of my PhD for the better. Yoni Japha, for the many hours of discussions, invaluable numerical simulations, and brutal honesty when examining any idea or result. Maxim Efremov, for many exciting discussions. Shraga Reznick, my first physics teacher, who showed me the beauty of physics.

Finally, I would like to thank my family. My partner, Dafna, for her unwavering love and support, and my son, Guy, for bringing me many hours of joy and happiness. To my parents, whose love and support shaped my childhood and who always prioritized the education and development of their children above all – I am forever grateful.

Contents

List of Figures

Abbreviations

MOT	magneto-optical trap
BEC	Bose-Einstein condensate
SG	Stern-Gerlach
SGI	Stern-Gerlach interferometer
COM	center of mass
DKC	delta-kick cooling
TOF	time-of-flight
MW	microwave
UHV	ultra-High Vacuum
NEG	Non Evaporable Getter
AOM	acousto-optic modulator
ECDL	external cavity diode laser
PLL	phase-lock loop
NA	numerical aperture
OD	optical density
RF	radio frequency
QGI	Quantum Galileo Interferometer
DD	dynamical decoupling
SEM	standard error of the mean
SOZ	second order Zeeman
STD	standard deviation
GP	Gross-Pitaevskii
NMR	nuclear magnetic resonance
TF	Thomas-Fermi

Chapter 1

Introduction

1.1 Cold atoms and atom interferometry

The field of cold atoms has undergone rapid evolution since the first demonstration of laser cooling of neutral atoms in 1982 [16]. This breakthrough paved the way for numerous advances in atomic physics. Another pivotal milestone was the invention of the magneto-optical trap (MOT)[1] [20], which provided an efficient method for cooling and confining neutral atoms using laser light and magnetic fields. In 1995, the field reached another major breakthrough with the first realization of Bose-Einstein condensation (BEC) in dilute atomic gases [22, 23]. Today, cold atom experiments have a wide range of applications, from precision metrology and tests of fundamental physics [24, 25] to quantum technologies [26] and quantum computing [27, 28]. They extend beyond traditional laboratory settings to experiments conducted in microgravity environments such as sounding rockets [29] and the Cold Atom Laboratory aboard the International Space Station [30]. Ongoing

[1] An interesting anecdote - according to David Pritchard (in this video [17]), the idea that atoms can be trapped with photon pressure came about due to a question from a curious student, E.L. Raab, after a lecture by Alain Aspect. In the lecture, Aspect explained that atoms could not be trapped by photon pressure due to the optical Earnshaw theorem [18]. As Pritchard explained the theorem to the student, he found a loophole: atoms are not spherically symmetric spheres, and their spin can be used to control their interaction with the laser light [19]. The authors of [20] give credit to Jean Dalibard for "for giving us the seminal idea for this trapping scheme", and the common wisdom credits Dalibard for the invention of the MOT [21].

advancements in cold atom physics promise further contributions to fundamental science and emerging quantum technologies.

1.2 Matter-wave interferometry

Interferometers have long played a crucial role in our investigation of nature and physical phenomena. Particularly famous interferometer experiments range from Young's double slit experiment that explored the wave-like nature of light to the Michelson-Morley experiment, with its brave attempt to measure the Earth's movement in the "luminiferous aether". The Michelson-Morley experiment was one of the experimental foundations of special relativity. Its ultimate extension in the modern era is the Laser Interferometer Gravitational-Wave Observatory (LIGO), a large-scale experiment designed to detect gravitational waves. LIGO successfully confirmed Einstein's predictions a century after the introduction of the theory of general relativity. The leap from optical interference to matter-wave interference occurred around 1924, when the de Broglie hypothesis was confirmed by the Davisson-Germer experiment which demonstrated the wave properties of electrons, exhibiting a diffraction pattern similar to that observed in X-ray scattering experiments. Atom interferometers were first developed in the 1990s by using microfabricated matter gratings [31, 32], and laser light [33] as beam splitters. Nowadays, atom interferometers are commonly used for research in the field of quantum mechanics and in precision measurements of gravity [34], fundamental constants [35], as accelerometers for inertial guidance, and many additional applications. A detailed review of atom interferometry can be found in [4, 36], and an extensive list of applications of matter-wave interferometers can be found in [37].

1.3 Review of the Stern-Gerlach interferometer

In 1922 Walther Gerlach and Otto Stern published their results on "The experimental proof of directional quantization in the magnetic field", which is now famously known as the Stern-Gerlach (SG) experiment [38]. In the experiment, a collimated beam of silver atoms passed through a region with a strong magnetic gradient. The results showed a splitting into two distinct beams, providing clear evidence of the quantization of the magnetic dipole of the atom. The SG experiment contributed to the discovery of quantum mechanical spin, the intrinsic angular momentum of particles. While the SG experiment demonstrated the splitting of an atomic beam into two distinct beams, it did not demonstrate the coherence of the splitting process; to prove coherent superposition, one has to show an interference signal, by realizing an interferometer.

The idea of an atom interferometer based on the SG effect was envisioned soon after the birth of quantum mechanics. For example: in 1951, David Bohm suggested using permanent magnets to create four regions of magnetic gradients to split, stop, reverse, and recombine the wave packets in a setup analogous to a Mach-Zehnder interferometer. Bohm mentioned that such a device would require “fantastic” accuracy [39]. Englert, Schwinger, and Scully analyzed the concept of a SGI in more detail and coined it the “Humpty-Dumpty” effect [40–42] to emphasize that exceptional precision would be required to split and recombine the wave packets coherently. While these analyses labeled the SGI as an impossible or formidable challenge, advancements in the field of cold atoms - mainly the production of BECs and the development of the atom chip - have made the realization of the SGI feasible. The demonstration in our group of coherent Stern–Gerlach momentum splitting on an atom chip [43] launched a decade of Stern-Gerlach interferometry experiments. A review of the Stern-Gerlach interferometer (SGI) experiments with the atom chip can be found in [6].

The SGI experiments can be divided into two main categories according to the experimental scheme and the output: (A) The “half-loop” SGI, whose output is a spatial interference pattern, and (B) The “full-loop” SGI, whose output is spin population. The first can be viewed as the atomic analog of the double-slit experiment, while the second can be viewed as the atomic analog of the Mach-Zehnder interferometer[2].

[2]The division into the two categories is not fundamental but practical, as both schemes can be engineered to produce the two kinds of outputs. For example, in the full-loop SGI, each output port can exhibit a spatial interference pattern, again in analogy to the optical Mach-Zehnder interferometer.

In this work, we present a new variation of the full-loop SGI; nonetheless, to provide a complete overview, we also include a short review of the half-loop SGI in the next section, as it was a crucial step in developing the full-loop SGI.

1.3.1 Half loop – spatial fringes

The half-loop SGI is an atomic analog of the double slit experiment, first splitting the wave packets, then stopping their acquired momentum after some propagation time, and finally allowing them to expand until they overlap and exhibit a spatial interference pattern produced by the interference of two wave packets having the same spin. The spatial interference fringe pattern contains information about the visibility, periodicity, and phase of the interferometer. The coherence of the SG splitting is demonstrated not only by the spatial interference pattern but also by the phase stability of the interferometer. This is crucial - not just in order to estimate the experimental drifts of the setup, but particularly when using a BEC, because a BEC can produce randomly positioned fringes even with non-coherent splitting. A detailed analysis of the stability of the Stern-Gerlach spatial fringe interferometer is given in [44], demonstrating the high phase stability of atom chip-based SGI, with a multi-shot fringe visibility of 90%.

Extending the spatial fringe SGI to include clock interferometry allowed for explorations of fundamental physics. By placing each of the two wave packets in a clock state, it was demonstrated that the "ticking" rate of the clocks gives rise to "which path" information, affecting the fringe visibility [46]. Such a setup also measured the quantum complementarity of clocks [47], extending the known quantum complementarity relation for visibility and distinguishability $V^2+D^2 \leq 1$ [48] where V is interference pattern visibility and D is the distinguishability of the two paths of the interfering particle. In an experiment where the proper time is a "which path" witness, the clock complementarity relation becomes $V^2 + (C \cdot D_I)^2 \leq 1$ where D_I is the ideal clock distinguishability of the paths, determined by the different ticking rate in the two paths of the clock, and $0 \leq C \leq 1$ is the clock quality, whereby D_I is due to the gravitationally induced red-shift of general relativity, and C is due to the quantum preparation of the two-level clock.

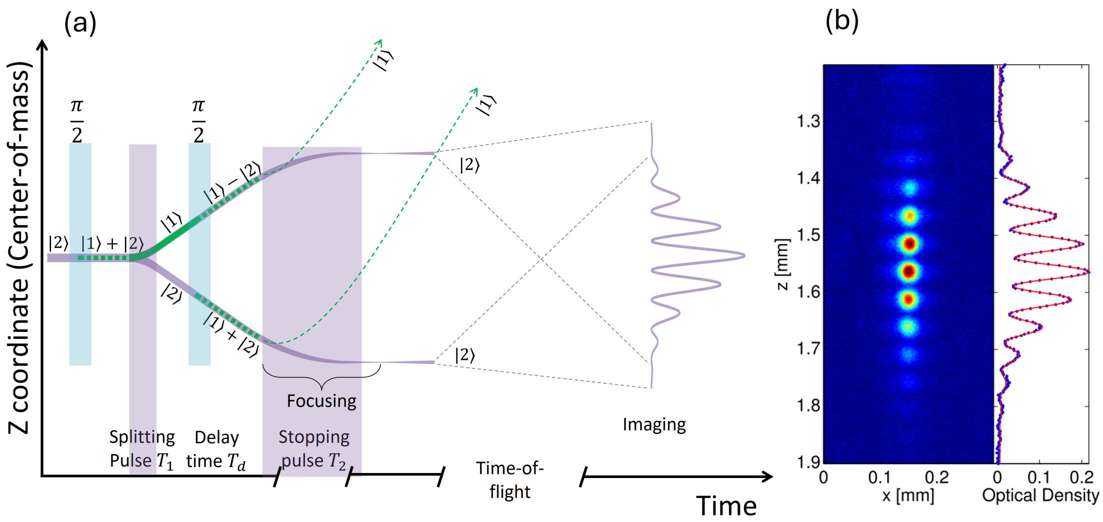

Figure 1.1: Half-loop SGI: (a) The experimental scheme: The initial wave packet is put in a superposition of two spin states by a $\pi/2$ Rabi pulse. The wave packet is then split into two arms by a magnetic gradient pulse. A second $\pi/2$ pulse puts each arm again in a superposition of the two spin states. The two arms are then stopped by a second magnetic gradient pulse, and the wave packets are allowed to expand freely. The final state of the wave packet is measured by absorption imaging. We note that due to the curvature of the magnetic field forming the magnetic gradient pulse, the long pulse also focuses the wavepackets, as depicted in the figure. (b) Spatial interference pattern from the half-loop SGI. A multi-shot image made by averaging 40 consecutive interference images using a BEC (no correction or post-selection) with a normalized visibility of 99%. (a) Adapted from [44], under license CC BY 3.0. (b) Adapted from [45].

During the late stages of my MSc and the early stages of my PhD, I was the co-author (with equal contribution) of a paper on the "Anomalous periodicity in superpositions of localized periodic patterns," where the periodicity of two overlapping spatial fringes originating from the interference of four wave packets was studied [14]. Surprisingly, the periodicity of the fringes was found to be discontinuous and piecewise rigid when scanning the central parameter of the system. While the data taking and analysis of these results were a significant endeavor, this finding was not the main focus of my PhD, and I do not include a detailed description of it in this thesis. The reader is referred to the paper itself for more details. The maturity of these and other [49] half-loop SGI experiments has paved the way for exploring the full-loop SGI (from now on referred to as the SGI).

Chapter 2

Theoretical background

In this chapter, we describe the theoretical background of the Stern-Gerlach interferometer (SGI) and the equations governing the phase evolution of wave packets in linear and quadratic potentials. Next, we provide the background of key experimental techniques used in this work: the 2D magneto-optical trap, delta-kick cooling, and microwave transitions in the ^{87}Rb atom. The background on other experimental techniques of cooling and trapping of atoms is well documented [7, 10, 50, 51], and the reader is referred to these sources or the theses of our group members for further details [52–54].

2.1 Theoretical framework for the Stern-Gerlach interferometer

2.1.1 Building blocks of the Stern-Gerlach interferometer

The SGI requires two fundamental components: (1) A particle that can be put in a superposition of two spin states and (2) a set of magnetic gradients to split and recombine the trajectories of the two spin states.

To describe the equations of the SGI, we name the two spin states $|1\rangle$ and $|2\rangle$ (not to be confused with the Zeeman sub-levels $m_F = 1, 2$). Let's assume we start with the particle at state $|1\rangle$ with some initial wave packet shape $\psi(\mathbf{r}, t = 0)$. We first create a superposition of the two states by applying a $\pi/2$ Rabi pulse and get

$$|\psi\rangle = \psi(\mathbf{r})\frac{1}{\sqrt{2}}(|1\rangle + |2\rangle)\,. \tag{2.1}$$

We then apply the magnetic gradients to manipulate the momentum and position of the wave packets. The wavefunction throughout the propagation in the interferometer is a superposition of two different spatial wave packets evolving separately along the interferometer arms

$$|\psi(\mathbf{r},t)\rangle = \frac{1}{\sqrt{2}}[\psi_1(\mathbf{r},t)|1\rangle + \psi_2(\mathbf{r},t)|2\rangle]. \tag{2.2}$$

After the magnetic gradients are applied we apply a second $\pi/2$ pulse, and get

$$|\psi(\mathbf{r},t_f)\rangle = \frac{1}{2}[\psi_1(\mathbf{r},t_f)(|1\rangle - |2\rangle) + \psi_2(\mathbf{r},t_f)(|1\rangle + |2\rangle)]. \tag{2.3}$$

At this stage, we can measure the population in the $|1\rangle$ state. From a mathematical perspective, a measurement of the population requires projection of the wavefunction onto state $|1\rangle$, which gives

$$\langle 1|\psi(\mathbf{r},t_f)\rangle = \frac{1}{2}[\psi_1(\mathbf{r},t_f) + \psi_2(\mathbf{r},t_f)] \tag{2.4}$$

and the measured population, i.e., fraction of atoms in the $|1\rangle$ state, is

$$P_1 = \int d^3\mathbf{r}\,|\langle 1|\psi(\mathbf{r},t_f)\rangle|^2 = \frac{1}{4}\int d^3\mathbf{r}\,(|\psi_1|^2 + |\psi_2|^2 + \psi_1^*\psi_2 + \psi_1\psi_2^*). \tag{2.5}$$

The wavefunctions ψ_1 and ψ_2 are normalized, so that

$$\int d^3\mathbf{r}\,|\psi_1|^2 = \int d^3\mathbf{r}\,|\psi_2|^2 = 1 \tag{2.6}$$

Plugging this into Eq. 2.5 we get

$$P_1 = \frac{1}{4}\left[2 + \int d^3\mathbf{r}\,(\psi_1^*\psi_2 + \psi_1\psi_2^*)\right], \tag{2.7}$$

which gives

$$P_1 = \frac{1}{2}\left[1 + V\cos(\Delta\phi)\right], \tag{2.8}$$

where

$$Ve^{-i\Delta\phi} = \int d^3\mathbf{r}\,\psi_1^*(\mathbf{r},t_f)\psi_2(\mathbf{r},t_f) \tag{2.9}$$

is the overlap integral. Here, V is the spin population fringe visibility, and $\Delta\phi$ is the interferometric phase. To predict the output of the SGI, we need to calculate the wave packet evolution in the interferometer arms and evaluate the overlap integral in Eq. 2.9. The experimental scheme of the full-loop SGI, as described above, is shown in Fig. 2.1.

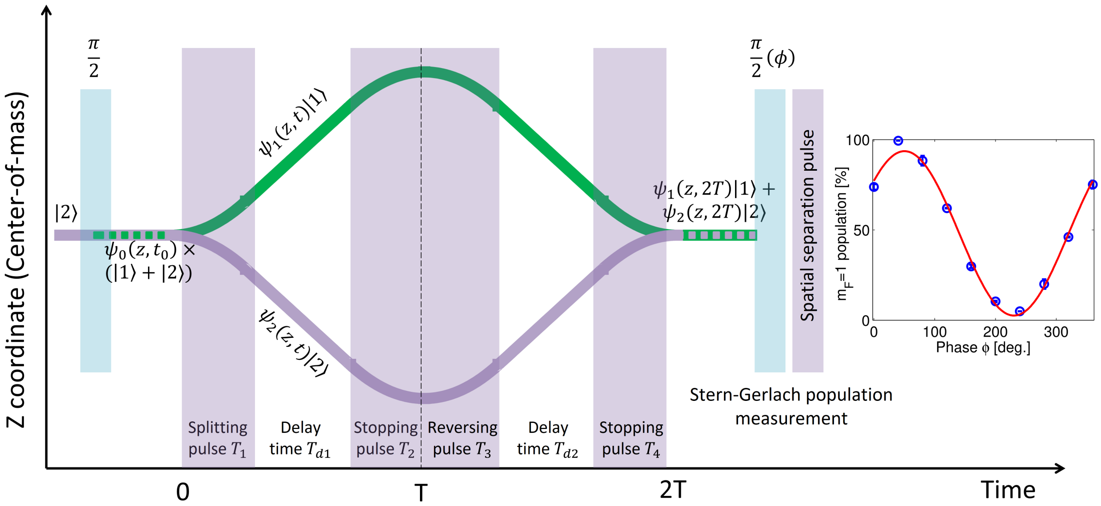

Figure 2.1: Experimental scheme of a full-loop SGI: A $\pi/2$ Rabi pulse prepares the atoms in a superposition $(|1\rangle+|2\rangle)$ of the two spin states. Magnetic gradient pulses from the atom chip (whose durations are labeled T_1, T_2, T_3, T_4) split the wave packet into a superposition of two trajectories, later stop and reverse the relative momentum, and finally recombine the parts of the superposition in momentum and position. Delay time between the gradient pulses (T_{d1}, T_{d2}) allows control of the spatial separation of the two wave packets. Finally, a $\pi/2$ pulse is applied, followed by a population measurement. Scanning the phase of the $\pi/2$ pulse results in spin population fringes, i.e., oscillations in the spin population, as seen in the inset, where the data in blue is fitted to a sine function (red). The spin population oscillations also appear when scanning a parameter that affects the phase difference between the two arms. This scheme is the most basic one for a full-loop SGI, while different combinations of Rabi pulses and magnetic gradients can create variations of the SGI. Taken from [55].

In this work, we use two models to calculate a prediction for the output of the SGI. The first model, described in Sec. 2.1.2, is used in the numerical simulations in Ch. 5 ,6 to calculate the phase and visibility expected in the experiment. The model provides a numerical solution for the wave packet parameters, including its shape and phase, and takes into account atom-atom interactions and curvatures of the potential. The second model described in Sec. 2.1.3 assumes time-dependent linear potentials and is used to derive the analytical prediction for the phase of the experiment. In the second model, the phase is not affected by the wave packet shape.

2.1.2 Unified model of wave packet evolution

Here we give a short description of the theoretical framework for calculating the output of the SGI in the numerical simulations presented in this work. This section is based on the model presented by Dr. Yonathan Japha in [56]. The model unifies the limits of weakly interacting atoms, described by a Gaussian wave packet, and strongly interacting atoms, described by the Thomas-Fermi approximation, into one parametric framework. The model shows excellent agreement with precise numerical calculations given by the Gross-Pitaevskii equations.

We divide our description of the framework into three main parts. First, we describe the wave packet parameters. Second, we describe the wave packet evolution in a locally quadratic potential. Third, we show how these equations can be used to predict the visibility and phase of the SGI.

The wave packet

The problem of wave packet evolution in the SGI can be separated into the evolution of the wave packet center position and momentum, and the evolution of the wave packet relative to the center, (such decoupling of the center of mass (COM) motion and the wave packet shape is possible as long as the potential is at most quadratic [57], or in our case, is locally quadratic over the scale of the wave-packet size). Thus we can write the wave packet as:

$$\psi(\mathbf{r},t) = e^{i[\mathbf{P}\cdot(\mathbf{r}-\mathbf{R})+S(t)]/\hbar}\Phi(\mathbf{r}-\mathbf{R},t), \tag{2.10}$$

where $\mathbf{R}$ is the COM position, $\mathbf{P} = m\dot{\mathbf{R}}$ is the COM momentum, $S(t)$ is the action along the classical trajectory of the COM, and $\Phi(\mathbf{r},t)$ represents the wave packet shape around its center, and can be written as [58]

$$\Phi(\mathbf{r},t) = |\Phi(\mathbf{r},t)| \exp\left[\frac{i}{2}\sum_j \alpha_j(t) r_j^2 + i\varphi_{\text{internal}}(t)\right] , \tag{2.11}$$

where $r_j (j = 1, 2, 3) = x, y, z$ are the Cartesian coordinates centered at the COM. Here, the first term in the exponent is the quadratic phase of the wave packet around the center due to expansion or focusing, and the second term is an internal global phase. The wave-packet COM and shape dynamics depend on the spin state at any given time along each of the interferometer arms. Overall, at any time t, the wave packet can be described by the following parameters:

- The spin state $|F, m_F\rangle$,
- The position of the center of mass $\mathbf{R}_j = (X, Y, Z)$.
- The velocity of the center of mass $\dot{\mathbf{R}}_j = (\dot{X}, \dot{Y}, \dot{Z})$.
- The width of the wave packet in each axis $\sigma_j = (\sigma_x, \sigma_y, \sigma_z)$,
- The rate of change of the wave packet widths in each axis $\dot{\sigma}_j = (\dot{\sigma}_x, \dot{\sigma}_y, \dot{\sigma}_z)$
- The global phase of the wave packet $\varphi(t) = S(t)/\hbar + \varphi_{\text{internal}}(t)$ (the phase can be expressed in terms of an integral over time of the previous parameters as we show in the next section).

Here we restrict the discussion to a model that does not include rotations. The full theory, including rotations (which was used in the simulation), is not yet published and will be detailed elsewhere in the future. Nonetheless, to provide a broader overview, we include a brief description of the wave packet in the model that includes rotations.

- The wave packet shape is initially defined by three size parameters $\sigma_i = \left[\int d^3\mathbf{r}\, r_i^2 |\Phi(\mathbf{r},t)|^2\right]^{1/2}$ for $i = 1, 2, 3$ being the axes of the trapping potential.
- Once released from the trap, the wave packet evolves with more general size parameters matrix $\Lambda_{ij}(t)$ such that $\lambda_{ij}(0) = \sigma_i^{-2}\delta_{ij}$ but later evolution allows off-diagonal components of Λ_{ij} that represent the rotation of the wave packet.

A treatment of rotations of a BEC can also be found in [57].

The wave packet evolution in a quadratic potential

We take a locally quadratic approximation for the potential.

$$V(\mathbf{r},t) \approx V(\mathbf{R},t) + \sum_j V_j'(\mathbf{R},t)\,(r_j - R_j) + \frac{1}{2}\sum_j V_j''(\mathbf{R},t)\,(r_j - R_j)^2\,, \quad (2.12)$$

where

$$V_j' = \frac{\partial V}{\partial r_j}; V_j'' = \frac{\partial^2 V}{\partial r_j^2} \quad (2.13)$$

In a quadratic potential, the wave packet preserves its general shape and particularly retains its Gaussian shape if initially it is a Gaussian. The wave packet evolution is governed by the following equations:

The center of mass position and velocity follow Newton's equations of motion

$$m\ddot{R}_j = -V_j'(\mathbf{R},t) \quad (2.14)$$

The widths of the wave packet and their time derivatives evolve due to "free expansion", the atom-atom interaction, and the local curvatures of the potential:

$$\ddot{\sigma}_j = \frac{\hbar^2}{4m^2}\left(\frac{1}{\sigma_j^3} + \frac{\beta a_s N}{\sigma_j\sigma_x\sigma_y\sigma_z}\right) - \frac{V_j''(\mathbf{R},t)}{m}\sigma_j, \quad (2.15)$$

where $\beta = 60/7^{5/2} = 0.4628$, and $a_s = 5.29$ nm is the s-wave scattering length of ^{87}Rb, and N is the total number of atoms. The Rb^{87} mass is $m = 1.44\times10^{-25}$ kg.

The global phase of the wave packet is divided into a phase related to the COM coordinates and a phase that depends on the internal dynamics of the wave packet (relative to the COM). The phase related to the COM is given by the action along the classical trajectory of the COM:

$$\varphi_{\text{action}}(t) = \frac{1}{\hbar}S(t) = \frac{1}{\hbar}\int_0^t \left[\frac{1}{2m}\mathbf{P}\left(t'\right)^2 - V\left(\mathbf{R}\left(t'\right),t'\right)\right]dt'\,, \quad (2.16)$$

The phase related to the internal dynamics of the wave packet around its COM is given by

$$\varphi_{\text{internal}}(t) = -\frac{1}{\hbar}\int_0^t \left[\tilde{\mu}(t') + \frac{1}{2}\sum_j \frac{\hbar^2}{2m\sigma_j(t')^2}\right]dt'\ , \quad (2.17)$$

where the first term is the potential energy due to the atom-atom interactions, which is proportional to the atomic density, and is given by $\tilde{\mu} = \frac{\hbar^2}{m}(a_{\rm S} N \beta)\frac{1}{\sigma_x \sigma_y \sigma_z}\frac{7}{8}$. The second term can be considered as the potential energy of the wave packet with regard to expansion around its center (related to the momentum uncertainty).

The evolution of the quadratic phase is given by

$$\alpha_j(t) = \frac{m}{\hbar}\frac{\dot{\sigma}_j}{\sigma_j}. \tag{2.18}$$

Overall, the phase of the wave packet includes a global phase given by Eqs. 2.16,2.17, a linear phase related to the momentum in Eq. 2.10, and a quadratic phase in Eq. 2.11, which is related to the wave packet expansion and given in terms of the wave-packet sizes and their time derivatives.

Given the above equations, calculating the evolution of a wave packet in the SGI requires knowledge of its initial state and the potential acting on it. In the case of the SGI, the potential is the sum of the magnetic and gravitational potentials. The initial state of the wave packet is determined by the trap properties and the number of atoms in the BEC, and is calculated using the model as presented in [56].

The overlap integral

The overlap integral (Eq. 2.9) is calculated by numerically integrating the wave packets of the two arms at the final time t_f. The absolute value of the overlap integral gives the visibility of the SGI, and the argument of the overlap integral gives the phase. While in some cases, the overlap integral can be calculated analytically (as in Eq.2.21 below), in the general case, it requires a numerical calculation.

In Ch. 5, we present the numerical simulations of the SGI using this model and compare the results with the experimental data.

2.1.3 Linear potential model

In the case of a linear potential, both wave packets evolve in the same way around their COM, so that the only difference between the two arms is the COM position and momentum. It can be shown that under this assumption the phase of the SGI depends only on the trajectories of the COM ([59] Sec. 3.3), and is given by

$$\Delta\phi = \frac{1}{\hbar}\Delta S - \frac{1}{\hbar}\mathbf{P}_{\text{avg}} \cdot \delta\mathbf{R}, \tag{2.19}$$

where $\Delta S = S_1 - S_2$ is the action difference between the two centers of the wave packets, $\delta\mathbf{R}$ is the spatial separation at time t_f, and

$$-\frac{1}{\hbar}\boldsymbol{P}_{\text{avg}} \cdot \boldsymbol{\delta R} \equiv \Delta\varphi_{\text{sep}} \ , \tag{2.20}$$

is the separation phase which appears if the two arms have some final spatial separation, and which depends on the average momentum of the two arms $\mathbf{P}_{\text{avg}}$.

The decomposition of the phase difference into the action and separation phase is not unique and depends on the frame of reference of the calculation; for example, in a frame of reference that moves with the average velocity of the final wave packets, the separation phase would vanish for any $\delta\mathbf{R}$, as $\mathbf{P}_{\text{avg}} = 0$. The action difference is also frame-dependent, such that the total phase is independent of the observer's frame [60].

It should be noted that while the expression for the separation phase in Eq. 2.20 is commonly used [60, 61], it is accurate only when both arms end with the same wave packet shape, and is therefore accurate only for the linear potential model. In other cases, the effect of imperfect recombination of the COM position of the two wave packets on the phase has to be calculated directly using the overlap integral.

In the case of a linear potential, calculating the phase of SGI requires only a calculation of the COM trajectories of the two arms. This model gives an analytical prediction for the phase of the SGI. In Ch. 5, we present this analytical prediction for the SGI phase and compare the results to the experimental data.

The visibility and the "Humpty-Dumpty" formula

The visibility is calculated from the absolute value of the overlap integral, which depends on the recombination of the two wave packets. The precision with which one has to recombine the wave packets is set by the spatial coherence length l_z and momentum coherence width l_p. These measures of coherence are inversely proportional to the momentum and position uncertainties of the atom, σ_p and σ_z, and may be defined as [15, 62]

$$l_z = \frac{\hbar}{\sigma_p}, l_p = \frac{\hbar}{\sigma_z}$$

where the momentum and position uncertainties satisfy the uncertainty relation $\sigma_p\sigma_z \geq \hbar/2$ (in this context, σ_z and σ_p are the uncertainties of the initial wave packet before the expansion of the cloud, and as long as linear potentials are used).

If the two paths at the output port of the interferometer (time $t = t_f$) are displaced by a distance $\Delta z(t_f)$, then the contrast is expected to drop as $V \propto \exp\left[-\frac{1}{2}\left(\Delta z(t_f)/l_z\right)^2\right]$. Equivalently, if the two paths are displaced in momentum by $\Delta p(t_f)$, then the contrast reduces as $V \propto \exp\left[-\frac{1}{2}\left(\Delta p(t_f)/l_p\right)^2\right]$.

A limiting case that gives insight into the visibility reduction is the case of two identical Gaussian wave packets with minimal uncertainty, separated by some final spatial splitting Δz and momentum splitting Δp at the time of measurement. In this case, we get that

$$V = \exp\left[-\frac{1}{2}\left(\frac{\sigma_p \Delta z}{\hbar}\right)^2 - \frac{1}{2}\left(\frac{\sigma_z \Delta p_z}{\hbar}\right)^2\right], \tag{2.21}$$

and using the minimal uncertainty relation $\sigma_p\sigma_z = \hbar/2$, we get

$$V = \exp\left[-\frac{1}{8}\left(\frac{\Delta z(t_f)}{\sigma_z}\right)^2 - \frac{1}{8}\left(\frac{\Delta p(t_f)}{\sigma_p}\right)^2\right], \tag{2.22}$$

which is known as the "Humpty-Dumpty" visibility formula [41].

For more information on the mathematical framework of atom interferometers in a linear potential, one can find in [63] a representation-free description of atom interferometers in time-dependent linear potentials and in [37] another mathematically rigorous description.

2.2 2D-MOT

2.2.1 Background - techniques for loading atoms to the MOT

The loading of atoms into a magneto-optical trap (MOT) requires a source of atoms in the form of increased vapor pressure of the desired atomic species or in the form of a cold atomic beam. Standard methods for increasing the vapor pressure include heating alkali dispensers, heating an oven containing a sample of the desired element, and light-induced atomic desorption (LIAD), in which UV light is used to induce atomic desorption from the walls of the chamber (mainly from the windows). Although these methods are easy to implement, each has its disadvantages and limitations. For example, heating alkali dispensers is a slow process, as it takes time to heat the dispensers, emit a sufficient amount of vapor, let the dispensers cool down, and pump the pressure back to its base value. In our setup, the process took 20 seconds, which is a typical time scale. Although fast modulation of alkali vapor pressure on the 100 ms scale was demonstrated in a small vacuum chamber with a volume of 290 ml [64], it was not manifested in the fast production of BECs. On the other hand, LIAD can modulate the pressure much faster, as shutting off a UV LED takes a few milliseconds, and the walls of the chamber act as a pump, reducing the vapor pressure within a few tens of milliseconds. LIAD works most efficiently on glass surfaces and is typically used in single-chamber experiments [65, 66]. The main challenge in using LIAD is keeping the reservoir on the walls saturated and finding a suitable dynamic equilibrium for the vapor pressure. Loading from a cold atomic beam requires a dual-chamber design and a few extra laser beams, but offers a significant improvement in the maximum attainable loading rate and reduced pressure in the main chamber, resulting in more atoms in the final MOT.

2.2.2 Background - equations of loading atoms to the MOT

The following rate equation describes the MOT loading dynamics:

$$\frac{dN}{dt} = \mathrm{R} - N\left(\gamma_{\mathrm{bg}} + \gamma_{\mathrm{Rb}}\right) - \beta_{\mathrm{la}} \int d^3r\, n^2(\mathbf{r}, t), \tag{2.23}$$

where R is the loading rate, $\gamma_{\text{bg}} = \frac{1}{\tau_{\text{bg}}}$ and $\gamma_{\text{Rb}} = \frac{1}{\tau_{\text{Rb}}}$ represent the loss rates due to collisions with the background gas and other rubidium atoms (with τ_{bg} and τ_{Rb} being the associated lifetimes), and β_{la} is the coefficient for light-assisted collisions.

When loading atoms from atomic vapor into the MOT, the loading rate is given by $\text{R} = \alpha P_{\text{Rb}}$, where α is a constant representing the MOT trapping cross-section and P_{Rb} is the partial pressure of ^{87}Rb. The loss rate due to rubidium collisions is given by $\gamma_{\text{Rb}} = \beta P_{\text{Rb}}$. Substituting these relations into Eq. 2.23 and neglecting light-assisted collisions, we obtain:

$$\begin{aligned}
&\frac{dN}{dt} = \alpha P_{\text{Rb}} - N\left(\beta P_{\text{Rb}} + \gamma_{bg}\right) \\
&N = N_S\left[1 - \exp\left(-t/\tau_L\right)\right] \\
&N_S = \frac{\alpha}{\beta}\left(1 - \gamma_b \tau_L\right); \frac{1}{\tau_L} = \beta P_{\text{Rb}} + \gamma_{bg} \ ,
\end{aligned} \tag{2.24}$$

where N_S is the steady-state number of atoms in the MOT, and τ_L is the characteristic loading time. From these expressions, we observe that while increasing P_{Rb} boosts the loading rate R, it also increases the loss rates, which limits the maximum number of atoms in the MOT, and the lifetime of the magnetic trap following the MOT. Typical loading rates R are around 10^7 atoms/s, with $N_S \approx 10^7 - 10^8$ atoms at a pressure range of 10^{-10} to 10^{-8} Torr, and a loading time of $5 - 20$ seconds.

When loading from a cold atomic source, such as a 2D-MOT, the flux Φ of cold atoms entering the MOT capture volume is introduced. In this case, the rate equation becomes

$$\frac{dN}{dt} = \Phi - N\left(\frac{1}{\tau_{\text{bg}}} + \frac{1}{\tau_{\text{Rb}}}\right) - \beta \int d^3r\, n^2(\mathbf{r}, t). \tag{2.25}$$

Since Φ can be increased without significantly raising the pressure, this approach allows for shorter loading times and a larger number of atoms in the MOT. Typical values of Φ range from 10^8 to 10^{10}, resulting in N_S values of $10^8 - 10^{10}$ atoms in the MOT. Thus, loading from a 2D-MOT leads to reduced loading times, increased atom numbers in the MOT, and lower pressure in the 3D-MOT chamber. Consequently, we have incorporated a homemade 2D-MOT into our setup, increasing the loading rate by a factor of 50 and the number of atoms in the MOT by a factor of 6, as described in Sec. 3.4.

2.3 Delta-kick cooling

The coherence length of a wave packet is given by $l_z = \frac{\hbar}{\sigma_p}$ [44]. This means that it is possible to increase the coherence length l_z by reducing the momentum spread, which amounts to cooling a thermal atomic cloud or collimating a wave packet. While evaporative cooling involves a loss of atoms and cannot reduce momentum uncertainty below the uncertainty limit of the ground state in the trap, it is possible to exploit the lensing effect of a harmonic potential to further cool the atoms or, rather, collimate them without a significant loss of atoms. This method, known as delta-kick cooling (DKC) [67], has been shown to achieve lensing and collimation, reducing the momentum width σ_P of atomic clouds [67–69]. Temperatures as low as tens of pico-Kelvin have been reported in [70–72].

The principle of DKC is as follows: Applying a harmonic potential with frequency ω_k, for a short duration τ_k, will act as a focusing lens, with a focal time given by $\tau_f = \frac{1}{\omega_k^2 \tau_k}$ such that the classical trajectories of atoms expanding from a single point for a duration τ_f become parallel (collimated) after the pulse. As the initial size of the atomic cloud is not zero, the cloud is not perfectly collimated, but its momentum spread is reduced by a factor $\sigma_z^i / \sigma_z(\tau_f)$ [73] where σ_z^i is the initial size of the cloud and $\sigma_z(\tau_f)$ is the size when the DKC is applied.

This implies that to achieve good collimation of the atomic cloud, three conditions should be met. The first is sufficient expansion, as DKC depends on the correlation between position and momentum that arises from the expansion of the atomic cloud. Assuming that the rate of expansion is constant, this condition can be written as

$$\sigma_v \cdot \mathrm{TOF} \gg \sigma_z^i, \tag{2.26}$$

where σ_v is the velocity spread of the atomic cloud, TOF is the time-of-flight (TOF) from the trap release to the DKC pulse (not necessarily equal to τ_f), and

σ_z^i is the initial spread in the wave-packet position. As the ratio of the final size to initial size increases, the correlation between position and momentum improves, allowing a greater degree of cooling [73]. Thus, DKC benefits from a long TOF and a small initial atomic cloud size.

In our experiment, the TOF is limited to one or two milliseconds, as the atoms freely fall away from the chip. On the other hand, the size of the atomic cloud can be decreased, for example, by adiabatically compressing the trap before its release or by loading the atoms to the magnetic trap on the atom chip, giving rise to high trap frequencies.

A different approach for achieving fast expansion rates is to apply a potential that has a focusing effect as in [46], after which comes fast expansion. In recent work, such an approach was used to realize a magneto-optical matter-wave telescope [74] by applying a diverging magnetic matter-wave lens followed by a collimating optical matter-wave lens.

We achieved efficient DKC in our experiment by loading the atoms to the atom chip trap, which has a trap frequency of $\omega \approx 2\pi \times 1\,\mathrm{kHz}$, and allowing a TOF of $\sim 1\,\mathrm{ms}$. While these numbers do not satisfy Eq. 2.26, the DKC is still effective. This is because the initial expansion of the BEC's wave packet is not constant but accelerated, due to the atom-atom interactions. After the short accelerated expansion, the wave packet is equivalent to one that started from an initial size much smaller than the minimal uncertainty wave packet size in the same harmonic trap. Effectively, the size after 1 ms of expansion is much larger than the initial "effective" size even though $\omega \cdot \mathrm{TOF} \sim 1$.

The second and third conditions define the parameters for optimal collimation. If the harmonic potential is turned on for a short duration such that the atoms hardly move during the pulse, the lens will be considered thin. The condition for a thin lens is [75]

$$\omega_k \, \tau_k \ll 1 \ . \tag{2.27}$$

Given the thin lens approximation, optimal collimation is achieved when the TOF is matched with the focal time of the lens $\omega_k^2\tau_k$, such that

$$\frac{1}{\mathrm{TOF}} = \omega_k^2\tau_k. \tag{2.28}$$

In our experiment, $\omega_k \approx 2\pi \times 1\,\mathrm{kHz}$, the DKC pulse duration is $\approx 100\,\mu\mathrm{s}$, and the TOF is $\approx 1\,\mathrm{ms}$. These parameters imply that the thin lens and long TOF approximations are not satisfied, and hence, the condition for optimal collimation given in Eq. 2.28 is not exact.

Instead of strictly following the analytical approximated model above, or using a more accurate and complex model[1], we adopted an empirical approach. We first set the TOF and the duration of the DKC pulse based on the experimental constraints and then optimized the DKC by observing the size of the cloud in the far field, 15 ms after the DKC, as a function of the DKC current. This approach proved both practical and effective, resulting in successful DKC, as demonstrated in Sec. 4.8 and Fig. 4.9.

2.4 Microwave transition in the ^{87}Rb atom

The microwave (MW) transition we use is a single photon transition between the hyperfine states $F = 2$ and $F = 1$ of the $5^2S_{1/2}$ ground state of the ^{87}Rb. The frequency of the transition $\Delta E_{\mathrm{hf}}/h = 6.834682610904290\,\mathrm{GHz}$.

Applying a magnetic field shifts the energy levels of the atomic states according to the Zeeman effect, creating five Zeeman sublevels in the $F = 2$ state and three in the $F = 1$ state. We consider here only single-photon transitions, i.e., only transitions with $\Delta m_F = 0, \pm 1$ are allowed due to the conservation of the angular momentum. These nine allowed transitions are shown in Fig. 2.2. For our new interferometer scheme, we are interested in a two-level system where one of the levels is $m_F = 0$, which is magnetically insensitive in the first-order approximation of the Zeeman effect. This leaves us with four distinct two-level systems, which

[1]Such a model for DKC in the case of an interacting BEC beyond the thin lens and long TOF approximations was developed in [76]. During the experimental work on the DKC we were not aware of this model, which seems to be a good approximation of our system and can be used to further investigate and optimize our DKC in the future.

are shown in Fig. 2.2 and in Table 2.1.

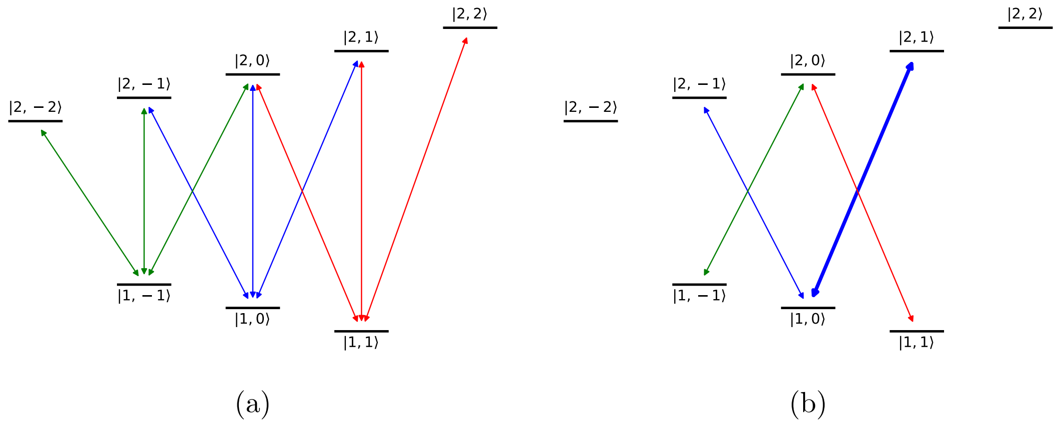

Figure 2.2: (a) The nine allowed single photon MW transitions between the hyperfine states of the $5^2S_{1/2}$ ground state of the ^{87}Rb. (b) The four possible two-level systems, in which one of the levels is in the $m_F = 0$ Zeeman sublevel. The thicker line represent the two-level system we use in our interferometer, $|2,1\rangle \leftrightarrow |1,0\rangle$. The four transitions are specified in Table 2.1.

ΔE	Two-level system
$E_{\rm hf} + \mu_B B$	$\lvert 2,1\rangle \leftrightarrow \lvert 1,0\rangle$
$E_{\rm hf} + \mu_B B$	$\lvert 2,0\rangle \leftrightarrow \lvert 1,-1\rangle$
$E_{\rm hf} - \mu_B B$	$\lvert 2,0\rangle \leftrightarrow \lvert 1,1\rangle$
$E_{\rm hf} - \mu_B B$	$\lvert 2,-1\rangle \leftrightarrow \lvert 1,0\rangle$

Table 2.1: The four possible two-level systems using the single photon MW transition, in which one of the levels is in the $m_F = 0$ Zeeman sublevel.

The transition is driven by a MW field with a Rabi frequency $\Omega_{\rm MW}$, which is proportional to the square root of the MW power. The MW field is generated by a MW source, amplified by a power amplifier, and delivered to the atoms by a MW antenna. The MW field is applied for a duration of $\tau_{\rm MW}$, which is typically on the order of a few microseconds.

Chapter 3

The Experimental Apparatus

The setup produces a Bose-Einstein condensate (BEC) of ^{87}Rb atoms, with $20-200\times 10^3$ atoms in the condensate every 26 seconds. We use a dual-chamber design, where a cold atomic beam from a 2D-MOT feeds the 3D-MOT, from which the atoms are loaded into a magnetic trap, where they are cooled by forced evaporation. While the apparatus was built during 2008–2009 and produced many impressive results with the original setup, significant upgrades and modifications were required to facilitate the new experiments described here. First, we installed a new atom chip and rebuilt the atom chip mount. Later, we upgraded the system from a single- to a dual-chamber by building our homemade 2D-MOT system. We replaced the lasers and upgraded the laser system to facilitate the required power and frequencies to operate the 3D-MOT and 2D-MOT, and replaced the imaging system. While the previous experiments used radio frequency (RF) transitions for interferometry with Zeeman sublevels within the same hyperfine level, we installed a new MW system for performing interferometry using pairs of states from different hyperfine levels of the ^{87}Rb atoms.

Another significant upgrade was achieved by loading the atoms into the atom-chip magnetic trap and reaching the phase transition in the atom-chip trap (instead of the trap created by the distant wires of the mount). This improved the stability of the final trapping position by a factor of 10 and enabled a critical enhancement in the performance of the Stern-Gerlach interferometer (SGI). The electronics and experimental control for the SGI sequence were also upgraded. All these upgrades were built on the "shoulders of giants" who built and operated the BEC2 system throughout the years, and passed the knowledge and tradition to the next generation of students, as described in the dissertations of S. Machluf [53, 77], Y. Margalit [45], and O. Amit [54].

In the following sections, we will describe the primary components of the experimental apparatus, the vacuum system, the laser system, the 2D-MOT system, the imaging system, and the atom chip.

3.1 Vacuum system

The vacuum system is a dual chamber design, with a 2D-MOT chamber and a main science chamber, connected by a differential pumping tube that allows the transfer of a cold atomic beam from the 2D-MOT chamber to the science chamber while keeping the pressure in the science chamber low. The structure of the vacuum system can be seen in Fig. 3.1. The vacuum system is made from 316LN stainless steel which, due to its low magnetic permeability, minimizes the magnetic response of the system. The main vacuum system is constantly pumped by a 300 l/s ion pump (Varian VacIon Plus 300) and a 200 l/s hybrid pump consisting of a passive Non Evaporable Getter (NEG) and an ion pump (SAES NexTorr D 200-5). At the core of the system lies the atom chip, which allows the creation of precise magnetic potentials for trapping and manipulating the atoms. The surface of the atom chip also serves as a mirror to reflect the beams of the 3D-MOT.

After installing the atom chip, we pump the system, initially with a dry scroll pump and a turbo pump, starting from atmospheric pressure and reaching high vacuum pressure (about 10^{-8} Torr). At this stage, we can turn on the ion pump. We then "bake" the system to a temperature of 115° C for a week to remove any contaminants from the chamber walls. A titanium sublimation pump is used after baking and at other times when required. The background pressure in our system, measured using a nude Bayard-Alpert type ionization gauge (Varian UHV-24p), is below 10^{-11} Torr. The 2D-MOT chamber can be separated from the main chamber using a gate valve to allow for easy maintenance of the 2D-MOT chamber. After installing the 2D-MOT, we pumped its chamber to high vacuum pressure and then baked it at 80° C for three days. The base pressure in the 2D-MOT chamber is $\approx 10^{-8}$ Torr, and the pressure during operation is $\approx 10^{-7}$ Torr. The 2D-MOT chamber is connected to a 2l/s ion pump, which we occasionally activate when we observe high pressure in the 2D-MOT chamber or a decrease in the loading rate of the 3D-MOT. While we did not measure the dependence of the loading rate on the pressure in the 2D-MOT chamber, it is well-documented that above a certain pressure, the efficiency of the 2D-MOT decreases [78, 79].

3.2 Laser system

We built a new laser system to replace the old one based on two external cavity diode lasers (ECDL), where each laser was locked to a signal from a polarization spectroscopy setup. The new laser system consists of a homemade ECDL that functions as a repumper and frequency reference and a Vescent D2-100-DBR cooler laser which is phase-locked to the repumper. The new system has a wider tuning range, is far more stable, and maintains the laser frequency lock for a full week of continuous data taking.

The cooler laser is amplified using a tapered amplifier, producing 1 W of laser power. After amplification, it is split into multiple beams; 2D-MOT cooling and push beams, 3D-MOT cooling, optical pumping, and imaging. The repumper laser is split into two beams for the 2D-MOT and 3D-MOT. The different laser frequencies are set using acousto-optic modulators (AOMs), and the power is controlled using a combination of AOMs (for real-time power modulation) and half-wave plates (for the initial distribution of power between the beams). After passing through the AOM, each beam is coupled into an optical fiber and sent to the 2D-MOT and 3D-MOT chambers. The laser system is shown in Fig. 3.2, and the beams are listed in Table 3.1.

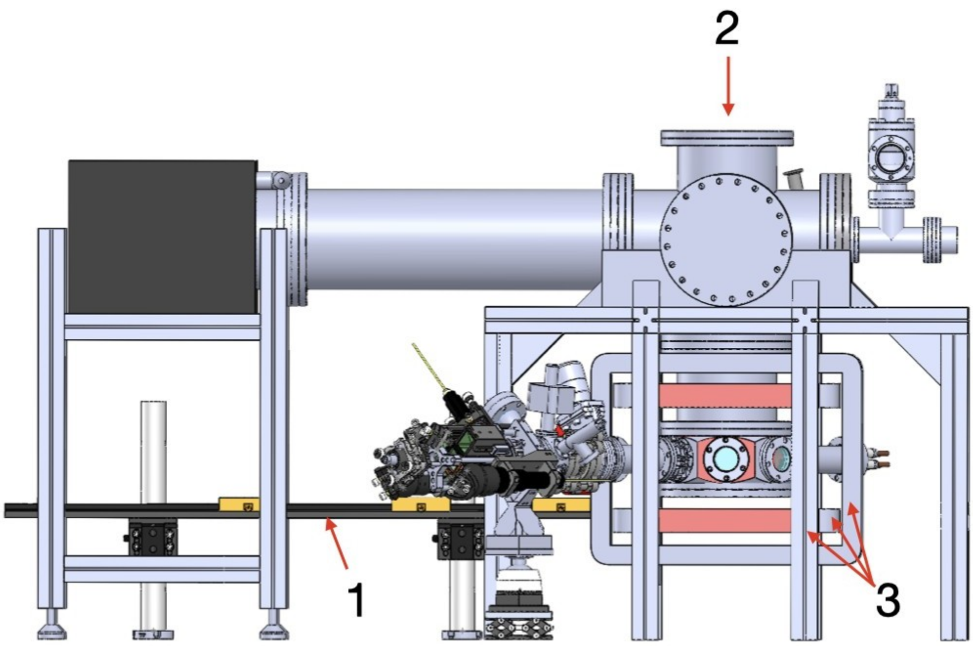

(a) Vacuum assembly side view: (1) Optical rail for the imaging system consisting of a CCD camera and two lenses. (2) The top cross that holds the atom chip mount. (3) Magnetic bias coils for x, y and z axes.

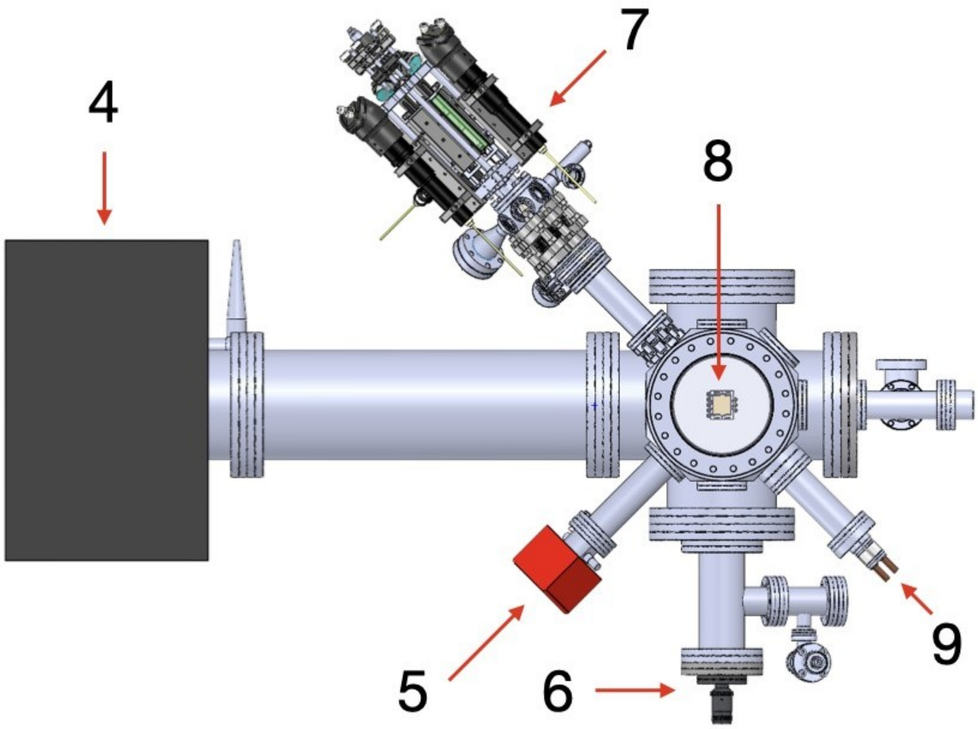

(b) Vacuum assembly bottom view: (4) 300 l/s ion pump (Varian VacIon Plus 300). (5) 200 l/s hybrid NEG and ion pump (SAES NexTorr D 200-5). (6) Titanium sublimation pump. (7) 2D-MOT. (8) Atom chip, located 7 mm above the center of the science chamber. (9) Feedthroughs for the Rb Dispensers.

Figure 3.1: Vacuum assembly from the side and bottom. Adapted from [80].

Beam	Typical Detuning [MHz]	Power [mW]	Diameter [mm]
3D MOT cooling	-15	190	30
2D-MOT cooling	-12	90	25
2D-MOT push	-12	1	3
Imaging	0	1	6
Optical Pumping	0	0.2	6
3D MOT repumper	0	2	30
2D-MOT repumper	0	2	25

Table 3.1: The laser beams used in the experiment. The frequency for each beam is shifted using acousto-optic modulators. The detuning is from the ^{87}Rb D2 line F = 2 to F′ = 3 transition, except for the optical pumping beam, which is tuned to the F = 2 to F′ = 2 transition, and the repumper laser which is tuned to F = 1 to the F′ = 2 transition. The repumper beams overlap with the cooling beams.

The stabilization of the laser frequency is achieved by locking the repumper laser to the ^{87}Rb D2 line F = 1 to F′ = 1-2 crossover transition using polarization spectroscopy. The cooler laser is then phase-locked to the repumper using the Vescent D2-135 offset phase lock servo. An external reference input frequency is set to achieve a red-detuning of 6.701376 GHz from the repumper laser. The phase-lock loop (PLL) allows tuning the cooler frequency over a wide range of several GHz without significant loss of power. The wide tuning range is an important upgrade compared to controlling the frequency by an AOM, where the tuning range is a few tenths of MHz at the maximum and also comes with a price in power reduction. The upgraded tuning range enabled us to improve the performance of the final laser cooling stage (optical molasses) and implement far-off-resonance imaging.

We measured the linewidth of the new laser setup and found it to be smaller than 1 MHz, which is within the requirements for our experiment (see Fig. 3.3). The result is comparable with measurements from [81].

3.3 Imaging system

The imaging system comprises a camera, two lenses, and the imaging laser beam. Two Achromatic Doublet lenses of focal lengths 150 mm and 300 mm and 2-inch diameter, magnify the image of the atoms by a factor of 2 (the 150 mm lens model

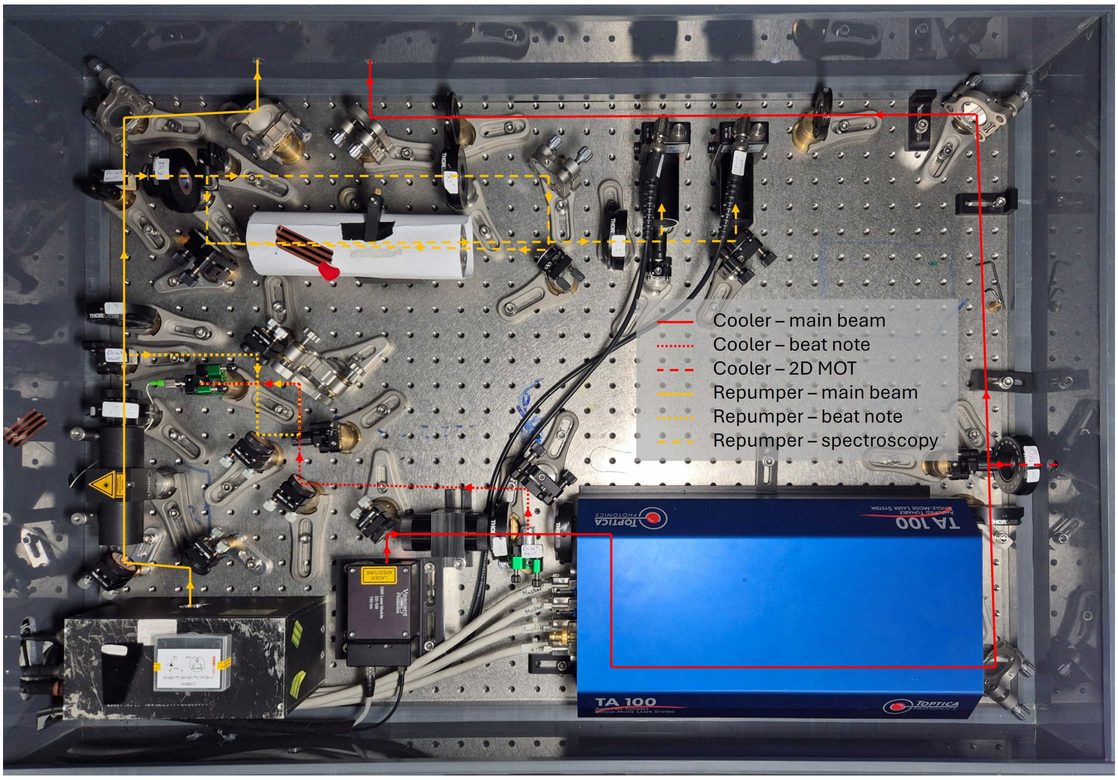

Figure 3.2: Laser system: The two lasers are kept in a closed box to reduce temperature fluctuations and light pollution. The cooler laser is a DBR laser (Vescent D2-100, 780 nm), and the repumper is a homemade ECDL. The beam paths, shown in red and yellow lines, are as follows: The cooler path starts from the laser, passes through an optical isolator, and is then split at a polarizing beam splitter (PBS), where a small fraction is directed into an optical fiber and overlapped with the repumper for beat note detection. The main beam is amplified by a tapered amplifier and then split at a PBS, where 30% of the power is sent to the 2D-MOT setup for the 2D-MOT cooler and push beams. The main beam exits the box and is directed to three AOMs (not shown) for the 3D-MOT cooler, optical pumping, and imaging beams. The repumper path starts from the laser, passes through an optical isolator, and is then split at a PBS, where a small fraction is directed into an optical fiber and overlapped with the repumper for beat note detection. The main beam is split again, and a small fraction is sent to the spectroscopy setup for locking. The main repumper beam exits the box and is sent into an AOM, after which it is split into two beams for the 2D- and 3D-MOT.

is AC508-150-B - f = 150.0 mm, Ø2” Achromatic Doublet, ARC: 650 - 1050 nm). The camera is a Lucid PHX200S, with a Sony IMX183 CMOS sensor and a pixel size of $2.4\,\mu\text{m} \times 2.4\,\mu\text{m}$, which results in a pixel size of $1.2\,\mu\text{m} \times 1.2\,\mu\text{m}$ in the object plane. The imaging resolution is diffraction-limited; the numerical aperture (NA)

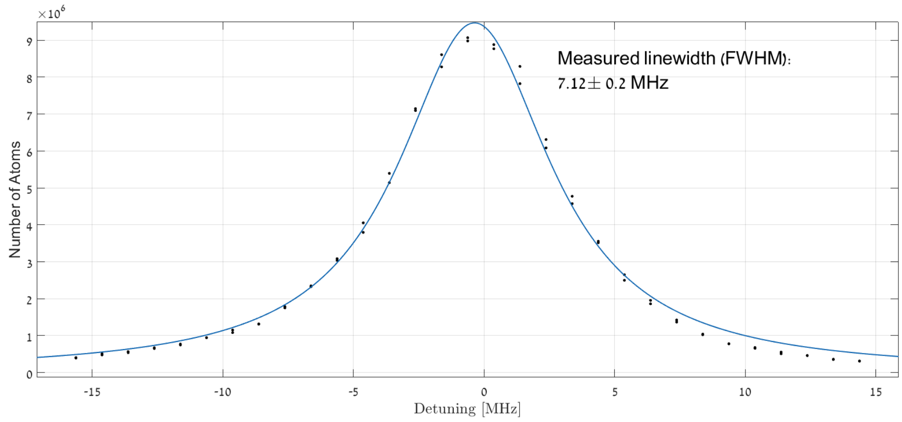

Figure 3.3: Measuring spectroscopy broadening in our experiment: We capture atoms in the MOT, release them, take an absorption image of the atoms, and measure the number of atoms in the cloud. By scanning the laser frequency, we obtain a Lorentzian due to the transition natural linewidth $\Gamma = 2\pi \times 6.0666(18)$MHz and the laser linewidth. The width of the measured Lorentzian is $\gamma = 2\pi \times (7.1 \pm 0.2)$MHz. As the convolution of two Lorentzian functions results in a Lorentzian whose width is the sum of their widths, we get an upper limit on the linewidth of the laser of ≈ 1 MHz.

of the window is 0.126, which yields a diffraction limit of $\lambda/(2\mathrm{NA}) = 3.1\,\mu$m. This resolution was confirmed experimentally.

For most of the measurements in this work, we use on-resonance absorption imaging, which we describe here in more detail. We also implemented fluorescence imaging, dark-ground imaging, reflection imaging, and off-resonant absorption imaging when required. Absorption imaging is especially useful when a well-calibrated measurement of the density of the atomic cloud and the number of atoms is required.

The imaging beam is tuned to the $F = 2 \rightarrow F' = 3$ transition. To get an absorption image, we apply two separate imaging laser pulses, with and without the atoms. In each pulse the intensity of the beam is recorded by the CCD. The atomic density can be determined using the Beer-Lambert law

$$I(x,z) = I_0(x,z) \exp\left[-\mathrm{OD}(x,z)\right], \tag{3.1}$$

where OD is the optical density and $I(x,z)$, $I_0(x,z)$ are the CCD pixel intensities in the imaging plane with and without atoms, respectively. The optical density is proportional to the column density of the atoms at a given position $\int n(x,y,z)dy$, where x and z are the object plane positions and the imaging laser is incident along the y-axis. The number of atoms $N(x_i, z_j)$ imaged by a pixel is

$$N(x_i, z_j) = \frac{A}{\sigma_o}\mathrm{OD}(x_i, z_j), \tag{3.2}$$

where A is the pixel area in the object plane, $\sigma_0 = 3\lambda^2/2\pi$ is the cross-section for resonant atom-light scattering for atoms in the $m_F = 2$ Zeeman sub-level with σ^+ polarized light, and $\lambda \approx 780.241\,\mathrm{nm}$ is the optical transition wavelength for the D_2 electronic transition, $(5^2S_{1/2} \to 5^2P_{3/2})$ of ^{87}Rb [82].

Rolling shutter

It is important to note that this camera model uses the rolling shutter method for sensor exposure, where each line of pixels in the sensor begins and ends its exposure one readout duration later than the previous line[1]. This is not optimal for our application, as only a fraction of the lines in the sensor captures the short imaging pulse of duration 20–100 μs.

We overcome this problem by using the rolling shutter with the global reset option, in which all lines begin the exposure simultaneously, allowing us to capture the imaging beam across the entire sensor at once. There is still a caveat: in this mode, the exposure of each line ends one readout duration later than the previous line, resulting in an increased exposure time as the line number increases. As long as ambient light or undesired scattered laser light is prevented from entering the camera, the increased exposure time has a negligible effect, as the signal on each pixel is determined mostly by the duration of the laser pulse and not the exposure duration. The rolling shutter with the global reset option provides good results, with the only limitation being a low frame rate of a few frames per second.

As a general rule of thumb, cameras with a global shutter are more straightforward for imaging experiments. However, a rolling shutter camera with a global reset mode can achieve good results under these three conditions: pulsed imaging laser,

[1] Rolling shutters introduce the infamous rolling shutter effect, where moving objects create interesting artifacts in the picture [83, 84]

the frame rate is not a limiting factor, and the camera is well shielded from ambient or stray light.

3.4 2D-MOT

In this section, we briefly describe the main components of our home-made 2D-MOT: the magnetic fields, laser beams, atomic source, and the differential pumping tube that connects the 2D-MOT to the 3D-MOT. We also provide a brief review of the 2D-MOT optimization process. A detailed description can be found in [80].

3.4.1 Principle of operation of the 2D-MOT

To trap and cool atoms in the transverse direction, a 2D-MOT uses a combination of magnetic fields and laser beams. In contrast to the 3D-MOT, where a magnetic field gradient is created along all three axes, the 2D-MOT creates a magnetic field gradient along two axes, resulting in a line of zero magnetic field along the third axis. Thus, the atoms can be trapped in the x-y plane (the transverse direction) but move freely along the z-axis (the longitudinal direction). Such magnetic fields can be created by two pairs of anti-Helmholtz coils. In Fig. 3.4, we present a simulation of the magnetic field produced by such a pair of coils. A set of permanent magnets is sometimes used instead of the coils. The laser system consists of two pairs of red-detuned counter-propagating laser beams, which slow down the atoms and apply the trapping force in the x and y axes. Some variations of the 2D-MOT include laser beams along the z-axis, for example, adding a "push" beam along the z-axis that pushes the atoms towards the 3D-MOT through the differential pumping tube, thereby improving the coupling to the 3D-MOT. In the 2D$^+$-MOT configuration, a "retarding" beam is applied in the opposite direction of the push beam creating optical molasses along the z-axis and cooling the atoms in the longitudinal axis. A schematic drawing of the key components of a 2D-MOT is shown in Fig. 3.5.

The atomic source can be alkali dispensers or an oven, reaching a vapor pressure of $10^{-8} - 10^{-7}$ Torr. The cold atomic beam is coupled into the 3D-MOT via a long thin tube called the differential pumping tube, which connects the 2D-MOT

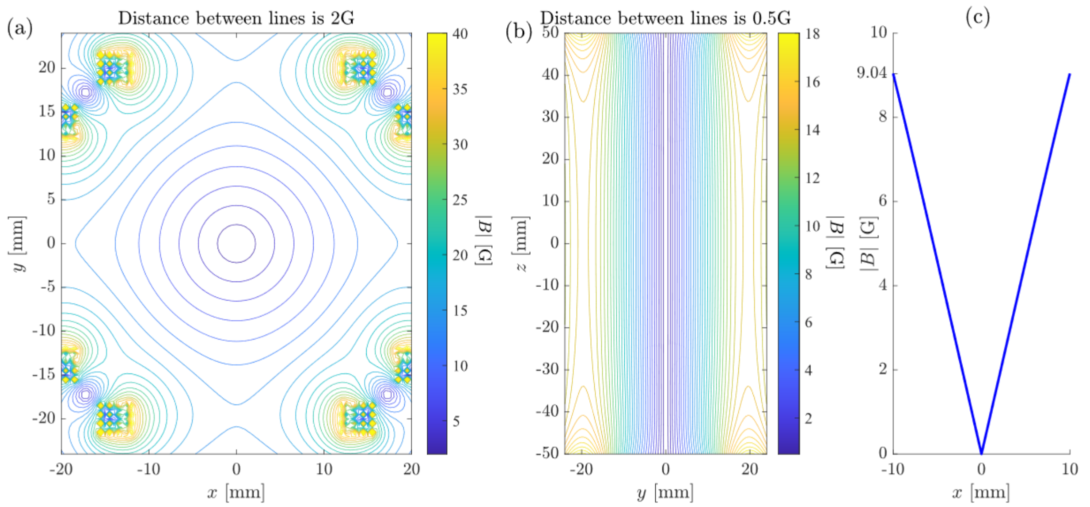

Figure 3.4: Simulation of the magnetic fields in the 2D-MOT with a current of 1 A through the coils: (a) The magnetic field in the transverse directions (x-y plane). (b) The magnetic field in both the transverse (y-axis) and longitudinal (z-axis) directions. At $y = 0$ along the longitudinal direction (z-axis), there is a zero magnetic field axis. (c) The magnetic field in the transverse direction (x-axis). From this, we obtain a gradient of 9.04 G/cm per 1 A. Taken from [80].

chamber to the main chamber. If the atomic beam is aligned correctly, centered, and parallel to the differential pumping tube, the atoms can move through the differential pumping tube from the 2D-MOT chamber into the 3D-MOT. The low conductance of the thin and long differential pumping tube results in a pressure difference of up to 5 orders of magnitude between the two chambers, which in our case allows reaching ultra-high vacuum in the main chamber in the range of $10^{-12} - 10^{-11}$ Torr.

3.4.2 Design and construction of the 2D-MOT

Our 2D-MOT apparatus can be seen in Figs. 3.6 and 3.8. The 2D-MOT is built around a rectangular anti-reflective (AR) coated glass vacuum chamber, with dimensions of 100 mm x 30 mm x 30 mm, with a CF 40 flange (Precision Glass Blowing). The glass vacuum chamber is connected to a spherical hexagon (Kimball Physics), to which the dispensers, angle valve, and a 2 l/s ion pump are connected through three CF 16 ports. The other side of the spherical hexagon is connected

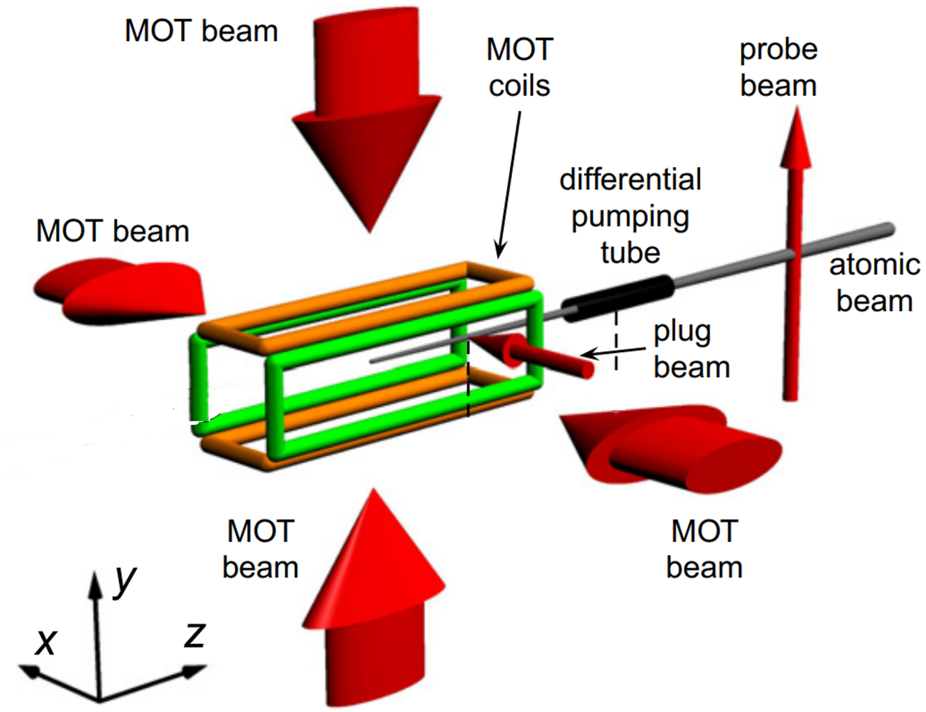

Figure 3.5: Schematics of a 2D-MOT: Two pairs of rectangular anti-Helmholtz coils produce the required magnetic field. Two pairs of red-detuned, counter-propagating laser beams apply trapping and cooling in the transverse direction. The differential pumping tube connects the 2D and 3D MOTs. Plug and probe beams can be added for controlling and probing the atomic beam. Adapted from [85].

to a flexible port aligner that allows the alignment of the whole 2D-MOT setup towards the 3D-MOT. The port aligner is connected to the gate valve, which allows the isolation of the main chamber from the 2D-MOT chamber when required. The differential pumping tube that connects the two chambers has a conical profile, with a total length of 122.5 mm, starting with a diameter of 1.5 mm and expanding up to 7 mm. Two alkali metal dispensers (model RB/NF/3.4/12 FT10+10 from SAES getters) are connected via feed-throughs.

The magnetic field is produced by two pairs of anti-Helmholtz coils. The transverse trapping beams have a total power of 90 mW, and the beams are distributed from two collimators, after which each beam passes through a $\lambda/4$ waveplate that shifts the polarization from linear to circular. Each beam is expanded by two beam splitters and a right-angle prism, and then retro-reflected by a long prism that acts both as a mirror and $\lambda/4$ waveplate. The push beam is applied using a collimator and an iris to limit the size of the beam.

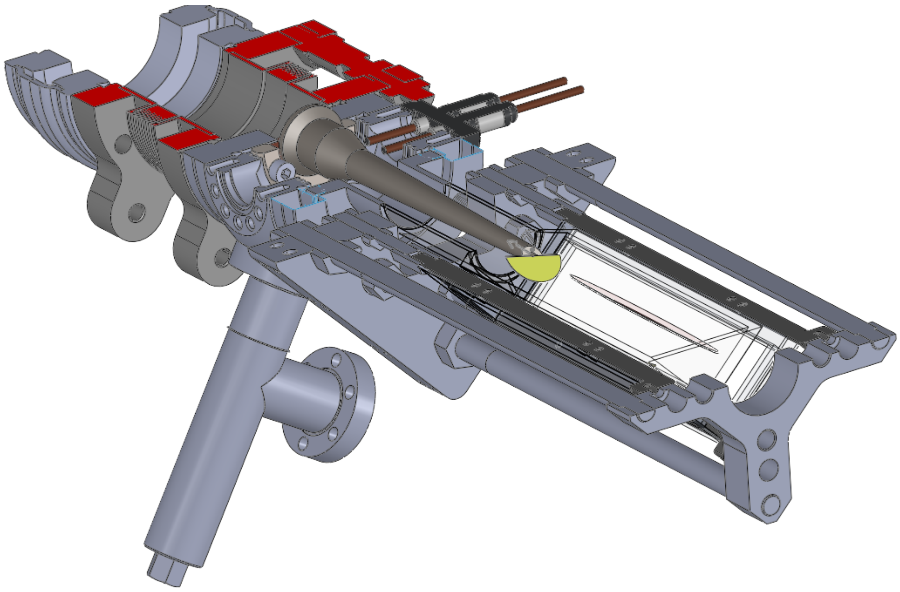

Figure 3.6: The 2D-MOT vacuum assembly: A cross-section of the 2D-MOT vacuum assembly, showing (from left to right) the gate valve, flexible port aligner, differential pumping tube, hexagon connected to feedthroughs and an angle valve, and the glass cell. In the center of the glass cell is a representation of the atomic cloud.

3.4.3 Optimization and results of the 2D-MOT

The first experimental signal from the 2D-MOT was the observation of a cloud of atoms trapped along the z-axis, which became visible when the magnetic fields and lasers were roughly aligned. The next step was to couple the atomic beam into the differential pumping tube and, from there, towards the 3D-MOT and measure the loading rate of atoms in the 3D-MOT. The initial loading rate we measured was 10^5 atoms/sec, three orders of magnitude less than our goal of 10^8 atoms/sec. While many parameters can affect the loading rate, such as the laser power and frequency, the magnitude of the magnetic gradient, and the vapor pressure, the

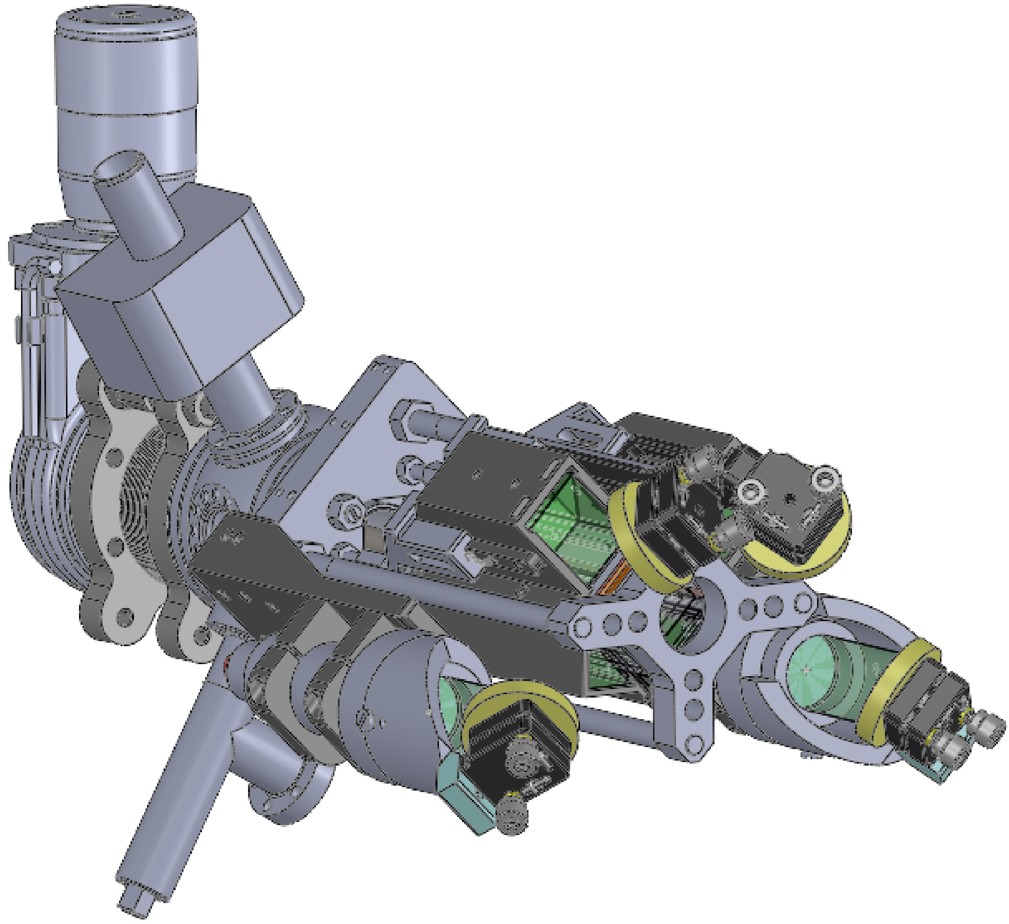

Figure 3.7: The 2D-MOT assembly from left to right: gate valve, flexible port aligner, hexagon connected to an angle valve, and the ion pump. A square aluminum bracket holds the coils and optics for distributing the cooling and the push beams.

main factor that significantly improved the loading rate by orders of magnitude was the geometrical alignment of the atomic beam, in relation to the differential pumping tube and the 3D-MOT.

The alignment between the atomic beam and the differential pumping tube is determined by the line of zero magnetic field and by the alignment of the trapping beams and push beam. We first optimized the currents in the coils so that the

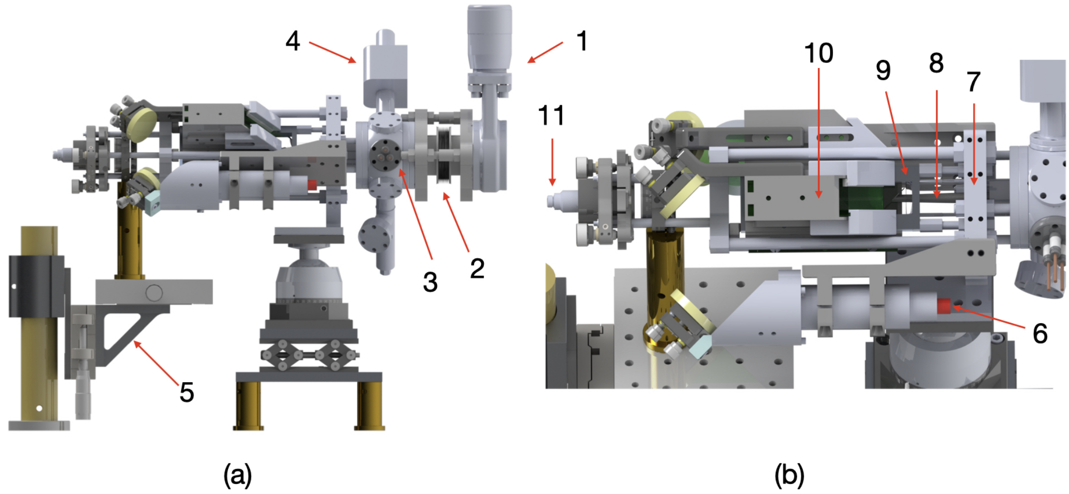

Figure 3.8: The 2D-MOT: (a) Side view of the 2D-MOT system. (b) Top side view at a 45 degree angle. Labels: (1) Gate valve, allowing isolation of the 2D-MOT from the main vacuum chamber for maintenance. (2) Port aligner, enabling angle adjustments crucial for atomic beam alignment. (3) Dispenser feedthroughs. (4) Agilent VacIon 2 L/s ion pump for pumping the 2D-MOT chamber. (5) Translation stages for holding the 2D-MOT assembly and optimizing the atomic beam angle relative to the differential pumping tube. (6) The collimator of one of the trapping beams, outputs a beam with a diameter of 25 mm. After the collimator, a $\lambda/4$ waveplate allows the beam polarization to be adjusted. (7) Base plate holding the coils assembly. (8) Differential pumping tube with a gold mirror inside the glass cell. (9) Coils assembly, containing the coils that generate the magnetic fields for 2D-MOT operation. (10) Assembly of the beam expander system, consisting of two non-polarizing beamsplitters and a prism, guiding the beam into the vacuum chamber and creating three capturing regions. (11) Collimator for the push laser fiber. Taken from [80].

atomic beam was centered with the differential pumping tube, and by slightly shifting the angle of the coils, we improved the loading rate by a factor of 10. This procedure is similar to coupling light into a fiber and is very sensitive to minor inaccuracies in the relative position and angle between the tube and the atomic beam. Next, we aligned the trapping beams' optical axis, which improved the loading rate by another factor of 5. The next step was to align the angle of the whole 2D-MOT setup using the port aligner to direct the atomic beam toward the 3D-MOT, which resulted in another factor of 5 increase in the loading rate. The final optimization was of the power of the trapping beams, current in the coils, and fine-tuning the angle and power of the push beam, which resulted in an impressive loading rate of $200 \cdot 10^6$ atoms/sec and a total number of $500 \cdot 10^6$ atoms trapped in the 3D-MOT in 3 seconds. The pressure in the 2D-MOT chamber is in the range of $10^{-8} - 10^{-7}$ Torr, and the pressure in the main 3D-MOT chamber is in the range of $10^{-11} - 10^{-12}$ Torr. Compared to our previous single chamber setup, which loaded $80 \cdot 10^6$ in 20 seconds, resulting in an average loading rate of $4 \cdot 10^6$ atoms/sec, the loading rate using the 2D-MOT is higher by a factor of 50, and the final number of atoms in the 3D-MOT was increased from $80 \cdot 10^6$ to $500 \cdot 10^6$. The dual chamber setup also has the benefit of lowering the pressure in the main chamber, extending the lifetime of the atoms in the magnetic trap from 20 to 60 seconds.

3.5 Atom chip mount

The atom chip mount holds the atom chip and copper structure required for trapping the atoms during the MOT and the magnetic trap, namely the U-wire and Z-wire (and two straight wires which are not used for the trapping, but one of them serves as an antenna for RF pulses). Due to a serious leak in the flange holding the mount, we had to rebuild the mount on a new flange and install a new atom chip. To rebuild the atom-chip mount, we produced a new MACOR piece that holds the atom chip and copper structure (see Fig. 3.9); we also produced three more atom chips. Once the mount was complete, including the MACOR piece, all the dimensions of the copper structure were measured, and the atom chip was glued to the MACOR. The next step was to bond the chip wires to the connecting pins on the MACOR. We used a bonding gold ribbon of dimensions $25 \times 250\,\mu$m, where 3-5 ribbons were bonded per pin (see Fig. 3.9). I performed the bonding on the West bond 7476E wire bonder, in which bonds are made by the wedge-wedge technique using ultrasonic energy to attach wire at room temperature. The bonding tool is manually guided by the operator using hand/eye reference to bond targets. Several test runs were made to optimize the bonding parameters, such as the bonding force, time, and power, and to ensure that the bonding would be reliable and robust.

3.5.1 Thermal management of the atom chip mount

As the mount relies on 50 cm copper rods, increasing the temperature of the mount results in an expansion of the rods, which pushes the copper structure closer to the chip and eventually breaks the chip. Thus, the heat management of the mount, though being a technical and mundane issue, becomes a crucial element in the experiment affecting its safety and the experiment cycle time. We designed a new atom chip mount to circumvent this problem by employing a design that allows for the expansion of the copper rods without pushing the copper structure toward the chip, but the production of such a mount was found to be too time and resource-consuming. We therfore decided to use the existing mount and improve the heat management instead of producing a new mount. With this approach, plus the faster MOT loading, we were able to reduce the experiment cycle time from 60 to 26 seconds.

It should be noted that after introducing the 2D-MOT and improving the heat management, another factor two reduction in the cycle time was possible with further optimization of the evaporative cooling (for example, performing the evaporative cooling fully in the atom chip trap). However, as the 26-second cycle time was sufficient for the goals of this work, we decided not to invest more time in this matter. For experiments that require a high repetition time of 1Hz, the technology for rapid BEC production is available [86, 87] and can be implemented for Stern-Gerlach interferometry.

The concept is simple: reduce the temperature of the feedthrough, which will allow for better heat transfer from the mount to the environment; this is achieved using a heat sink connected to the feedthrough. As heat is produced not only in the mount (vacuum side of the feedthrough) but also in the wires leading from the power supply to the mount (air side of the feedthrough), we also improved the heat management in this area. We increased the diameter of the wires from 5 mm to 8 mm, increasing the cross section by a factor of 2.56. As even these wires heat up during the cycle, we built a homemade custom "super-wire" for the last section of the wire, made from seven Kapton-insulated copper wires, each with a diameter of 3 mm. These are connected at each end but well separated along the length of the wire to allow for good airflow (see Fig. A.2). The super-wire has a cross-section similar to the 8 mm diameter wire, producing the same amount of heat per unit length. However, it has a 2.6 larger surface area and only a thin layer of insulation, which allows for much better heat transfer to air. The super-wire can carry a DC current of 90 Ampere without significantly heating due to its large surface area (we measured an increase of 1° C above the ambient temperature at this current). To expedite the evacuation of heat from the vacuum side, we installed heat sinks on the air side of the feed troughs and mounted three fans to blow air onto the heat sinks. This solution proved to be very effective in terms of both time and resources, as well as in the improved safety and cycle time of the experiment. Using these straightforward upgrades, we could run the system at a higher duty cycle (the Z-wire is on for 12 seconds out of 26, compared to the previous 12 out of 60). We also use an active protection system in which the temperature of the feedthrough is monitored, and if it passes a defined threshold, a TTL signal turns off the relevant power supply. More details may be found in the appendix A.

3.6 Atom chip

The atom chip is the core of the experiment as it provides the magnetic potentials not only for applying the SG forces during the interferometer but also for the DKC and the final magnetic trap. All three applications require accurate time-dependent potentials, for which the atom chip is an optimal tool. The nano-fabricated wires on the atom chip allow for accurate spatial control of the magnetic field, and the low inductance of the wires, together with custom-made electronics, enables fast, accurate modulation of currents in the temporal domain.

The atom chip is nano-fabricated from a single piece of silicon (30 mm $\times$ 25 mm) with a thickness of 500 μm, on which a thin gold layer of 2 μm is deposited. The 2D array of wires is etched onto the gold surface. Our design of the chip wires consists of three sets of wires, totaling nine. Three parallel wires at the chip's center provide the gradients for applying the SG forces during the SGI. The magnetic trap consists of two straight wires for confinement along the y-axis and four U-wires for confinement along the x-axis. The chip is shown in Fig. 3.10, and the wire scheme is shown in Fig. 3.11.

To test the current carrying capacity of our chip, we measured the increase in resistance of the wires while running a DC current. The two straight wires showed an increase of 20% at a current of 730 mA, corresponding to a temperature increase of 60° C. The U-wires showed an increase of 20% at a current of 800 mA. These limits allow us to safely run the experimental scheme, which requires a current of 700 mA in the U-wires and 500 mA in the straight wires.

Figure 3.9: The atom chip on its mount: The chip is glued to the MACOR block that also holds the copper structure. The ribbon bonding between the chip and pins is visible at both edges of the chip, and the connection of the copper structure to the leads is visible at the top and bottom.

3.6.1 Protection of the atom chip

The thin wires of the atom chip can quickly heat up and burn if a DC current of approximately 1 A passes through them. To prevent this, we use a simple homemade protection system with two fast-blowing fuses (5×20 mm fast-acting glass body cartridge fuse 0.4A rating, model, Littelfuse 0217.400MXP). One fuse

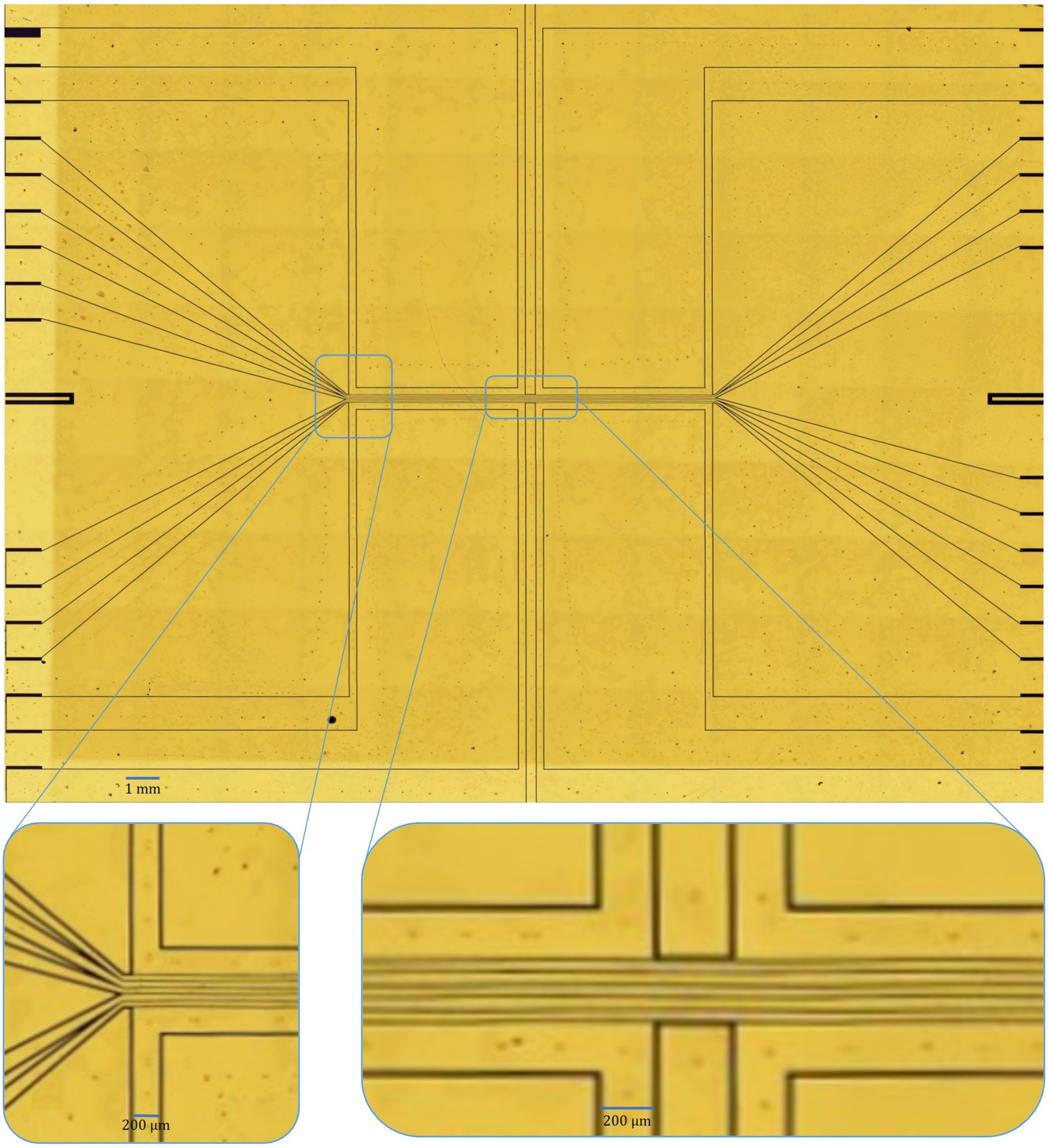

Figure 3.10: Optical picture of the atom chip: The zoom-in shows the center of the chip, where all nine wires lie. The scheme of the wires and their dimensions is given in Fig. 3.11.

is embedded in the power supply output, and another is installed just before the feedthrough leading to the atom chip. The fuses were carefully chosen and tested so that they burn before any risk of damaging the chip rises.

Initially, we designed and built an active protection system in which the resistance of the chip is monitored, and if it exceeds a defined threshold, a TTL signal turns off the relevant power supply. However, we found that such a system was too complicated and could introduce noise in the atom chip wires. Therefore, we decided to use a simple fuse-based passive protection system, which proved to be very effective.

As in the case of thermal management of the atom chip mount, this appears to be a mundane, technical issue. However, it is crucial for the safety of the experiment and the longevity of the atom chip. A burnt chip completely stops the experiment and necessitates opening the vacuum, followed by a time and resource-consuming process of installing a new chip, reaching ultra-High Vacuum (UHV), realigning some of the optics, and more. Thus, investing time and effort into an appropriate protection system is a simple and cost-effective measure that significantly boosts the productivity of experimental systems. This indeed saved our atom chip several times from human and machine errors.

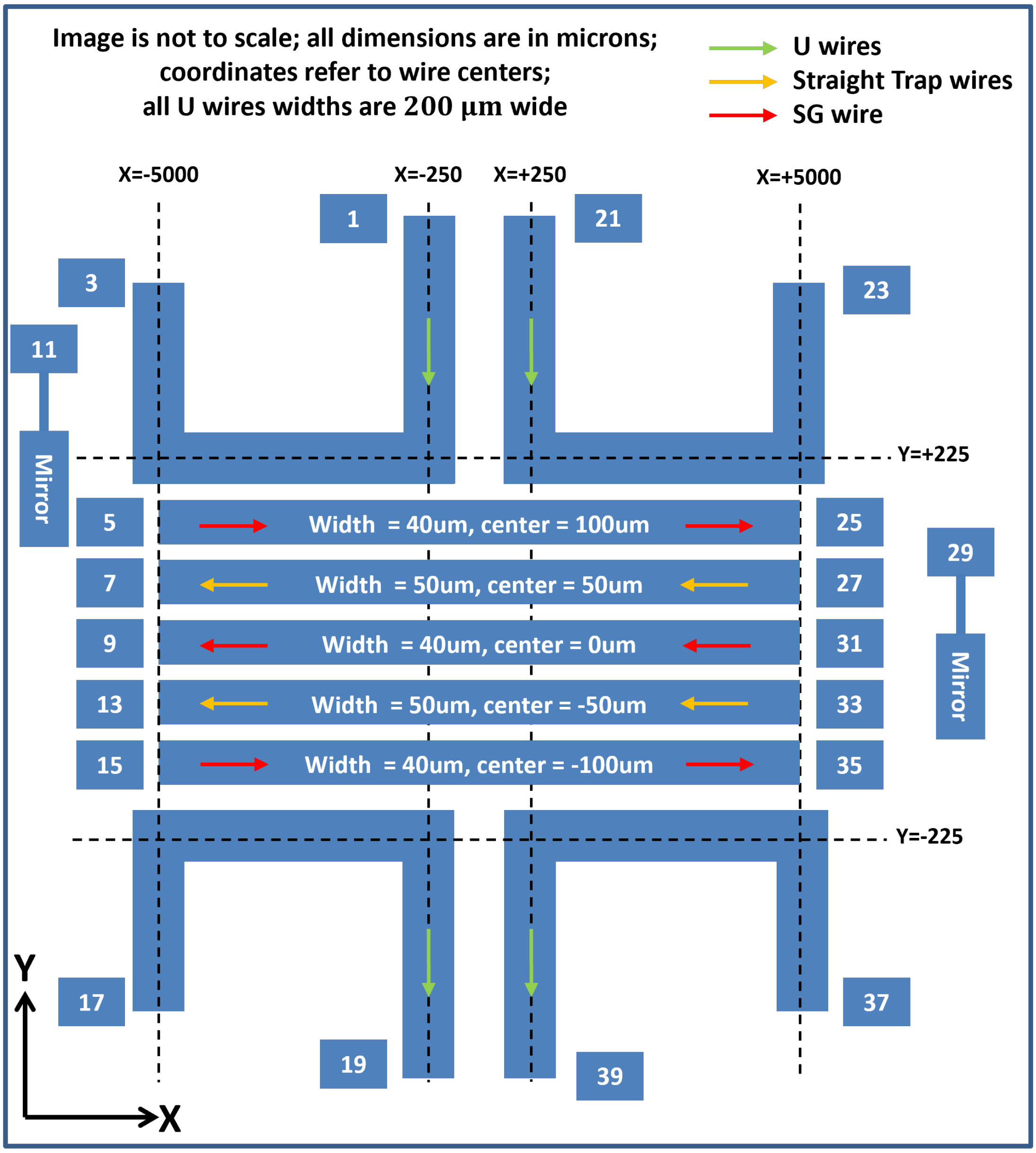

Figure 3.11: The atom chip wires scheme: The numbers indicate the wire pads. The arrows indicate the direction of the current. The magnetic trap is formed by 4 U-wires connected in series, and two straight wires connected in series as well. The gradients for the SGI are produced by three straight wires, where the current in the two outer wires has an opposite polarity relative to the middle one, creating a magnetic quadruple. The current flow for the U-wires is $(1 \to 3) \to (17, 19) \to (21 \to 23) \to (37 \to 39)$, for the two straight wires $(7 \to 27) \to (13 \to 33)$, and for the SG wires $(5 \to 25) \to (31 \to 9) \to (15 \to 35)$.

Chapter 4

BEC Production

In this chapter, we detail our experimental sequence for producing the BEC, including the MOT loading, magnetic trap, evaporative cooling, and the phase transition to BEC. In the final section, we describe the delta-kick cooling (DKC) process that allows us to collimate the expansion of the BEC and to reach an effective temperature of 3.3 nK.

4.1 MOT loading

As described in Sec. 3.4, we load the atoms to the 3D-MOT from the cold atomic beam produced by the 2D-MOT. The loading rate is 200M atoms per second, and we load up to 500-600M atoms. The number of atoms in the 3D-MOT vs time is shown in Fig. 4.1. While the number of atoms starts to saturate after three seconds of loading, we set the loading duration to five seconds to render the scheme less sensitive to drifts or fluctuations in the loading rate. Such drifts may occur due to changes in the parameters, such as the vapor pressure of the 2D-MOT and the alignment or power of the beams.

During the loading stage, the 3D-MOT cooling beams are red-detuned by 3Γ, and the 2D-MOT cooling beams by 2Γ. The current in the U-wire is 35 A, and the current in the y and z bias coils is 10 A and 3.7 A, resulting in a magnetic field of roughly 8 G and 3 G respectively. At the end of the MOT loading, we apply a short duration (20 ms) of gray MOT, by increasing the detuning to 5Γ in a 10 ms ramp, which results in a temperature of $\sim 150\,\mu$K.

To improve transfer into the magnetic trap, we compress the MOT and cool the atoms by applying gray MOT and optical molasses. To achieve compression, the current in the U-wire is reduced from 35 A to 32 A, while the y-bias field is increased from 10 G to 14 G. This occurs in a ramp with a duration of 90 ms to ensure that the transfer is adiabatic, which helps reduce oscillations and heating of the cloud. Fig. 4.2, displays real-color images of the atoms in the MOT during the loading and compressed MOT stage.

At the end of the compression, the MOT is $\sim$ 2 mm below the chip, while the initial position of the MOT is $\sim$ 7 mm below the chip.

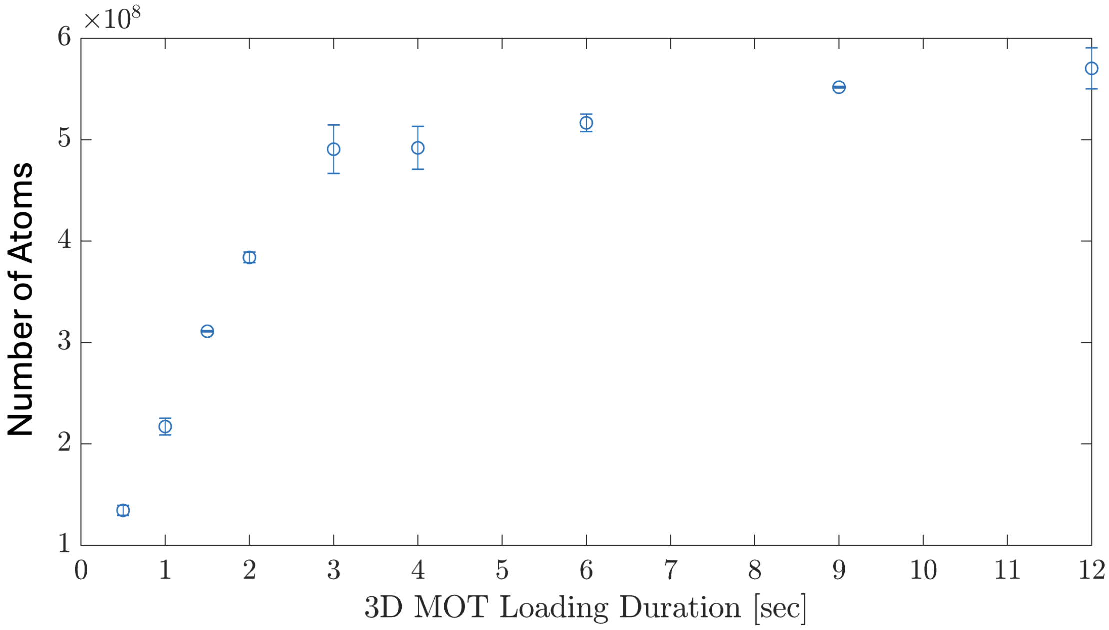

Figure 4.1: 3D-MOT loading: The number of atoms trapped in the 3D-MOT as a function of time. After one second, more than $200 \cdot 10^6$ atoms are trapped; after 3 seconds, $500 \cdot 10^6$ atoms.

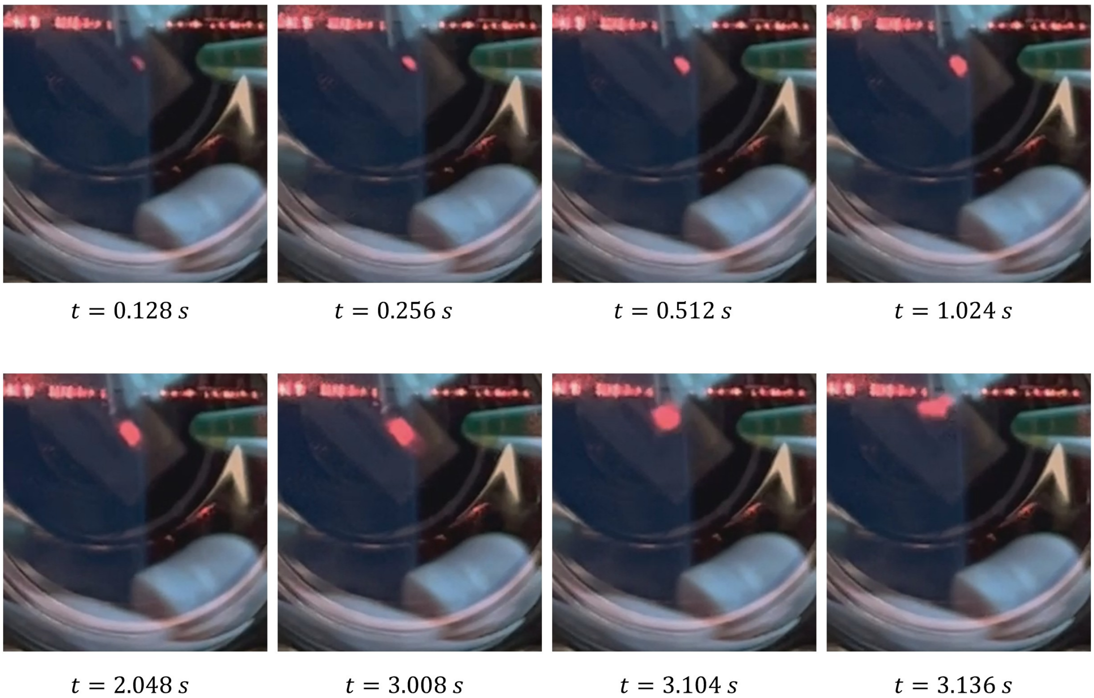

Figure 4.2: MOT loading time lapse: Real-color images taken with a standard smartphone camera. The time shown below each picture indicates the duration from the start of loading. The MOT is located a few mm below the chip and increases in size from image to image. The shiny red spots and columns at the top are the pins on the atom chip mount. The last two pictures display the compression of the MOT.

4.2 Gray MOT and optical molasses

We apply gray MOT and optical molasses to cool the cloud further and enhance the initial phase space density of the atoms in the magnetic trap. The gray MOT is applied during the last 10 ms of the compression and starts by increasing the detuning of the cooling light to 12Γ in a ramp of 3 ms. For the optical molasses, we first turn off the laser beams and the magnetic fields. After 1.5 ms, we turn on the laser beams for a short 1.5 ms pulse. We detune the cooling beams in a ramp with a duration of 1.5 ms from 5Γ to 27Γ. At the end of the optical molasses, the temperature of the atoms reaches $50\,\mu$K in the x-axis and $16\,\mu$K in the y-axis. We determine the temperature by measuring the size of the cloud vs the time of flight of the atoms after the molasses stage, as shown in Fig. 4.3. The enhancement of

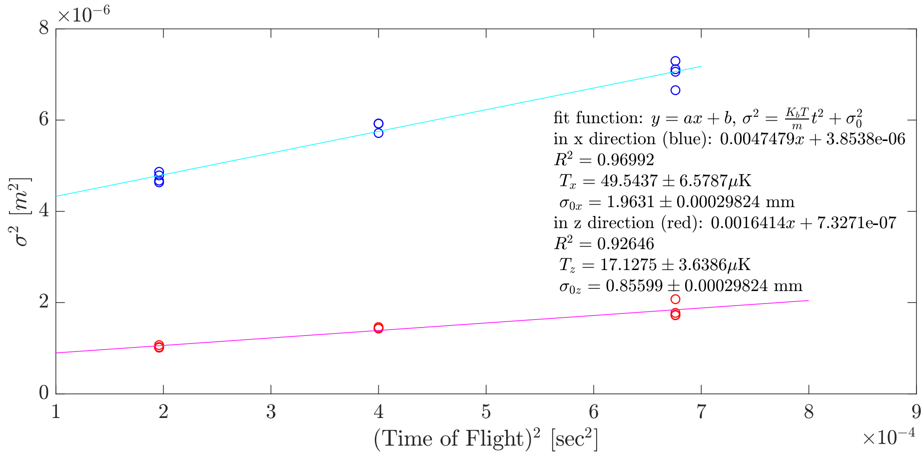

Figure 4.3: Temperature after the optical molasses via time-of-flight: The atomic cloud freely expands while falling under the influence of gravity. The cloud expands due to the kinetic energy of the atoms, which depends on their temperature. We image the cloud at different time-of-flight values and fit each image of the cloud with a 2D-Gaussian to get the Gaussian width as a function of time. By fitting $\sigma^2 = \frac{K_b T}{m} t^2 + \sigma_0^2$ [53] on the data, we obtain $T_x \approx 50\mu$K and $T_z \approx 17\mu$K. The vertical difference between the two axes reflects the initial size difference of the cloud in the radial and longitudinal directions caused by the asymmetry of the compressed MOT. The difference in temperatures indicates that the cloud is not in thermal equilibrium.

the optical molasses, i.e., shortening it and reaching lower temperatures compared to the previous setup [45]), is possible due to the wide tuning range of the cooler laser. However, the efficiency of the optical molasses is still limited, mainly due to residual magnetic fields and the imbalance of the laser intensity in the reflection MOT setup.

4.3 Optical pumping

In the MOT and optical molasses, the atoms are distributed evenly over the 5 Zeeman sublevels of the $F = 2$ ground state. As only the $m_F = 1$ and $m_F = 2$ are trappable in the magnetic trap, we apply a stage of optical pumping 300 μs after the molasses stage by applying a short 700 μs pulse of σ^+ polarized laser light along the y-axis. The magnetic bias field in the y-axis defines the quantization axis of the Zeeman sub-levels and is produced by the y-bias coils in a ramped manner as part of the magnetic trap loading. The optical pumping beam has a power of

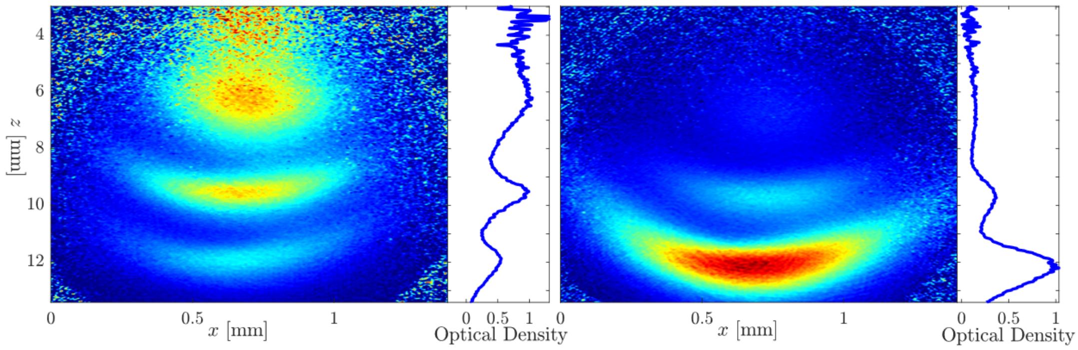

Figure 4.4: Demonstration of optical pumping: To estimate the population in the different Zeeman sub-levels, we apply a strong magnetic gradient using the z-wire, which separates them. The $m_F = 0$ state falls under gravity, while $m_F = 1$ and $m_F = 2$ are pushed downward with different accelerations ($m_F = 2$ experiences a force twice as strong). The $m_F = -1$ and $m_F = -2$ states are pushed upward toward the atom chip and are not visible in the image. The left image shows the distribution between the Zeeman sub-levels without optical pumping. The optical pumping is activated in the image on the right, efficiently transferring most of the atoms to the $m_F = 2$ state. We optimize the optical pumping parameters by minimizing the number of atoms in the $m_F = 1$ state. Taken from [80].

≈ 200 μW and a diameter of 6 mm and is tuned to be on-resonance with the $F = 2$ to $F' = 2$ transition. During the optical pumping pulse, the detuning is varied linearly from approximately $-\Gamma$ to Γ to ensure coverage of the resonance frequency of the transition during the ramping of the y-bias field. Due to the closed-cycle optical transition, repeated excitation-emission cycles polarize the atoms in the $|2, 2\rangle$ state, which is a dark state, thus limiting the interaction of the atoms with the laser. As some atoms decay to the $F = 1$ state, the repumper is also active during the optical pumping stage and is shut off 500 microseconds after the brief optical pumping pulse. Fig. 4.4 demonstrates the efficient transfer of the atoms to the $m_F = 2$ state of the optical pumping pulse. After the optical pumping pulse, the temperature is 90 μK in the x-axis and 75 μK in the z-axis.

4.4 Magnetic trap

We create an Ioffe-Pritchard trap using a Z-shaped wire and a homogeneous bias field in the y direction, along with an additional homogeneous bias field in the x

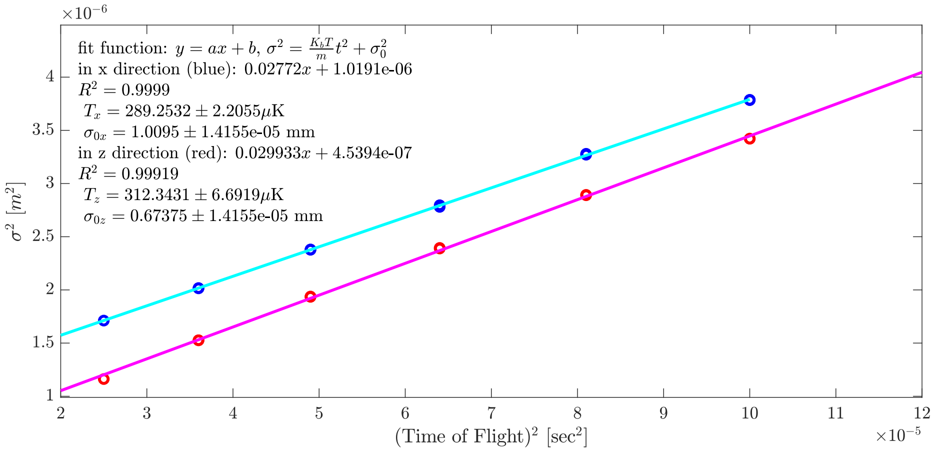

Figure 4.5: Measurement of the temperature after loading into the magnetic trap: The atoms are released from the trap and freely expand. The measurement, fitting, and analysis are the same as in Fig. 4.3 and yield $T_x \approx 290\mu$K and $T_z \approx 312\mu$K.

direction to control the minimum value of the magnetic field. We "mode match" the trap with the compressed MOT, i.e., match their position and frequency. We first optimize the field to maximize the number of atoms loaded into the magnetic trap and then fine-tune them to minimize the temperature of the cloud after loading, thus maximizing the initial phase space density. For the mode matching stage, the current in the Z-shaped wire is 90 A, and the bias fields along the y-axis and x-axis are set to about 55 G and 25 G, respectively. We load about $100 \cdot 10^6$ atoms into the magnetic trap with a temperature of approximately 300 μK (see Fig. 4.5) and a lifetime of about 60 seconds. After loading the atoms into the trap, we begin the evaporative cooling and gradually change the fields for three seconds to get the trap into its final position and frequency for the evaporative cooling stage, with 62 A in the Z-shaped wire, and 45 G and 35 G along the y-axis and x-axis respectively.

4.5 Evaporative cooling

After loading the atoms into the magnetic trap, we start the evaporative cooling stage. The RF frequency starts at 50 MHz and is exponentially lowered within 12 s in a series of steps to a final value of ~ 0.415 MHz where the phase transition to a BEC is reached. Alternatively, to prepare the atoms for transfer to the atom

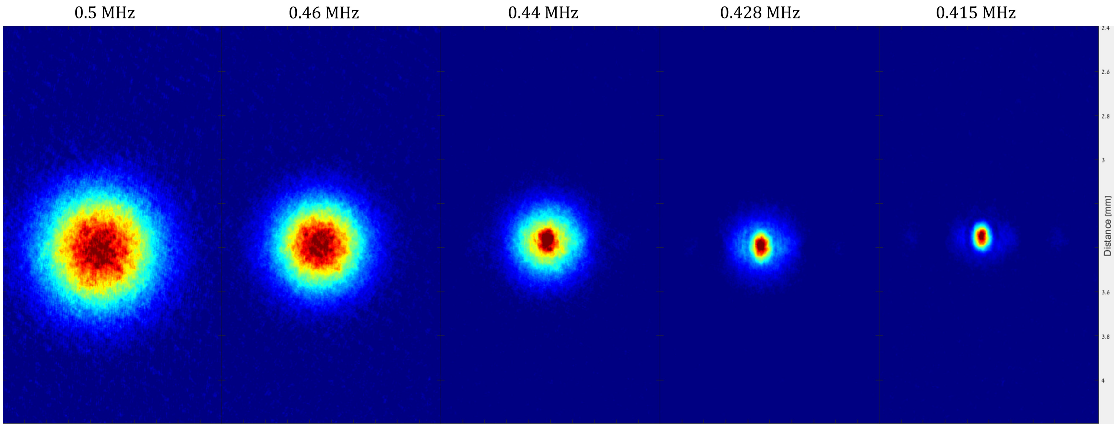

Figure 4.6: The phase transition to BEC: CCD images of the atoms 26 ms after release from the z-wire trap, showing the phase transition to BEC. The frequencies above each image indicate the frequency of the last RF ramp. We observe the phase transition from a thermal cloud at 0.5 MHz to a BEC with high purity at 0.415 MHz. The thermal cloud exhibits isotropic expansion, while the BEC exhibits anisotropic expansion. The thermal distribution of the kinetic energy determines the expansion rate of the thermal cloud. In contrast, the expansion rate for the BEC is determined by the trap frequency and the repulsive atom-atom interactions.

chip trap, we set the final value of the RF to 0.5 MHz, and load the atoms to the atom chip trap where the final evaporation stage is applied. The lowest RF frequency, which controls the final cloud temperature and BEC purity, is occasionally optimized to compensate for small variations in the magnetic fields.

4.6 Phase transition to BEC

As the temperature of the cloud is reduced below the critical temperature ($\sim$ 200 nK), we observe the phase transition from a thermal distribution to BEC, as seen in Fig. 4.6. The thermal cloud exhibits isotropic expansion, while the BEC exhibits anisotropic expansion. The thermal distribution of the kinetic energy determines the thermal cloud expansion rate. In contrast, the expansion rate for the BEC is determined by the trap frequency and the repulsive atom-atom interactions. The anisotropic expansion is demonstrated in Fig. 4.7, where we image the BEC in free fall.

We measure 200×10^3 atoms in the condensate, which is a 20-fold increase in the number of atoms in the BEC compared to the previous setup [45]. This enhancement was made possible due to the upgrades mentioned in this chapter and Ch. 3. The dual chamber design increases the number of atoms in the MOT and the lifetime of the atoms in the magnetic trap. The improved optical molasses and optimized trap loading further increase the initial phase space density of the atoms in the magnetic trap, resulting in a higher number of atoms in the BEC.

4.7 Phase transition to BEC on the atom chip

To transfer the atoms from the z-wire trap to the chip trap, we set the last ramp of the evaporation stage in the z-wire trap $\sim 0.1\,\mathrm{MHz}$ above the phase transition, and transport the z-wire trap closer to the chip in an adiabatic manner, with a ramp duration of 250 ms. We then gradually reduce the current in the z-wire and y-bias while ramping up the currents in the chip trap during 500 ms; at this point, the z-wire is at zero current, and the atoms are trapped in the atom chip trap. Following this, we increase the current in the chip wires and y-bias during 400 ms to reach the final chip trap configuration.

At this stage, we apply one second of RF evaporation, leading to the phase transition to a BEC (see Fig. 4.8), with $15 - 30 \times 10^3$ atoms in the condensate.

To quantify the stability of the chip trap, we measured the shot-to-shot fluctuations in the trap position 2 ms before release. We found the standard deviation to be $0.1\,\mu\mathrm{m}$ (see Fig. 6.12). The high stability of the chip trap improves the visibility and phase stability of the SGI.

4.8 Delta-kick cooling

Once we release the BEC from the trap, it expands rapidly along the z-axis due to the high trapping frequency along the transverse axes, and the high atomic density in the trap. This rapid expansion presents both a challenge and an opportunity. The faster expansion rate results in a smaller coherence length of the BEC, as the coherence length is inversely proportional to the momentum spread of the wave packet (as explained in Sec. 2.1.3). However, this rapid expansion enables the ap-

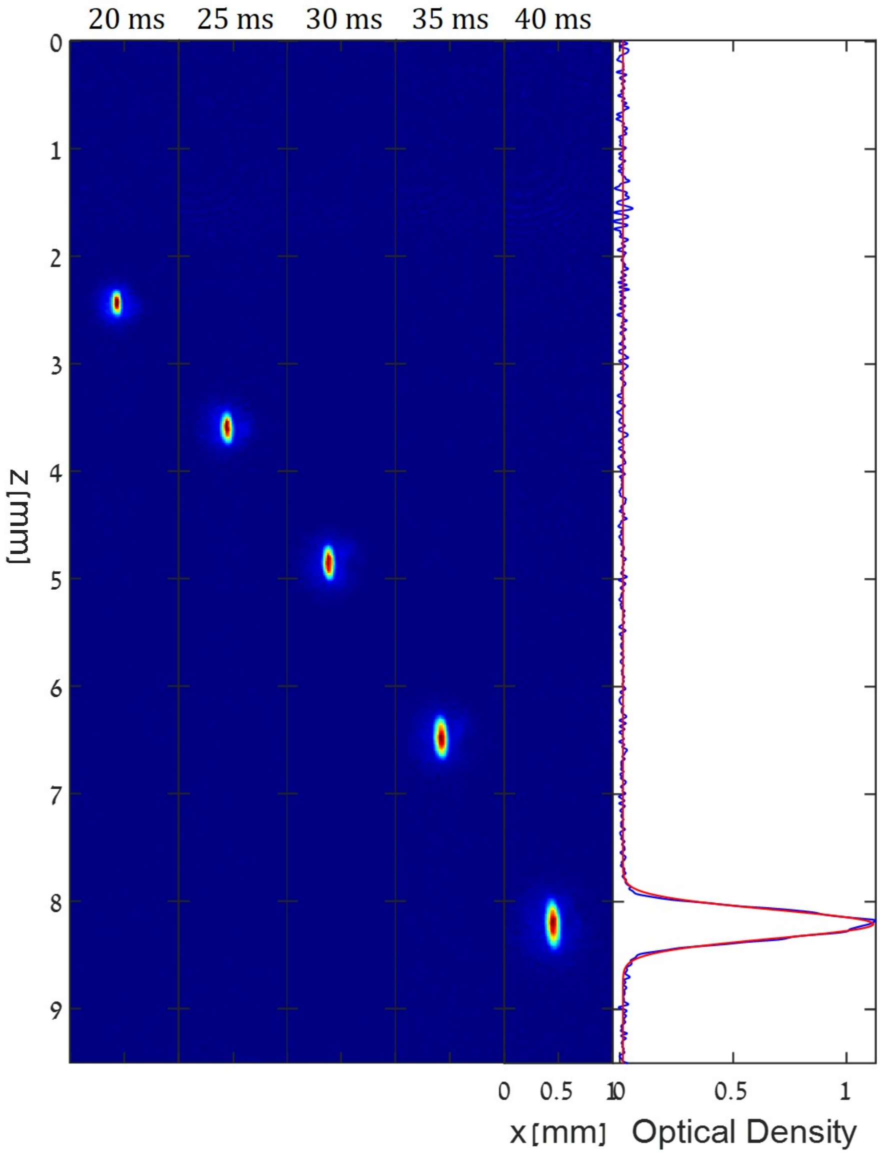

Figure 4.7: BEC in free fall: The images show the atoms free-falling due to gravity; the time above each image indicates the duration of the free fall after release from the magnetic trap. The BEC exhibits an anisotropic expansion, as opposed to the isotropic expansion of a thermal cloud.

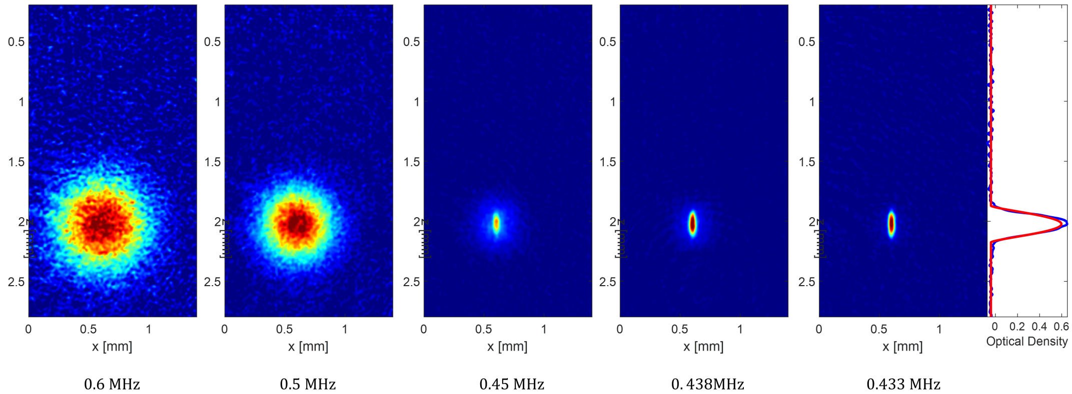

Figure 4.8: Phase transition to BEC on the atom chip trap: CCD images of the atoms 20 ms after release from the atom chip trap, showing the phase transition to BEC. The frequencies below each image indicate the frequency of the last RF ramp. We observe the phase transition from a thermal cloud at 0.6 MHz to a BEC with high purity at 0.433 MHz.

plication of DKC, which exploits the correlation between position and momentum that develops during the wave packet's expansion (see Sec. 2.3).

We leverage the rapid expansion rate and apply DKC to the BEC, reducing its expansion rate. We first allow the BEC to expand freely for 1 ms, then turn on the trapping potential for $\sim 100\,\mu$s. Such short delta-kick operation of the trap is possible thanks to the low inductance of the chip wires.

The exact values are the following: We release the atoms from the trap by shutting off the current in the chip trap with a linear ramp of 30 μs. The finite duration of the ramp gives the BEC some upward momentum. After a time of flight of 1030 μs, we apply DKC by running a pulse of current through the straight trap wires for 110 μs with a current of 470 mA. The shape of the pulse is a trapezoid with a linear rise of 9 μs and a linear fall of 22 μs.

The DKC collimates the BEC along the z and y axes and reduces its expansion rate to an effective temperature of 3.3 nK along the z-axis. Fig. 4.9 shows the temperature with and without DKC, and Fig. 4.10 shows the raw images from the CCD for a visual representation of the collimation effect of the DKC. A desired side effect of the DKC is a momentum kick to the BEC that launches it upward toward the chip.

We optimized the DKC current by observing the BEC in the far field (15 ms after the trap release). We measured the size of the BEC along the z-axis vs. the DKC current (Fig. 4.11) and found values that give minimal wave packet width at 470 mA, and 550 mA. For our experiments, it is favorable for the atoms to begin with a velocity upward against gravity, so we chose the lower value of 470 mA for the DKC current, as a lower current results in a push upward.

The DKC reduces the expansion rate of the BEC along the z-axis to 0.4 μm/ms, which corresponds to an effective temperature of 3.3 nK (Fig. 4.9). The upward momentum propels the atoms into a ballistic trajectory, reaching a maximum height $2930 \pm 100\,\mu$s after the trap release.

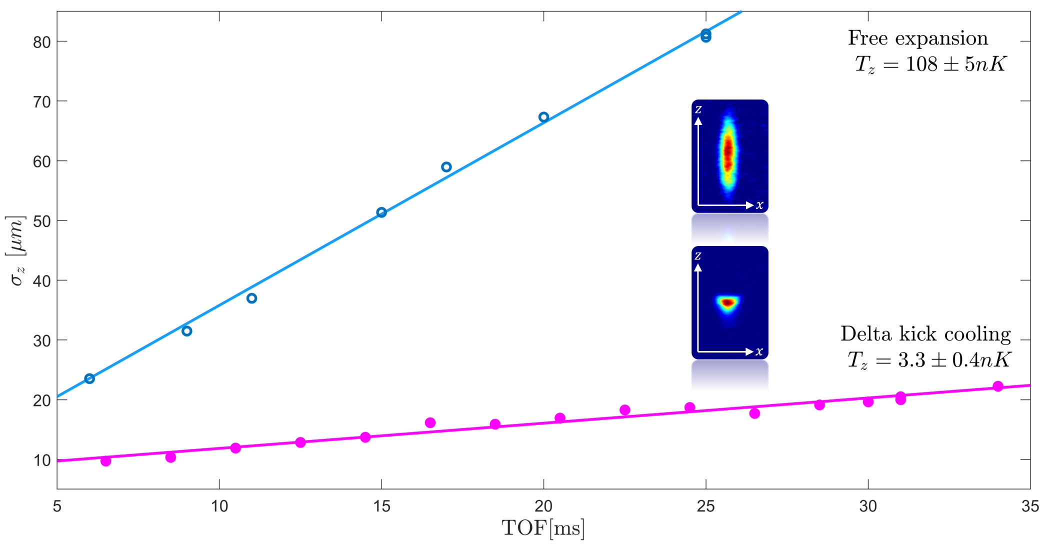

Figure 4.9: Temperature measurement with and without DKC: The expansion rate with DKC is 0.4 μm/ms, corresponding to an effective temperature of 3.3 nK. For free expansion without DKC, the expansion rate is 3.1 μm/ms corresponding to an effective 108 nK. The inset shows the CCD image of the atoms with and without DKC after time of flight of 26.5 ms and 25 ms, respectively. Taken from [13].

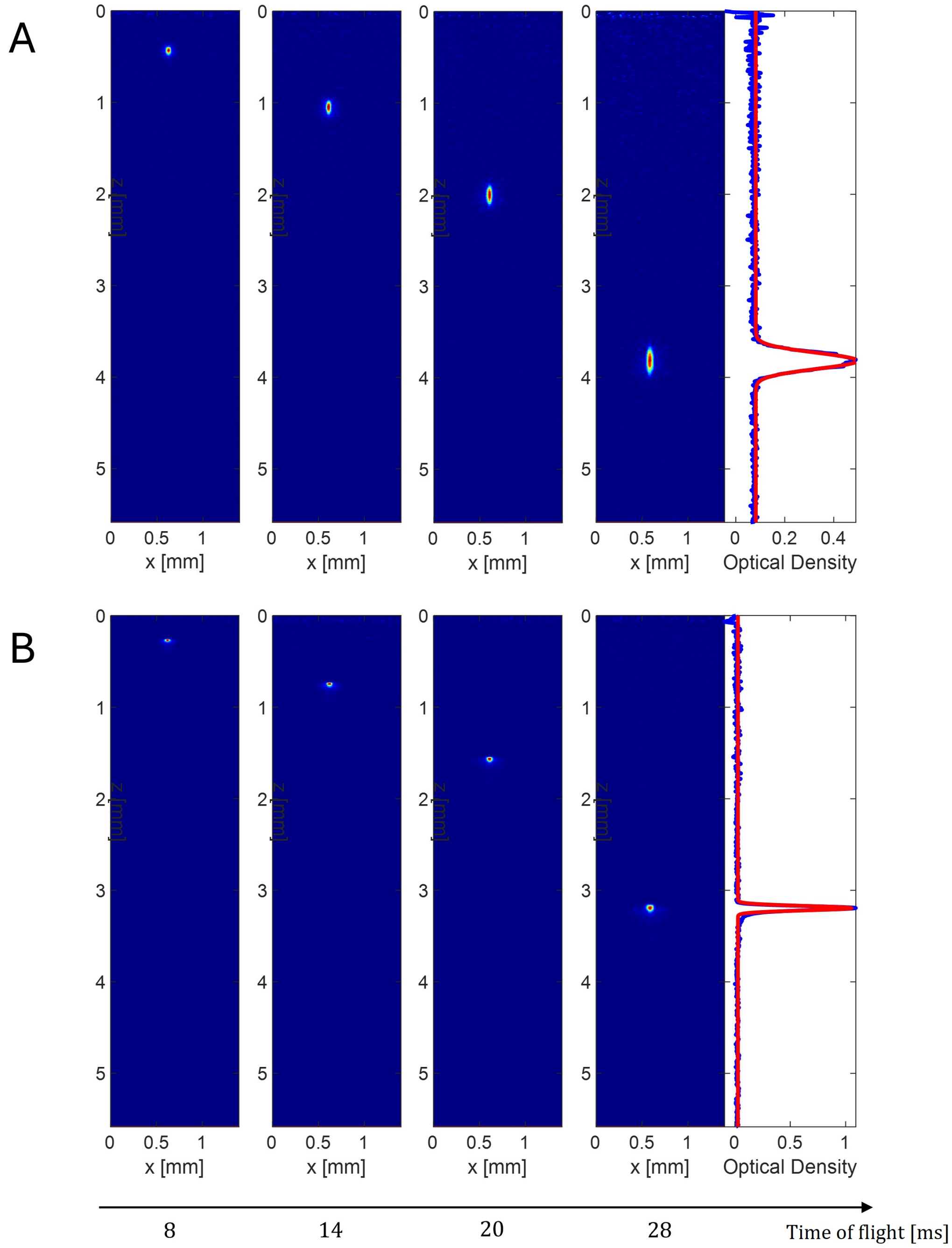

Figure 4.10: DKC vs free expansion: CCD images of the atoms during the time of flight after trap release for $t = 8, 14, 20, 28\,\mathrm{ms}$. (a) Free expansion without DKC. The BEC rapidly expands along the z-axis. (b) Expansion with DKC. The BEC is collimated along the z-axis, as well as pushed upward.

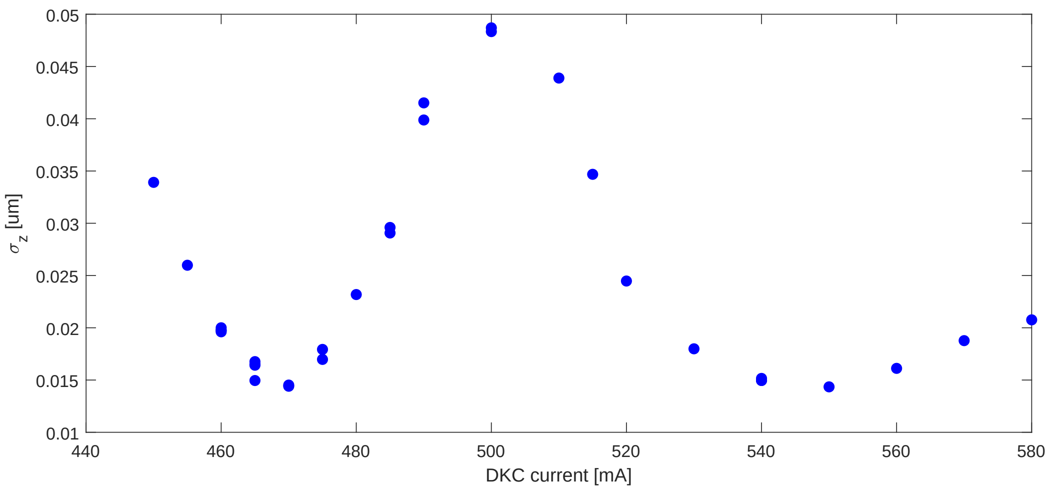

Figure 4.11: Collimation of the BEC vs the DKC current: We apply the DKC pulse and measure the size of the BEC (Gaussian width along the z-axis) after a time of flight of 15 ms. The minimum size is achieved at 470 mA and 550 mA.

Chapter 5

Measurement of the quantum phase of a freely-falling mass

This chapter presents the background and main results of the work leading to the paper "Observation of the quantum equivalence principle for matter-waves" (arXiv preprint arXiv:2502.14535 (2025) [13]).

The next chapter (Ch. 6) provides an in-depth description of the experiment and the main experimental and theoretical results.

5.1 Introduction

Here we present an experiment that measures the quantum phase of a freely-falling massive particle. The experiment is based on a novel matter-wave interferometer, in which ultra-cold atoms are put in a superposition of two trajectories: a freely-falling trajectory (ballistic arm) and a stationary trajectory (reference arm). The phase difference between the two arms is measured, revealing the characteristic t^3 dependence of the phase on the free-fall time t. To honor Galileo's contribution to the study of free fall, we name our new interferometer the Quantum Galileo Interferometer (QGI).

The prediction that an accelerated object, particularly a free-falling object, acquires a phase $\phi \propto mg^2t^3$, was previously made by researches such as Darwin, Kennard, and others [88–95]. Our experiment serves as a direct test and confirmation of these predictions. This phase plays a role in various publications in the context of Einstein's equivalence principle and Galilean invariance in quantum mechanics [96–100]. Recently, it was hypothesized to be a gauge phase between a system at rest in a gravitational field and an accelerated frame in a gravity-free region, presenting itself as an extension of the equivalence principle to the quantum domain [11]. Even more, this phase has been suggested to play a role in a possible unification of quantum theory and the theory of relativity[12, 94].

In Fig. 5.1a, we present a simplified version of the experiment, which we name the *Gedanken* (thought) experiment. In the *Gedanken* experiment, at time $t = t_0$, a beam splitter splits the wave packet into two paths. In one path it is at rest in the lab (so-called Newtonian) frame due to an applied force that exactly counteracts gravity, while in the other, it is in free-fall, i.e., at rest, in the freely-falling (so-called Einsteinian) frame. To achieve recombination of the two paths, the wave packet in the freely falling path is initially launched upwards by the beam splitter with a velocity v_0 in the direction opposite to gravity, and then falls freely for a time $2T = 2v_0/g$ (hereafter referred to as the closing condition), after which an identical beam splitter erases the velocity difference between the two wave packets so that the two paths overlap in position and momentum. In Fig. 5.1b, we present a schematic drawing of our setup in which the chip faces downward, and the interferometer sequence takes place beneath it.

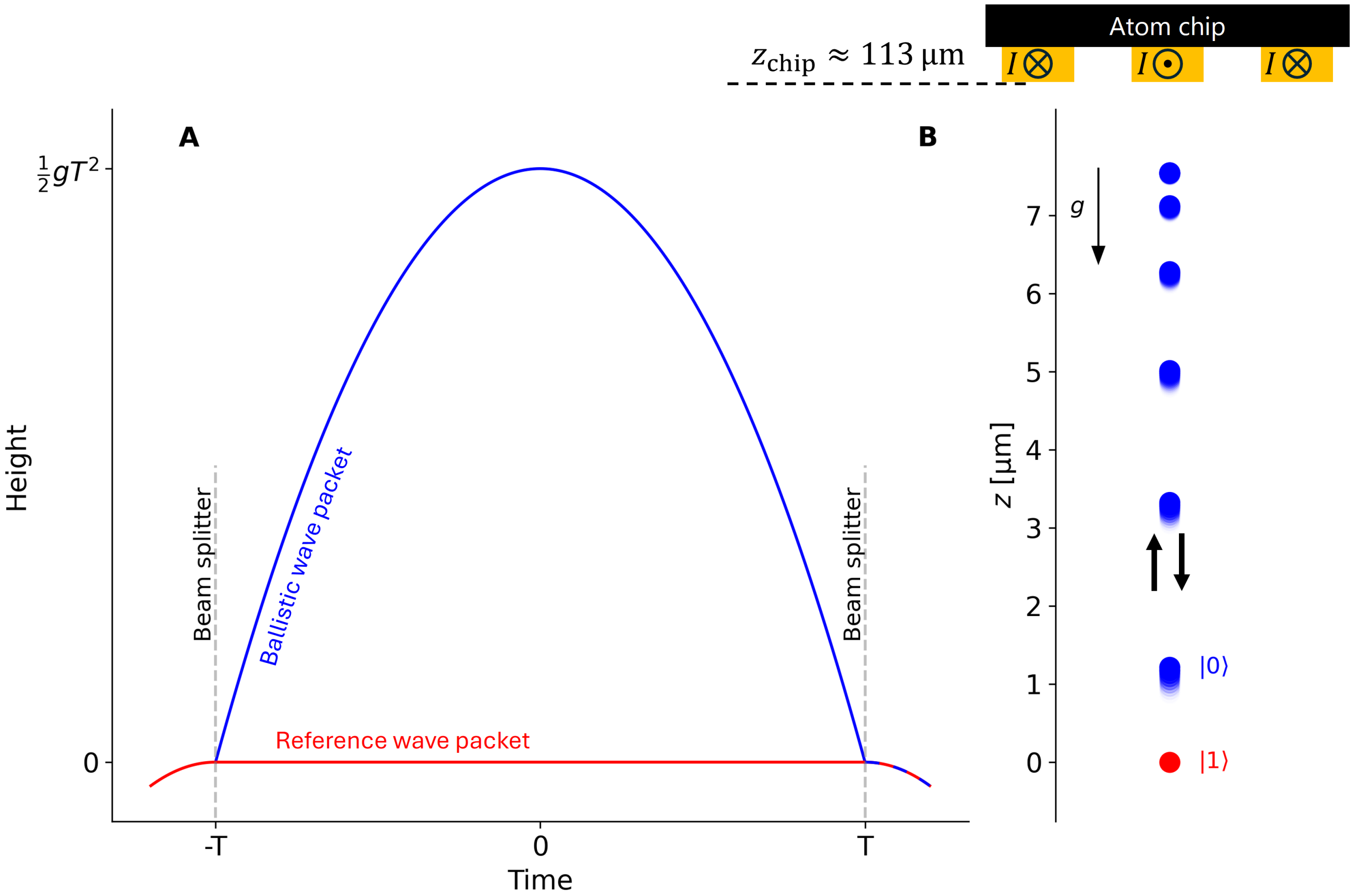

Figure 5.1: The QGI experiment to measure the phase accumulation of a free-falling particle: (a) Space-time diagram illustrating the classical trajectories of the wave packets in the interferometer. A beam splitter creates a coherent superposition of two wave packets with different spin states, launching one wave packet into a freely-falling ballistic trajectory for a duration of $2T$, while the second wave packet is held stationary, serving as a reference. A second beam splitter recombines the two wave packets at the end of the ballistic trajectory. State-dependent detection (not shown) measures the population in each state, revealing the phase difference between the two trajectories. (b) A schematic of our experimental realization: The stationary trajectory is held against gravity using magnetic gradients produced by currents in microfabricated wires on the atom chip. The stationary trajectory, associated with state $|1\rangle \equiv |F=2, m_F=1\rangle$ of a ^{87}Rb atom, is positioned $\approx 113\,\mu$m below the chip surface. The ballistic trajectory, associated with state $|0\rangle \equiv |F=1, m_F=0\rangle$, travels upwards reaching, in this example, a splitting of about $7.5\,\mu$m [about seven times the wave packet size (see Fig. 6.13)]. The interchanging currents in the three wires (shown in the figure) create a 2D quadrupole to realize a strong magnetic gradient with a small magnetic field, which minimizes phase noise (see Fig. 6.7). Taken from [13].

5.2 Experimental scheme

Typical atom interferometers are free-space interferometers, where during most of their motion, the wave packets do not experience any potential applied by the experimental setup [101]. Some interferometers, however, have a potential applied to the wave packets during their evolution, and these can be termed guided interferometers [102, 103]. In our interferometer, both methods are used simultaneously, one for each of the wave packets.

The scheme of the QGI is a variation of the SGI, in which a set of Rabi pulses and magnetic gradient pulses manipulates the two arms. The Rabi pulses control the spin state of the atoms, while the magnetic gradients control their momentum. The scheme is illustrated in Fig. 5.2. An essential aspect of the QGI variation is the use of a two-level system, where one state is magnetically sensitive, and the other is non-sensitive (up to first order in the Zeeman energy). This setup allows us to apply a force to one arm while the second arm is in free fall. We chose the two-level system of the states $|F=2, m_F=1\rangle \equiv |1\rangle$ and $|F=1, m_F=0\rangle \equiv |0\rangle$ to implement this configuration.

We can divide the experiment into three stages: BEC production, preparation of the atoms, and the interferometer. The BEC production is described in detail in Ch. 4. The atom preparation and the interferometer (including the measurement stage) are described as follows:

To prepare the atoms for the interferometer, we first produce a ^{87}Rb BEC consisting of $15-30\times10^3$ atoms in the $|F=2, m_F=2\rangle$ state. We release the BEC from the atom chip trap by shutting off the trapping currents in a linear ramp with a duration of 30 μs, giving the BEC some upward momentum. After a time-of-flight (TOF) of approximately 1100 μs, we apply a delta-kick cooling (DKC) pulse, which collimates the expansion of the BEC (as described in Sec. 4.8) and also gives the atoms an upward momentum kick. We then apply an on-resonance RF π pulse of duration 100 μs to move the atoms from the $|2,2\rangle$ state to the $|2,1\rangle$ state, completing the preparation stage. The atomic cloud density is now low enough to minimize atom-atom interactions, making the physics essentially single-particle.

We first describe the building blocks of the interferometer and then the order in which they are applied. The interferometer scheme (described in Fig. 5.2) consists of four microwave (MW) pulses to manipulate the spin state of the atoms and three magnetic gradient pulses for controlling the momentum of the atoms. The two-level system is controlled by on-resonance MW pulses, with a Rabi frequency $\Omega_R = \frac{2\pi}{32\cdot 10^{-6}} = 2\pi \cdot 31.25\,\mathrm{kHz}$, such that the duration of a π pulse is $16\,\mu$s. The four MW pulses are arranged in a dynamical decoupling (DD) scheme. The symmetry of the DD cancels the linear phase accumulation that rises in the case of undesired detuning of the MW pulses from the resonance, thereby reducing shot-to-shot fluctuations of the phase. It also reduces the effects of inhomogeneity of the resonance within the atomic sample or the magnetic bias field, thus increasing the coherence time of the MW scheme. We define the delay between the $\frac{\pi}{2}$ and π pulses as τ_{DD}, resulting in the scheme $\frac{\pi}{2}, \tau_{DD}, \pi, 2\tau_{DD}, \pi, \tau_{DD}, \frac{\pi}{2}$. The magnetic gradients are arranged to launch one wave packet upwards into a ballistic trajectory with duration $2T$ while keeping the other wave packet stationary and finally stopping the ballistic wave packet when it reaches its initial position, thus recombining the wave packets in both position and momentum. This requires two short, strong pulses with duration T_{kick}, and current I_{kick}, and one longer weaker pulse in between them to hold the reference wave packet against gravity, which we call the holding pulse, and has a duration T_{hold} and current I_{hold}. While in the *Gedanken* experiment the pulses are assumed to be instantaneous, in the actual experiment the pulses have a finite duration and a delay between them, T_d.

The interferometer starts with a $\frac{\pi}{2}$ pulse, which puts the atoms in a superposition of the magnetic sensitive state $|1\rangle$ and the non-sensitive state $|0\rangle$. Next, we apply a short magnetic gradient pulse, which launches state $|1\rangle$ upwards. Shortly thereafter, we apply a π pulse, so that the wave packet launched upwards is in state $|0\rangle$ and is no longer affected by the magnetic gradients, thus going into a ballistic trajectory affected only by gravity (up to first-order Zeeman effect). The other wave packet, which is now in state $|1\rangle$, is held against gravity by the holding pulse. Consequently, this wave packet remains static and does not change position. Finally, we reverse the sequence to bring the two wave packets to the same position and momentum for a full overlap. Let us emphasize that our interferometer is a longitudinal (1D) interferometer, and all positions are along the vertical axis.

The detection stage begins with a $\frac{\pi}{2}$ pulse, which projects the phase difference between the spin states onto the population of the states. To measure the population in each state, we apply another magnetic gradient kick that induces a momentum difference between the two spin states, causing them to become spatially separated after a period of time-of-flight. We can then determine the population in each spin state using absorption imaging with a CCD and measure the interferometer output. As we increase the interferometer duration, we observe oscillations in the population, indicating the increasing phase difference between the two arms.

We use an analytical approximation and a numerical simulation to predict the phase difference of the interferometer. The analytical approximation assumes square pulses of a homogeneous gradient along the z-axis (or equivalently, a linear magnetic potential along the z-axis), leading to purely one-dimensional motion along z, where the acceleration of each arm is a piecewise constant function. Together with the symmetry of the scheme, this results in perfect path recombination. Under these assumptions, the phase difference between the two arms is given by:

$$\Delta\phi = \frac{mg^2}{3\hbar}\left[T^3 + T^2 T_{kick} + T\left(T_{kick}^2 + T_{kick}T_d\right) - T_d\left(T_{kick} + T_d\right)^2\right]. \tag{5.1}$$

See Sec. 6.1 for a detailed derivation.

The case of the *Gedanken* experiment is equivalent to taking the limit of a short kick and short delay, which gives

$$\lim_{T_{kick},T_d \to 0} \Delta\phi = \frac{mg^2}{3\hbar}T^3. \tag{5.2}$$

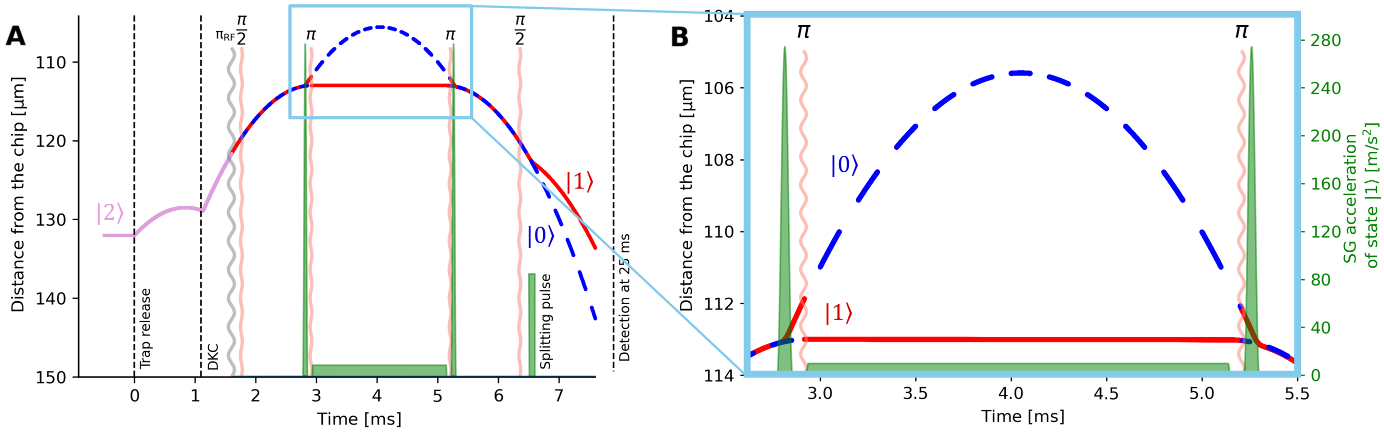

Figure 5.2: (a) The complete experimental scheme of our longitudinal (1D) QGI, for the case of $2T = 2.4\,\text{ms}$. The x-axis is time, where we set $t = 0$ at the moment of trap release. At this time the atoms are in the state $|2\rangle \equiv |F = 2, m_F = 2\rangle$. We apply Delta-kick cooling (DKC) at $t = 1.1\,\text{ms}$, which collimates the wave packet's expansion and launches the atoms into a ballistic trajectory upwards. Before the start of the interferometer, we transfer the atoms to the state $|F = 2, m_F = 1\rangle$ by applying an on-resonance RF π pulse (gray wavy line). During the interferometer, we control the spin state of the atoms with four MW pulses (orange wavy lines) and the momentum of the atoms with three magnetic gradient pulses (green areas). The MW pulses are on resonance with the transition between the $|1\rangle \equiv |F = 2, m_F = 1\rangle$ and $|0\rangle \equiv |F = 1, m_F = 0\rangle$ states, where the $|0\rangle$ state is magnetically non-sensitive in the Zeeman first order. The first $\pi/2$ pulse puts the atoms in an equal superposition of $|1\rangle + |0\rangle$. At the end of the interferometer, the trajectories of these two states are joined to a single trajectory with two spin states, after which the second $\pi/2$ pulse is applied, creating four overlapping wave packets which interfere, two wave packets per each spin state, imprinting the phase difference into a population difference (for simplicity of graphics, we have not differentiated the four wave packets in the plot). After the second $\pi/2$ pulse, we detect the relative population in each state. In the detection scheme, we first spatially separate the states by applying a fourth magnetic gradient and, finally, image the atoms using on-resonance absorption imaging. The symmetric temporal positioning of the $\pi/2$ and π pulses also serves as a dynamic-decoupling scheme, increasing the coherence time, canceling the linear phase accumulation due to possible detuning of the MW and reducing the shot-to-shot phase fluctuations. (b) Zoom-in on the interferometer sequence. The first gradient (kick) pulse applies a maximal acceleration a_{kick} for a total duration of T_{kick}, which launches the top arm into a ballistic trajectory. $50\,\mu\text{s}$ after the end of the gradient pulse, we apply a π pulse (with a duration of $16\,\mu\text{s}$) that inverts the spin state of the arms so that the bottom arm is now in the magnetically-sensitive state $|1\rangle$. $5\,\mu\text{s}$ after the π pulse, we start the holding pulse (duration of T_h and rise time $\tau_h = 12\,\mu\text{s}$), which applies an acceleration opposite and equal to gravity, to hold the bottom arm stationary in the lab frame. $50\,\mu\text{s}$ after the holding pulse, we again apply a π pulse and $5\,\mu\text{s}$ later we recombine the trajectories of the two wave packets by applying a magnetic gradient pulse with a maximal acceleration a_{kick} for a total duration of T_{kick}, as in the first pulse. Taken from [13].

5.3 Results

In Fig. 5.3, we present the interferometer output, that is, the population in state $|0\rangle$, as a function of the interferometer duration. We observe 13 oscillations, which constitute about 80 rad phase accumulation. We extract the phase of the interferometer by fitting the oscillations and present it in Fig. 5.4 where we compare the experimental result to the numerical simulation, the analytical prediction of Eq. 5.1 as well as to the *Gedanken* experiment given in Eq. 5.2. In addition to the main origins of phase accumulation, the numerical simulation takes into account (i) three-dimensional propagation in a curved potential resulting in non-perfect path recombination, (ii) internal wave packet dynamics (expansion, focusing, and rotation), and (iii) atom-atom interactions within each wave packet. The first two factors may change the phase by 1-2 radians, while the latter may contribute up to 0.25 radians. The prediction of the numerical simulation is accurate within the uncertainty limits of the experimental parameters. The model at the base of the numerical simulation is described in Sec. 2.1.2.

The primary source of uncertainty in the experimental results arises from the systematic uncertainty in the ratio of the kick and holding currents, as the phase accumulation is most sensitive to this ratio. Deviations from the desired ratio add a phase term that scales linearly with the interferometer time.

As shown in Fig. 5.4b, the residuals amount to about 2.5%, showing good agreement between the model and the data.

In Ch. 6, we provide detailed information on the data analysis of Figs. 5.3 and 5.4, together with more details on the experimental setup and the numerical simulation.

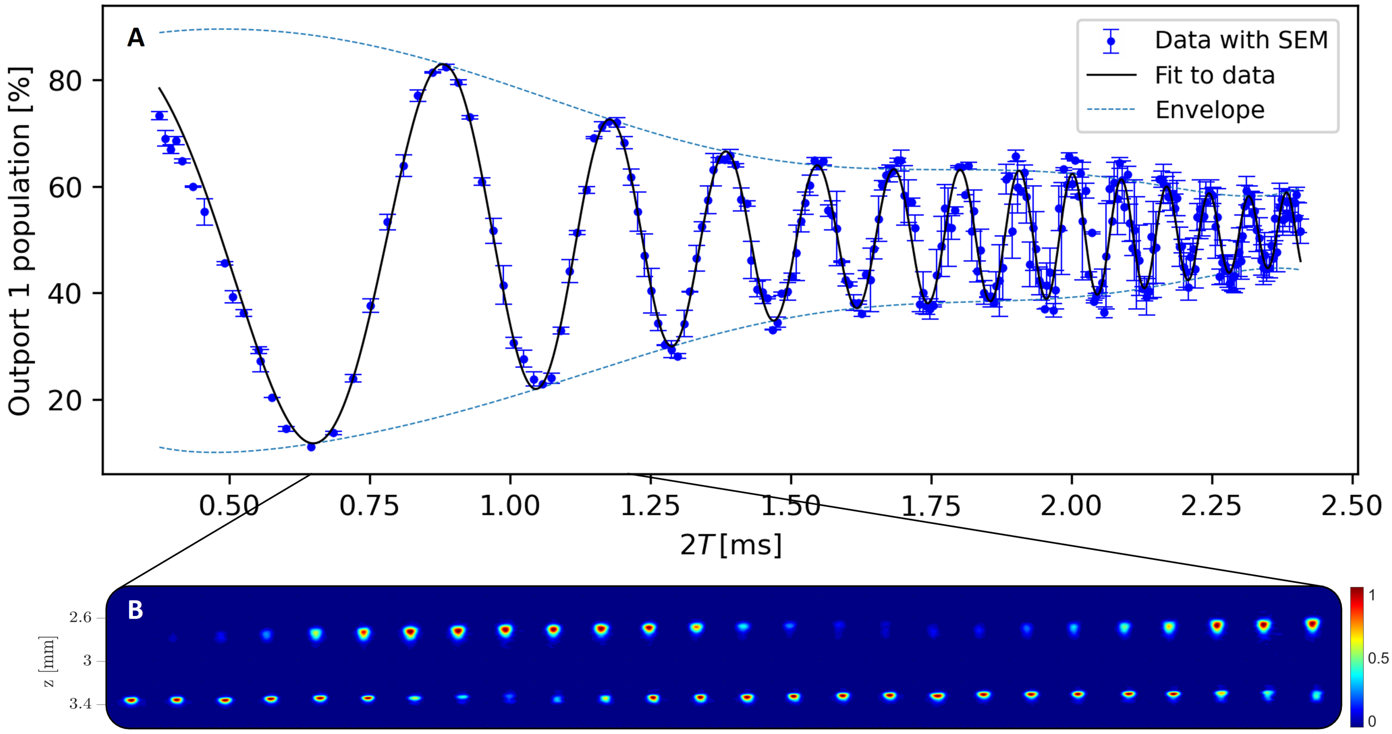

Figure 5.3: Population in outport 1 vs. the free-fall duration of the ballistic path $2T$: (a) The relative spin population in outport 1 (state $|0\rangle$) oscillates with a distinct chirp as a function of interferometer time. The blue points represent the experimental data, with error bars derived from the standard error of the mean (SEM). The black line is a fit to the data of the form $P = P_{\text{mean}}(2T) + \frac{1}{2}V(2T)\cos[\phi(2T)]$, where V is the visibility of the oscillations, ϕ is the phase of the oscillations and P_{mean} is the mean value of the population. To obtain the fit, we first identify the upper and lower envelopes and fit them to a polynomial to get P_{mean} and $V(2T)$. We then fit the data to the model where the phase $\phi(2T)$ is a third-order polynomial. During the fitting, we exclude the first and last oscillation as they suffer from larger uncertainty in the values of the envelope. The data shows 13 complete oscillations with low phase noise, resulting in an average population error (SEM) of 1.8 ± 1.5 [%] and good visibility, starting at $V = 80\,\%$ and decreasing to $V = 20\,\%$ at $2T = 2000\,\mu$s. The decrease in visibility is mainly due to a varying overlap between the wave packets caused by differences in shape evolution under the influence of curved gradients, as well as imperfections in the path recombination. The figure includes 633 experimental cycles, each lasting 30 s, resulting in a graph taken over a period of 5.3 hours. The short and long-term stability of the interferometer is good due to the high stability of the chip trap, and current source. (b) CCD images of the atoms in the two outports taken with on-resonance absorption imaging, showing one and a half oscillations. The top cloud is outport 1 (state $|0\rangle$), and the bottom cloud is outport 2 (state $|1\rangle$, which is magnetically sensitive), Z represents the distance from the chip, and the heatmap shows the relative optical density. The cloud in outport 2 is focused by the final splitting pulse, increasing its optical density, and making it appear slightly brighter even when the two clouds have the same population. Taken from [13].

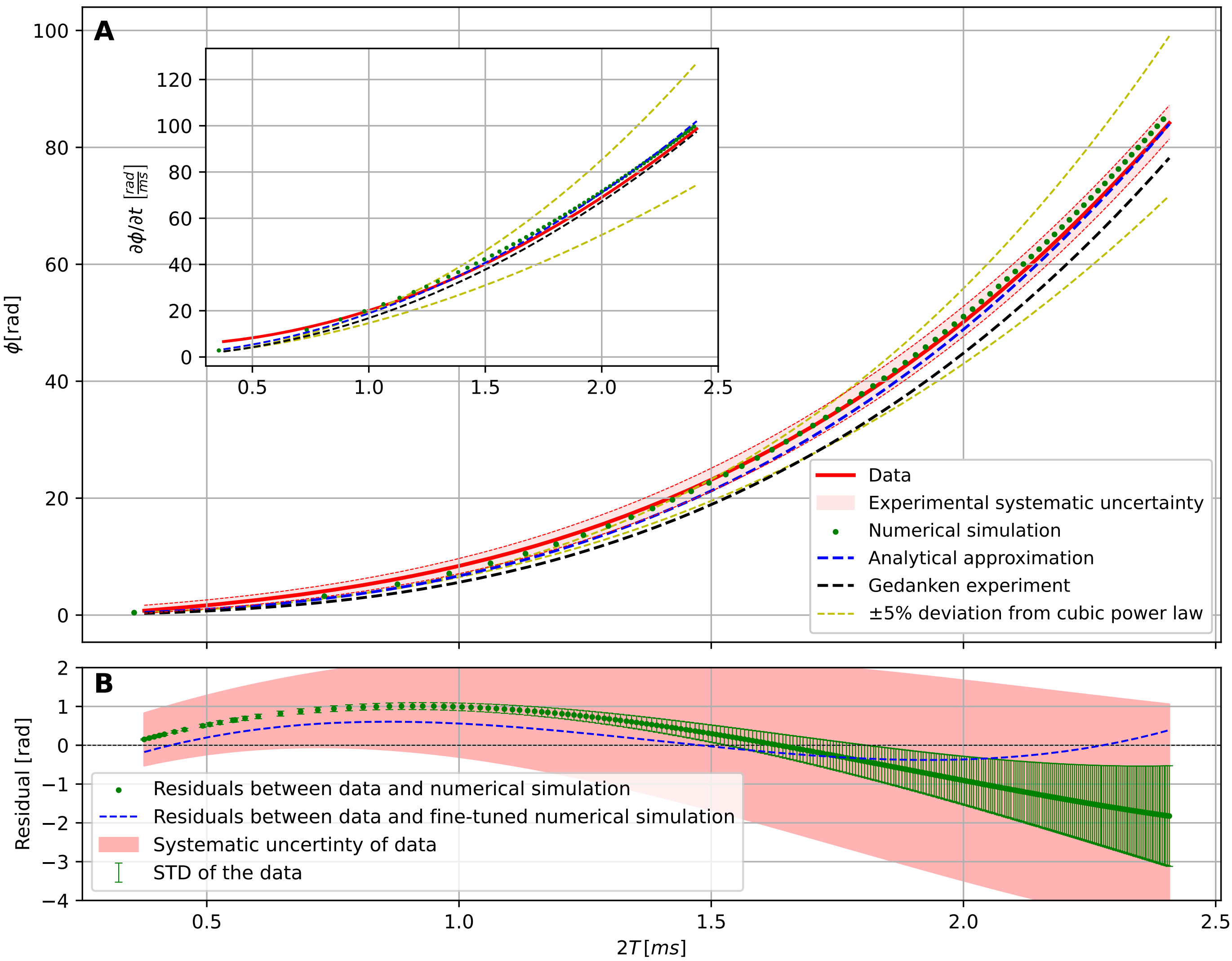

Figure 5.4: Phase and its derivative vs. the free-fall duration of the ballistic path $2T$: (a) The phase difference between the two interferometer arms as a function of the free-fall duration of the upper arm. The red line represents the experimental data, where the phase is extracted from Fig. 5.3. To estimate the uncertainty bounds, we repeat the experiment with an increase (decrease) of the magnetic-pulse current I_{kick} by 0.5 % (which is our estimated experimental precision) and use the result to plot the upper (lower) uncertainty bounds. The green points are the result of the numerical simulation based on tools we developed for calculating wave packet evolution (see [56] and Sec 2.1.2), which include the effects of shape and rotation of the wave packet. The blue dashed line is the result of the analytical approximation of the experiment given in Eq. 5.1, which assumes that the acceleration of each arm is a piecewise constant function. The black dashed line depicts the phase of the *Gedanken* experiment. The inset shows the derivative of the phase with respect to $2T$. To obtain the derivative of the phase for the numeric simulation, we fit a third-order polynomial to the set of points in the main figure and take its derivative. The derivative of the analytical approximation and the *Gedanken* experiment are calculated by direct differentiation. The yellow dashed lines represent 5% deviations from the T^3 phase accumulation model, by modifying the analytical prediction to a power law of $T^{3\pm0.15}$. This is meant to show that the data is not consistent with such deviations from the cubic phase. (b) The residuals between the phase of the data and the numerical simulation, where the latter is a "blind" simulation with no free parameters or fine tuning. A difference of 2 rad over 13 oscillations spanning a phase of ≈ 80 rad, constitutes a deviation of about 2.5%. The error bars represent the statistical noise of the phase in the experiment, which shows a relative noise of 1.3% of the phase. The red band represents the systematic uncertainties [which also appear in (a)]. The blue line shows the result of the numeric simulation after fine-tuning of the currents and the magnetic field along the z-axis. The kick current is increased by 0.15% , the idle current is changed from 0.55 mA to 0.5 mA, and B_z from 0.33 G to 0.35 G, all within the experimental uncertainties. Taken from [13].

5.4 Discussion

Since the time of Galileo and Newton, it has been clear that the phenomenon of free-fall in a gravitational field is a paradigm of physics and must be fully understood as part of any description of nature. Galileo's quantitative assessments of the gravitational acceleration mark a turning point in modern science [104]. Newton's law of gravity united the earthly experience of free fall with the motion of the stars in the sky above us. Einstein went a step further and used the geometry of space-time to describe gravity and free-fall.

Surprisingly, despite the rich history of matter-wave experiments, the numerous efforts to unite the theory of gravity with quantum mechanics, and the prediction of the phase of a freely falling particle almost a century ago [89], the quantum phase of a freely-falling massive particle had not been measured until now.

While measuring gravity with matter-wave interferometers has been previously achieved with neutrons in the celebrated Colella-Overhauser-Werner (COW) experiment [105] (as well as by Bonse and Wroblewski for a noninertial frame [106]), and with atoms [107–111], the explicit phase of a free-falling wave packet has not been directly measured, as these interferometers measure a phase that is linear or qudratic in time.

A cubic phase dependence on the interferometer time may also appear in a few standard-practice interferometers [112–115]. Still, these interferometers do not measure the phase of a free-falling particle but rather measure other accelerations.

A direct measurement of the phase of a freely-falling mass requires a superposition of a free-falling trajectory with a stationary trajectory, which is realized by the QGI, thus establishing a direct test and confirmation of the phase of a free-falling object.

We have developed a unique interferometer, the QGI. While the Ramsey-Bordé interferometer is mostly characterized by the constant spatial separation between the two paths [116], and the Kasevich-Chu interferometer by the piece-wise constant velocity separation (difference) between the two paths [33], the QGI enables the control of all degrees of freedom, allowing spatial, velocity, and acceleration differences, almost at will. This allowed us to have one wave packet at rest and the other free-falling.

As this quantum phase involves the comparison of two fundamental reference frames, the rest frame and the free-falling frame, it has already been introduced in many fundamental theoretical inquiries regarding the interface of quantum mechanics and gravity, although usually as the phase of a single wave packet, and not as the phase difference between two parts of a superposition. We hope this new experiment and its results will serve as a unique tool in probing this interface and as a base for further investigating such fundamental questions [117, 118].

As an outlook, let us note two important points: First, as our unique interferometer is also able to manipulate clock wave packets (for clocks in a SGI, see [46]), it opens the door for investigating more complex formulations suggested for the equivalence principle in the quantum domain. It also paves the way for searches for new physics [119]. Second, it represents a milestone toward developing a SGI with nano-diamonds instead of atoms. This advancement will allow us to test quantum mechanics in new regimes and to probe the quantum-gravity interface, e.g., test the quantization of gravity [15]. In addition, such a large-mass interferometer can explore the Díosi-Penrose conjecture regarding gravitationally-induced collapse.

Chapter 6

Details of the experimental realization

We present the details of the experimental realization of the QGI. This chapter presents the work that is the basis for the supplementary material of the paper "Observation of the quantum equivalence principle for matter-waves" (arXiv preprint arXiv:2502.14535 (2025) [13]), and accordingly, there is some overlap between the two.

We start by providing a detailed derivation of the phase in the analytical model and then give the details of the numerical simulation and the data analysis. We continue to present the details of the experimental realization, including the magnetic potential, the magnetic field gradients, and the characterization of the trap. We conclude with additional information on the wave-packet size and the trajectories during the QGI.

6.1 Analytical model for calculating the phase

This section describes the derivation of the analytical model of the QGI and is adapted from the supplementary material of [13].

In the following derivations, the analytical model approximates the experiment as a set of square pulses of a homogeneous magnetic gradient so that the acceleration of each arm is a piecewise constant function. This simple model is a good approximation of the experiment and allows us to understand the behavior of the interferometer. While it is possible to calculate an analytical prediction that includes the real temporal shape of the magnetic gradient pulses, it is not necessary for the purpose of this work, as this analytical model approximates the real experiment well, and anyway, the more realistic case is calculated by a numerical simulation. The analytical model does not include the effect of the shape of the wave packets on the phase, while the numerical simulation does.

Given the assumptions above, the experiment can be described by a set of durations and the acceleration of each arm during each duration.

We define the total interferometer time as $2T + 2T_{kick}$, and the holding duration of the bottom arm can be defined as $T_h = 2T - 2T_d$. The experiment can be described by the set of durations

$$(T_{kick}, T_d, T_h, T_d, T_{kick}) \tag{6.1}$$

where the acceleration of the ballistic and reference paths in each of these durations is given by

$$a_{\text{ballistic}} = -g + (a_{kick}, 0, 0, 0, a_{kick}), \tag{6.2}$$

and,

$$a_{\text{reference}} = -g + (0, 0, a_{hold}, 0, 0). \tag{6.3}$$

The phase of the interferometer is given by the action along the classical path

$$\phi_j = \frac{1}{\hbar} S_j = \frac{1}{\hbar} \int_0^{t_f} [K_j(t) - U_j(t)] \, dt, \tag{6.4}$$

where j is an index of the respective interferometer path, and

$$K_j(t) = \frac{1}{2} m v_j^2(t) \ , \ U_j(t) = -m a_j(t) [z_j(t) - z_0] \, , \tag{6.5}$$

where z_0 is defined by the zero of magnetic potential, $|B(0, 0, z_0)| = 0$, which is the position of the magnetic field quadrupole in the experiment (not to be confused with the initial position of the atoms $z_i(0)$). In the case of a closed interferometer, the phase does not depend on z_0. For an open interferometer, the phase will depend on z_0 and will include the contribution of the separation phase (Eq. 2.19).

The condition for a closed interferometer is an equal area of the accelerations of the two arms (see Sec. 6.2)

$$\int_{t_i}^{t_f} a_1(t)dt = \int_{t_i}^{t_f} a_2(t)dt \tag{6.6}$$

which, in this case, give

$$a_{kick} \cdot 2T_{kick} = a_{hold} \cdot T_h \,. \tag{6.7}$$

Setting $a_{hold} = g$ confirms that the reference path does not accelerate in the lab frame during the holding pulse.

In the *Gedanken* experiment, the trajectories are symmetric around the middle point (the turning point of the ballistic path), and the reference arm is stationary in the lab frame. To maintain the symmetry of the trajectories in the case of a finite duration of the pulses, we set the initial conditions of the COM of the wave packet to be

$$v_z(0) = g(T_{kick} + T_d) \quad ; \quad z(0) = -g(T_{kick} + T_d)^2/2 \,, \tag{6.8}$$

which also sets the velocity of the reference arm to zero during the holding pulse, making it stationary in the lab frame. (as the reference arm is in free fall during the initial and final duration of $T_{kick} + T_d$).

Performing the integrals, we get

$$\phi_1 = \frac{mg^2}{3\hbar}\left(-T^3 - T^2T_{kick} - TT_{kick}^2 - TT_{kick}T_d + 2T_{kick}^3 + 7T_{kick}^2T_d + 8T_{kick}T_d^2 + 3T_d^3\right) \tag{6.9}$$

$$\phi_2 = \frac{2mg^2}{3\hbar}\left(T_{kick} + T_d\right)^3 \tag{6.10}$$

$$\Delta\phi = \frac{mg^2}{3\hbar}\left[T^3 + T^2T_{kick} + T\left(T_{kick}^2 + T_{kick}T_d\right) - T_d\left(T_{kick} + T_d\right)^2\right] . \tag{6.11}$$

Taking the limit of a short kick we get

$$\lim_{T_{kick}\to 0}\Delta\phi = \frac{mg^2}{3\hbar}\left(T^3 - T_d^3\right) \ , \tag{6.12}$$

and in the limit of short delay we get

$$\lim_{T_{kick},T_d\to 0}\Delta\phi = \frac{mg^2}{3\hbar}T^3. \tag{6.13}$$

Eq.6.13 represents the *Gedanken* experiment in which the beam splitter is a delta pulse such that $T_{kick}, T_d \to 0$.

The trajectories of the two arms in the three cases of Eqs. 6.11,6.12,6.13 are shown in Fig. 6.1.

The result of the analytical model given in Eq. 6.11 is plotted in Fig. 5.4, using the experimental values of $T_{kick} = 80\,\mu$s and $T_d = 71 + 6\,\mu$s where we include half the rise time of the holding pulse $\tau_{\text{hold}}/2 = 6\,\mu$s in the delay.

We also include the contribution to the phase from the force on the state $|0\rangle$ due to the second-order Zeeman (SOZ) effect. This force is opposite to the force on the $|1\rangle$ state during the gradient pulses, and its value is about 1% of the latter. During the holding pulse, the acceleration of the state $|0\rangle$ due to SOZ is calculated to be $a_{SOZ} = 0.10\,\text{m/s}^2$ (see Sec. 6.6.1) for details). We include this effect in the analytical prediction for the phase [Eq. (5.11)] by replacing the gravitational acceleration g by $g_{\text{eff}} = g + a_{\text{SOZ}} = 9.91\,\text{m/s}^2$. This estimation agrees with a model in which a_{SOZ} is explicitly included in the calculation to within 0.03 rad.

An analytical calculation can also include the temporal shape of the pulses and account for time-dependent homogeneous magnetic pulses. However, for the scope of this work, we choose to present the analytical prediction only for the more straightforward case of piecewise constant acceleration and use the numerical simulation to include the temporal and spatial modulation of the gradients.

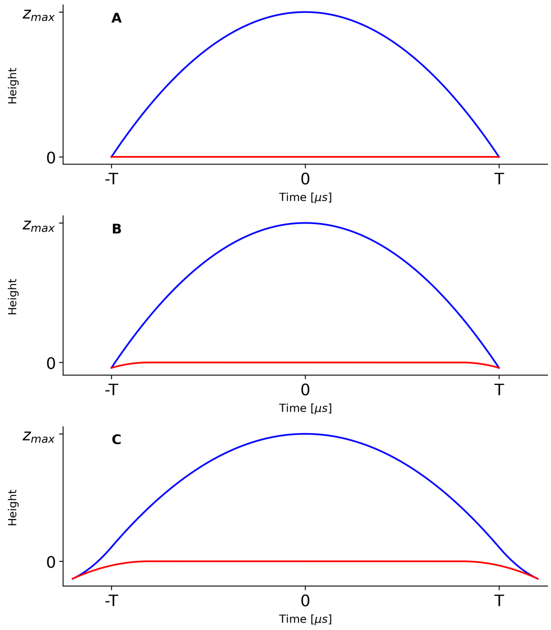

Figure 6.1: Trajectories in the analytical approximation for three limiting cases: In each plot, the blue line represents the trajectory of the ballistic wave packet and the red of the reference wave packet. (a) In the *Gedanken* experiment case, the ballistic wave packet freely falls for duration $2T$, while the reference wave packet is stationary for the same duration. The beam splitter is a delta pulse and $T_{kick}, T_d \to 0$ (Eq. 6.13). (b) The case of Eq. 6.12 includes a finite delay T_d between the beam splitter and the holding. The reference wave packet freely falls during the short delay time T_d and is held stationary for a duration $T_h = 2T - 2T_d$. (c) Including a finite duration of T_{kick} (Eq. 6.11), the ballistic wave packet experiences upward acceleration for a duration T_{kick}. In all cases, the trajectories are symmetric around the middle point, where the ballistic path is at the turning point (set as t=0 in these plots).

6.2 Conditions for a closed interferometer

A closed interferometer is defined by both arms having the same final position and momentum. We can characterize the trajectories of the two arms using

$$\begin{aligned}\Delta a(t) =& a_2(t) - a_1(t) \\ \Delta v(t) =& v_2(t) - v_1(t) \\ \Delta z(t) =& z_2(t) - z_1(t) \ ,\end{aligned} \tag{6.14}$$

such that a closed interferometer is defined by $\Delta v(t_f) = 0$, $\Delta z(t_f) = 0$. We will now show that for a symmetric interferometer scheme, there is a simple law of equal areas of acceleration, which ensures a closed interferometer.

First, we require that $\Delta v(t_f) = 0$; from that we can write

$$v_1(t_f) = v_1(t_i) + \int_{t_i}^{t_f} a_1(t)dt = \int_{t_i}^{t_f} a_2(t)dt + v_2(t_i) = v_2(t_f), \qquad (6.15)$$

by definition $v_1(t_i) = v_2(t_i)$ we get

$$\int_{t_i}^{t_f} a_1(t)dt = \int_{t_i}^{t_f} a_2(t)dt \qquad (6.16)$$

This is the law of equal areas of acceleration, which can be also written as

$$\int_{-T}^{T} \Delta a(t)dt = 0. \qquad (6.17)$$

We consider a symmetric interferometer, where the interferometer starts at $t = -T$ and ends at $t = T$, and the acceleration is symmetric under inversion around $t = 0$

$$a(t) = a(-t), \qquad (6.18)$$

Due to the symmetry of $a_i(t)$ we get

$$\int_{0}^{T} \Delta a(t)dt = \int_{-T}^{0} \Delta a(t)dt = 0. \qquad (6.19)$$

which gives us

$$\Delta v(0) = \int_{-T}^{0} \Delta a(t)dt = 0 \qquad (6.20)$$

so that halfway through the interferometer the differential velocity is zero.

We can show that $\Delta v(t)$ is an antisymmetric function. By definition:

$$\Delta v(t) = \int_{0}^{t} \Delta a(t')dt', \qquad (6.21)$$

by substitution of $t' \to -t'$

$$\Delta v(t) = \int_{0}^{t} \Delta a(t')dt' = -\int_{0}^{-t} \Delta a(-t')dt' = -\int_{0}^{-t} \Delta a(t')dt' = -\Delta v(-t) \qquad (6.22)$$

An integral of an asymmetric function (over a symmetric domain) is zero, which in this case results in zero final spatial splitting, $\Delta z(t_f) = 0$. We can directly calculate this by

$$\Delta z(t_f) = \int_{-T}^{T} \Delta v(t) dt = \int_{-T}^{0} \Delta v(t) dt + \int_{0}^{T} \Delta v(t) dt = \int_{0}^{T} \Delta v(-t) dt + \int_{0}^{T} \Delta v(t) dt = 0 \tag{6.23}$$

This concludes the proof that in the case of a symmetric interferometer scheme, the law of equal areas of acceleration ensures a closed interferometer.

6.3 Numerical simulation

In this section, we provide details of the numerical simulation (taken from the supplementary material of [13]). The model for the numerical simulation is described in 2.1.2.

6.3.1 Details of the numerical simulation

The numerical simulation calculates the dynamics of the atomic BEC during the trapping, release, DKC, and interferometer sequence. The simulation is based on the model of wave packet evolution given in [56], which is extended to include the effects of rotations. To use the model with curved magnetic potentials, we locally approximate the magnetic potential by a quadratic potential and calculate the evolution of each wave packet in the potential. The simulation predicts the output of the SGI by calculating the overlap integral of the two final wave packets, resulting in a complex value, where the visibility is the magnitude of this integral and the phase is the argument.

The simulation is constructed to mimic the exact experimental sequence by using the same timings as in the experiment. During the preparation stage, the currents and magnetic fields in the simulation are kept close to the values reported in the experiment but fine-tuned to match the wave packet's initial conditions, such as initial position and velocity, and initial expansion rate. As the measurements of the absolute positions of the atoms are accurate up to a few μm, other indications of the position of the atoms in the lower interferometer arm are also taken from the holding current required to hold the atoms against gravity, and the trajectory after the DKC. A holding current of 23-24 mA corresponds, according to the calculation, to a distance of 112-113 μm from the chip surface. Assuming that the velocity of the atoms at this position before turning on the holding pulse is almost zero, we can deduce the trajectory after the DKC as the atoms are in free fall and hence travel a distance $\Delta z = \frac{1}{2}gt^2$. This calculation indicates a distance of about 132 μm from the chip surface for the initial trapping position. These values of the initial trap and turning point agree with direct measurements from the experiment.

The magnetic bias field is taken to be the field generated by the bias coils and Earth's magnetic field $\mathbf{B}_E = (-0.31, 0, 0.33)\,$G. The bias generated by the coils consists of a component in the y direction and in the x direction, which are determined to be $B_{0y} = 12.9928\,$G and $B_{0x} = -1.175\,$G. The y-component of the field during the trapping determines the trap position with respect to the chip surface and the x-component determines the trap frequency and field at the bottom of the trap. The total magnetic field magnitude is indeed measured some time after trap release by the RF transition frequency between the Zeeman levels $|2,2\rangle$. and $|2,1\rangle$. This measurement indicates that the total field at this time is $B_0 = 12.625\,$G, but we take the field during the trapping to be $B_0 = 13.05\,$G to ensure that the trapping position is about 132 μm from the chip surface, which is consistent with the position of the atoms in the lower arm of the interferometer, as described above. The discrepancy between the measured bias field after the trap release and the predicted bias field required to explain the trapping stage may be attributed to the magnetic response of the atom chip mount and the chamber itself, resulting in transient fields in the science chamber during the trapping. Time dependence of the bias field after the trap release and DKC is observed in the RF resonance measurements. The z-component of the magnetic field generated by Earth is responsible for a shift of the trapping position relative to the center of the system and we find numerically that the trapping position is at $\mathbf{r}_{\mathrm{trap}} = (0.79, 4.67, 132.05)\,\mu$m relative to the center of the surface of the central wire. The trapping frequencies are $\omega_y \approx \omega_z \approx 2\pi \times 1.04\,$kHz and $\omega_x \approx 2\pi \times 57\,$Hz, which is in good agreement with the measured trap frequencies. The calculated field at the bottom of the trap is $B_0 \approx 0.825\,$G, which is slightly larger than the measured value. For a total number of $2 \cdot 10^4$ atoms, we obtain a BEC of an average width $\sigma_x = 3.13\,\mu$m in the longitudinal direction and $\sigma_y = \sigma_z = 1.31\,\mu$m in the transverse direction. This serves as the starting point for calculating the evolution of the wave packet widths during the sequence. The constant bias field also includes a measured gradient $B' = 68.32\,$G/m, giving rise to an acceleration $\mu_B B'/2m = 0.22\,$m/s^2 in the direction of gravity. The DKC pulse kicks the atoms upwards, and after it, the atoms are in free fall until the beginning of the interferometer, except that they are affected by small magnetic gradients from the bias field and an idle current from the kick wires on the chip. During this time, they are transferred from the state $|2,2\rangle$ to the state $|2,1\rangle$ by a RF pulse that ends about $400\,\mu$s after the collimation pulse and then they are split into a superposition of $|2,1\rangle$ and $|1,0\rangle$. As the idle current is designed to counteract the magnetic gradient of the bias during the time between the splitting $\pi/2$ pulse and the recombining $\pi/2$ pulse we may consider the trajectory of the atoms before the kick pulse as being ballistic and calculate the timing and position of the turning point where the atoms are expected to have a zero velocity. This point z_h is located at a distance $z_h - z_{\text{DKC}} = \frac{1}{2}gt^2_{\text{free}}$ from the position z_{DKC} at the end of the collimation pulse. At this point, the holding current I_h is calculated and the kick current I_k is also calculated such that the holding current and kick currents satisfy $2I_kT_k = I_hT_h$. The DKC is optimized to yield a zero velocity of the atoms at the beginning of the holding pulse such that the lower trajectory is constant during the holding time. The ballistic trajectory is calculated based on the calculated kick current and the second-order Zeeman effect is taken into account during the holding time of the lower arm, as well as the effect of the second-order Zeeman over the whole sequence.

The free parameters of the simulation are the bias field in the x and y directions and the exact value of the collimation current. When these parameters are varied under the constraint that the lower arm trajectory is flat and at the correct distance from the chip surface, the interferometer phase varies within a range of $\pm 0.07\,$rad at the longest holding time. Note that these parameters were not used for fitting the phase but rather to fit other parameters of the experiment mentioned above; thus the numerical simulation curve in Fig. 5.4 can be considered as a curve without fitting parameters related to the phase.

In addition, the second simulation curve [blue line in Fig. 5.4b] represents an attempt to best fit the experimentally measured phase without exceeding the uncertainty range of the parameters, with the price of the lower arm trajectory not being flat. In the latter simulation, the holding current was taken to be 23.5 mA (although a larger current was required to hold the reference arm against gravity), and the DKC current was taken to be 0.4705 mA (instead of 0.4695 mA for the first simulation). The kick current was taken larger by 0.15%, the idle current was taken to be 0.5 mA instead of 0.55 mA, and B_z was taken to be 0.35 G instead of 0.33 G. All these changes are well within the uncertainty limits of the experimental parameters.

6.3.2 Effect of wave packet shape on the phase

The numerical simulation includes the effect of the wave-packet shape, which evolves due to single particle effects (momentum uncertainty of the wave packet and response to the curved potentials) and atom-atom interactions. To estimate the effects of the wave-packet shape on the phase, we compare the total phase calculated from the overlap integral to the phase of the classical trajectory of the COM. The result is shown in Fig. 6.2. The total phase accumulation in the experiment amounts to 80 rad while the contribution due to the shape of the wave packet is in the range of 0 to 1 rad. The relative contribution of the "non trajectory" phase is as high as 7% for short interferometer durations but decreases for longer interferometer times. The exact contribution due to the shape of the wave packet depends on the exact shape of the wave packet and the specific experimental conditions, and can be one of the sources of the discrepancy between the numerical simulation and the experimental data. The numerical simulation also includes the effect of the ambient gradient in the chamber, which was measured to be 0.7 G/cm (equivalent to an acceleration of 0.2 m/s^2 along gravity of the $|1\rangle$ state, see Sec. 6.5.2 for more details) and the idle current of 0.55 mA we apply to counteract the effect of the ambient gradient. The shape of the pulses of current in the SG wires is also included in the simulation. A detailed description of the pulses is given in Sec. 6.6.3.

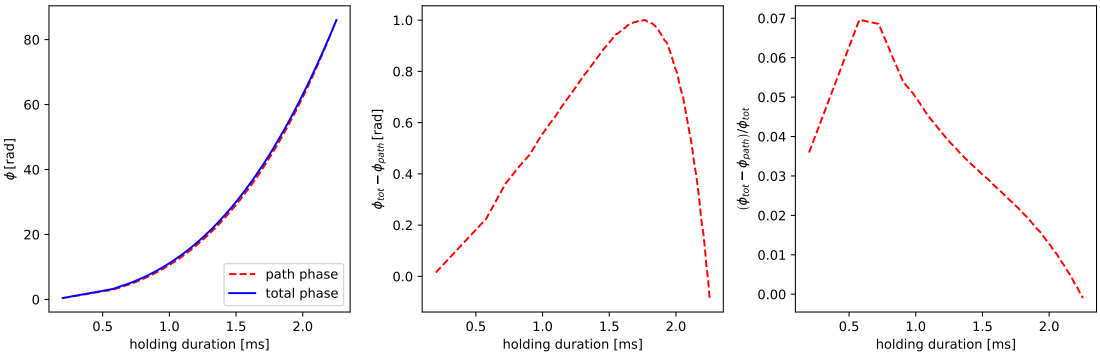

Figure 6.2: The different phase contributions calculated in the numerical simulation: (a) The total phase (blue solid line), was calculated from the overlap integral between the two wave packets at the end of the interferometer (the timing of the last $\pi/2$ pulse). This total phase takes into account the effects of wave packet shape and atom-atom interaction. The red dashed line is the "path phase", the phase accumulation due to the classical trajectory of the COM. (b) The difference between the two calculations, shows that the "non trajectory" contributions range between -1.1 to 0.4 rad, out of the total 80 rad of the interferometer. (c) The relative part of the "non trajectory" is as high as 15% for short interferometer duration but decreases to less than 2% for durations longer than 1.2 ms. Taken from [13].

6.4 Data analysis

In this section, we provide the details of the data analysis of the experiment (taken from the supplementary material of [13].)

To extract the phase from the raw data of population vs. time, we fit the data to a model $P = P_{\text{mean}}(2T) + \frac{1}{2}V(2T)\cos[\phi(2T)]$, where V is the visibility of the oscillations, ϕ is the phase of the oscillations and P_{mean} is the mean value of the population. To obtain the fit, we first identify the upper and lower envelopes and fit them to a polynomial to get P_{mean} and $V(2T)$. We then fit the data to the model where the phase $\phi(2T)$ is a third-order polynomial. During the fitting, we exclude the first and last oscillations as they suffer from larger uncertainty in the values of the envelope. As fitting such a model to the data requires a good initial guess, we use the Hilbert transform [120, 121] to extract the phase from the data. The details of the analysis are given below.

6.4.1 Fitting the population vs. time data and extracting the phase

We fit the data of population vs. time with the following algorithm: First, we fit the envelope of the oscillations by identifying the local maxima (minima), connecting them with a set of straight lines, and fitting them to a polynomial. For the data in Fig. 5.3, a polynomial of order seven was used for the envelopes. Once we have an equation for the upper and lower envelope, we calculate the local amplitude $V/2(2T)$ and local mean $P_{mean}(2T)$. We then apply the Hilbert transform, which results in a complex number for each data point, whose argument is the phase up to $2\pi n$, so we unwrap the phase of the whole data, which requires a high enough sampling rate in each oscillation. At this point, we fit a third-order polynomial to obtain a smooth function $\phi(2T)$. We use this polynomial as the initial guess for the final fit of the population. While the Hilbert transform is a powerful tool for extracting the phase, it introduces significant edge effects, which are hard to avoid. The direct fit of the phase to the data is more robust against edge effects and is thus used for the final fit of the data.

6.4.2 Phase

In Fig. 5.4, we show the phase derived from the experimental data against three calculations of $\phi(2T)$: the numerical simulation, the analytical approximation, and the expected phase in the *Gedanken* experiment. We calculate the lines of the analytical approximation and the *Gedanken* experiment using Eq. 6.11 and Eq. 6.13 respectively. The line of experimental data was derived by a fit to the data of Fig. 5.3 (as explained above), and the data points of the numerical simulation were derived as explained in Sec. 6.3. We also plot as a guide to the eye deviations from the T^3 phase accumulation, by plotting a modified version of the analytical approximation,

$$\Delta\phi = \frac{mg^2}{3\hbar}\left[\left(\frac{mg^2}{3\hbar}\right)^{\frac{\alpha}{3}} T^{3+\alpha} + T^2 T_{kick} + T\left(T_{kick}^2 + T_{kick}T_d\right) - T_d\left(T_{kick} + T_d\right)^2\right], \tag{6.24}$$

where we set $\alpha = 0.15$ to show 5% deviation from the T^3 phase accumulation, and the coefficient $\frac{mg^2}{3\hbar}^{\frac{\alpha}{3}}$ is added to maintain the correct units. The conditions that define the phase in interest are that the interferometer is closed and the reference arm is stationary. The closing condition is best approximated by the law of equal areas of current. We found experimentally, analytically, and numerically, that phase is much more sensitive to small deviations from the equal areas of current than to small deviations from the flatness of the reference arm. Thus to estimate the uncertainty bounds of the phase, we repeat the experiment with an increase (decrease) of the magnetic-pulse current I_{kick} by 0.5 % (which is our estimated experimental precision on this parameter). We use the result to plot the upper (lower) uncertainty bounds of the phase. The inset shows the rate of phase accumulation $\frac{\partial\phi}{\partial t}$, of the same four cases. To get the derivative of the phase for the numerical simulation, we fit a third-order polynomial to the set points and calculate the analytical derivative of the polynomial. For the experimental data, we use the analytical derivative of the polynomial found in Fig. 5.3. The derivative of the analytical approximation and the *Gedanken* experiment is calculated by the derivative of Eq. 6.11 and Eq. 6.13 respectively. We also plot in the inset the 5% deviation from the T^3 phase accumulation, this time by plotting the derivative of the modified *Gedanken* experiment phase accumulation.

$$\Delta\phi(2T) = \left(\frac{mg^2}{24\hbar}\right)^{\frac{3+\alpha}{3}} (2T)^{3+\alpha} \rightarrow \frac{\partial\phi}{\partial(2T)} = (3+\alpha)\left(\frac{mg^2}{24\hbar}\right)^{\frac{3+\alpha}{3}} (2T)^{2+\alpha}, \quad (6.25)$$

where the power of the coefficient is corrected to maintain the correct units. Fig. 5.4b shows the residuals between the experimental data and the numerical simulation. To estimate the statistical noise of the phase, we use a method of error propagation from the standard deviation (STD) of the population data to the STD of the phase, as explained in the next section.

6.4.3 Error analysis

We wish to find the phase uncertainty due to the uncertainty of a cosine signal $S(\phi) = a\cos(\phi)$, where the amplitude a and the phase ϕ have an uncertainty δa and $\delta\phi$, respectively. The uncertainty of the signal due to the phase and amplitude uncertainties is given by

$$\delta S^2 = \delta a^2 \cos^2 \phi + a^2 \sin^2 \phi \delta\phi^2. \tag{6.26}$$

This is a familiar relation, but it is important to remember that the trigonometric functions on the right-hand side should be averaged over the uncertainty $\delta\phi$ of the phase (otherwise this equation is not correct and gives wrong values, especially around the extremum points of the signal, where the derivative approaches zero). Assuming that ϕ is a Gaussian distributed variable with a STD $\delta\phi$, the expectation values of the trigonometric functions are

$$\left\langle \sin^2 \phi \right\rangle = \frac{1}{2}[1 - \langle \cos(2\phi) \rangle], \quad \left\langle \cos^2 \phi \right\rangle = \frac{1}{2}[1 + \langle \cos(2\phi) \rangle]. \tag{6.27}$$

where

$$\langle \cos(2\phi) \rangle_{\phi=\phi_0} = \frac{1}{\sqrt{2\pi}\delta\phi} \int_{-\infty}^{\infty} d\phi e^{-(\phi-\phi_0)^2/2\delta\phi^2} \cos(2\phi) = \cos\left(2\phi_0\right) e^{-2\delta\phi^2} \tag{6.28}$$

We obtain

$$\delta S^2 = \frac{1}{2}\left[1 + \cos(2\phi) e^{-2\delta\phi^2}\right] \delta a^2 + \frac{1}{2} a^2 \left[1 - \cos(2\phi) e^{-2\delta\phi^2}\right] \delta\phi^2. \tag{6.29}$$

To extract the STD of the phase, we need to know the STD of the signal (δS^2), the amplitude and phase of the signal (a and ϕ), which we get from the fit to the data, and the STD of the amplitude (δa). Finding both δa and $\delta\phi$ from δS^2 of a single point seems to be impossible because, on the right-hand side, we have two variables. So we must either assume a given value of δa and then find $\delta\phi$ from δS^2 or assume some relation of δa and $\delta\phi$ along the different measurement points that may enable the determination of both uncertainties from the signal. In our case, we assume that the amplitude uncertainty is negligible compared to the phase uncertainty, so we can find the phase uncertainty from the signal uncertainty. This assumption holds well for $2T > 1ms$, where the phase noise is the dominant source of noise in the signal, and is approximately proportional to the phase itself. While for $2T < 1\,\mathrm{ms}$ this assumption is less accurate, the STD of the signal is very small in this range, anyway. As the number of iterations per point is 2-4, resulting in large fluctuations of the STD, we fit the STD to a polynomial of order 3, and use the result of the fit as the STD of the phase in Fig. 5.4b. The results of the error analysis are shown in Fig. 6.3.

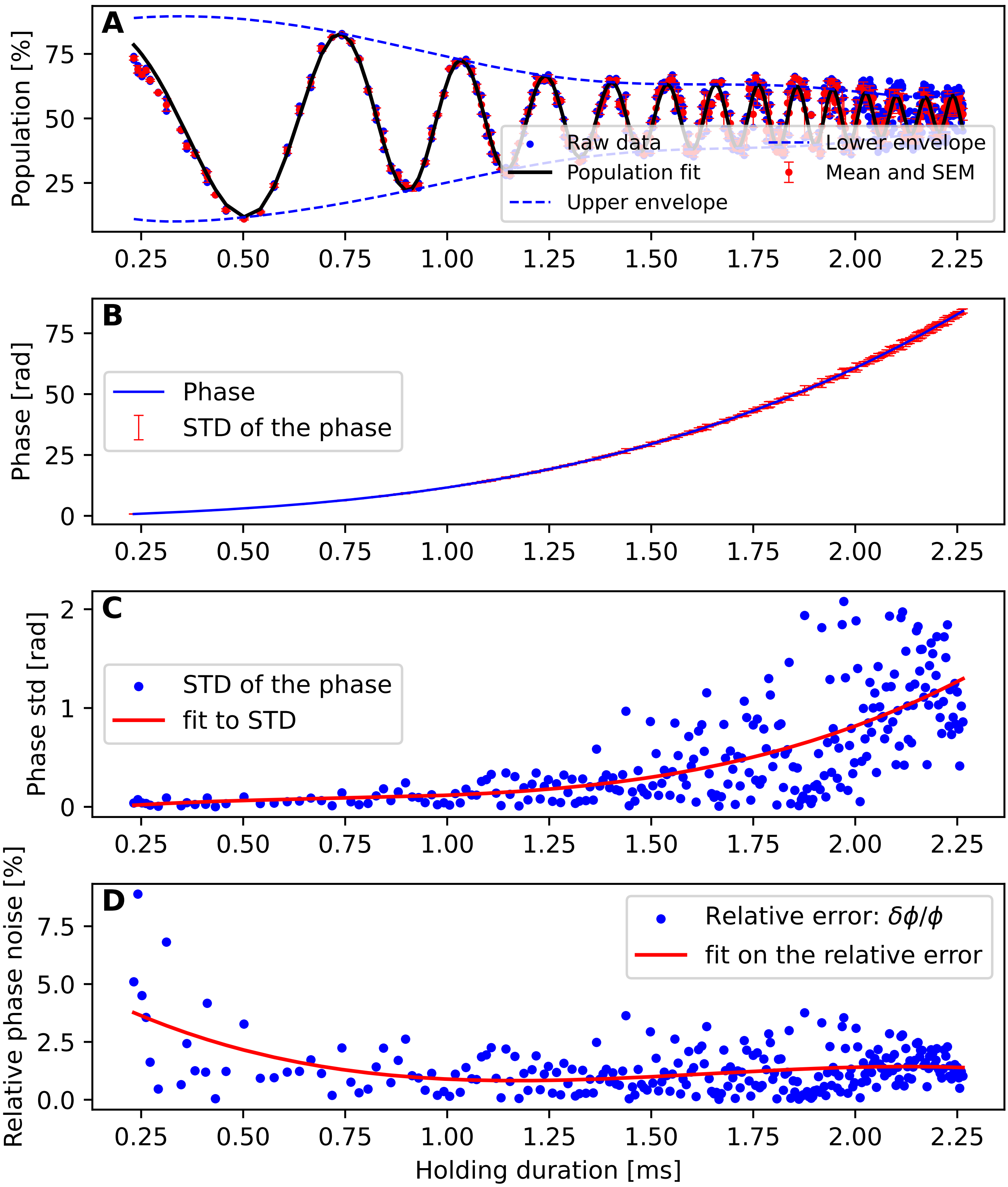

Figure 6.3: Summary of the error analysis: (a) The experimental data, including the raw data of the population vs. time, the fit to the envelope, and the fit to the data. (b) The phase as a function of the holding duration, with error bars indicating the STD of the phase. The STD is calculated using the method of error propagation explained in Sec. 6.4.3. (c) The STD of the phase, and fit to a third order polynomial. The result of the fit is used as the STD of the phase in Fig. 5.4b (d) The relative error of the phase, calculated as the ratio of the STD of the phase to the phase, which has an average value of 1.3%. Taken from [13].

6.5 Magnetic fields

Here we provide details on the magnetic fields in the experiment

6.5.1 Y-bias coils

The y-bias coils produce the bias magnetic field along the y-axis. We measured the magnetic field produced by the y-bias coils by measuring the resonance frequency of the transition from the $|2,2\rangle$ to $|2,1\rangle$ vs. the current in the coils. We fit the results to a model that includes the x and z magnetic bias fields and a stray magnetic field in the y-axis on top of the field produced by the y bias coils, such that $B_y = c \cdot I + B_{0y}$, and $|B| = \sqrt{((c \cdot I) + B_{0y})^2 + B_{0x}^2 + B_{0z}^2}$. The fit yields $c = 0.74 \pm 0.03\,\mathrm{G/A}$, and $B_{0y} = -1.4 \pm 1\,\mathrm{G}$.

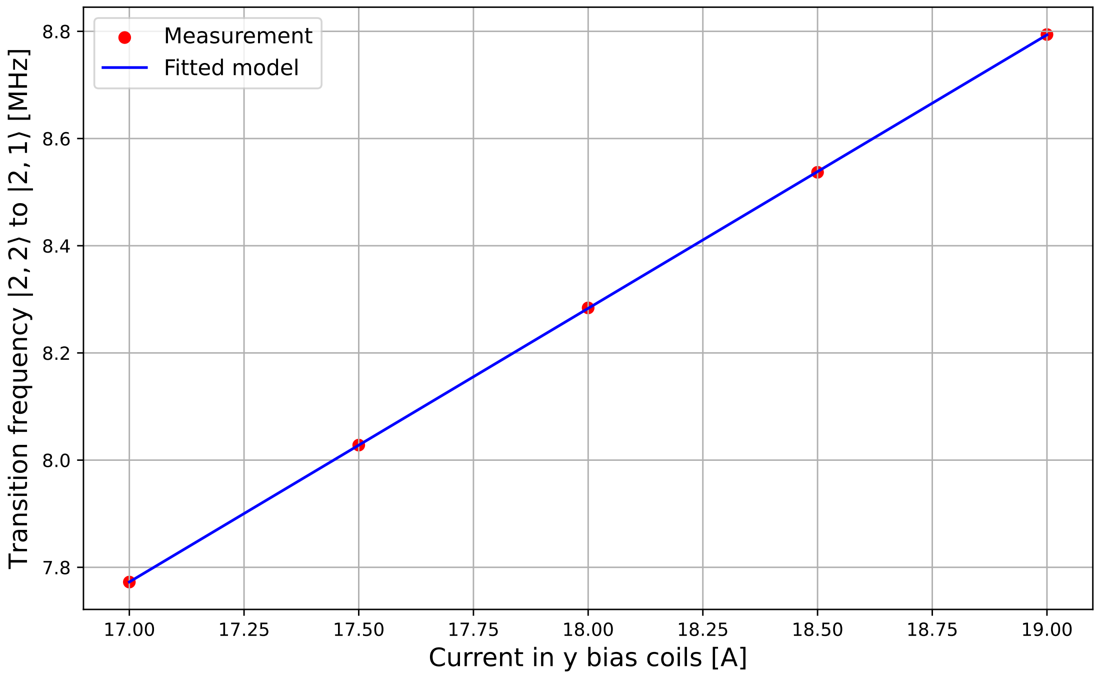

Figure 6.4: Measuring the magnetic field produced by the y bias coils: The resonance frequency of the transition from the $|2,2\rangle$ to $|2,1\rangle$, vs. the current in the coils. We fit the results to a model $B_y = c \cdot I + B_{0y}$, and $|B| = \sqrt{((c \cdot I) + B_{0y})^2 + B_{0x}^2 + B_{0z}^2}$. The fit gives $c = 0.74 \pm 0.03\,\mathrm{G/A}$, and $B_{0y} = -1.4 \pm 1\,\mathrm{G}$.

6.5.2 Ambient gradient in the chamber

Here we detail our findings on the ambient magnetic gradient in the chamber (taken from the supplementary material of [13]).

We found a small ambient magnetic gradient in the chamber even when the currents on the atom chip were zero. We measured this ambient magnetic gradient in two methods. The first method involves measuring the differential acceleration between the $|1\rangle$ and $|0\rangle$ states over a long time of flight of $20-34\,\mathrm{ms}$, following the $\pi/2$ pulse and observing the spatial splitting of the states. We fit the spatial splitting vs time and find $a_{ambient} = 0.211 \pm 0.005\,\mathrm{m/s^2}$. The data and the fit appear in Fig. 6.5. The second method is observing a T^3 phase accumulation when measuring the pure MW DD scheme (without magnetic gradients from chip wires) for a duration of $4\tau_{DD} = 4\,\mathrm{ms}$, which can, in the presence of the ambient gradient, create a “self emerging” T^3 full-loop SGI. In the original T^3 SGI scheme of [114], the loop is closed by inverting the orientation of the magnetic gradients. In this scheme, the magnetic gradients remain constant, and the π pulses invert the spin of the arms to create a closed interferometer. We calculate the prediction for the phase by plugging the durations $(\tau_{DD}, 2\tau_{DD}, \tau_{DD})$ and accelerations $a_1 = (a_{ambient}, 0, a_{ambient}) + g$, $a_2 = (0, a_{ambient}, 0) + g$ of the scheme into Eq. 6.4 which gives:

$$\delta\phi = \frac{m}{\hbar}\tau_{DD}^3\left(a_{ambient}^2 + 2ga_{ambient}\right) , \tag{6.30}$$

where $\tau_{DD} = (T_h + 2T_d)/2$. Using the prediction for the phase we extract $a_{ambient} = 0.221 \pm 0.005\,\mathrm{m/s^2}$, which corresponds to a magnetic gradient of $0.68 \pm 0.02\,\mathrm{G/cm}$. The data and the fit of this measurement appear in Fig. 6.6.

6.6 SG forces and magnetic field gradients

6.6.1 Magnetic potential energy of the atoms

Taken from the supplementary material of [13].

The potential in the SGI is the magnetic potential and gravity. The magnetic

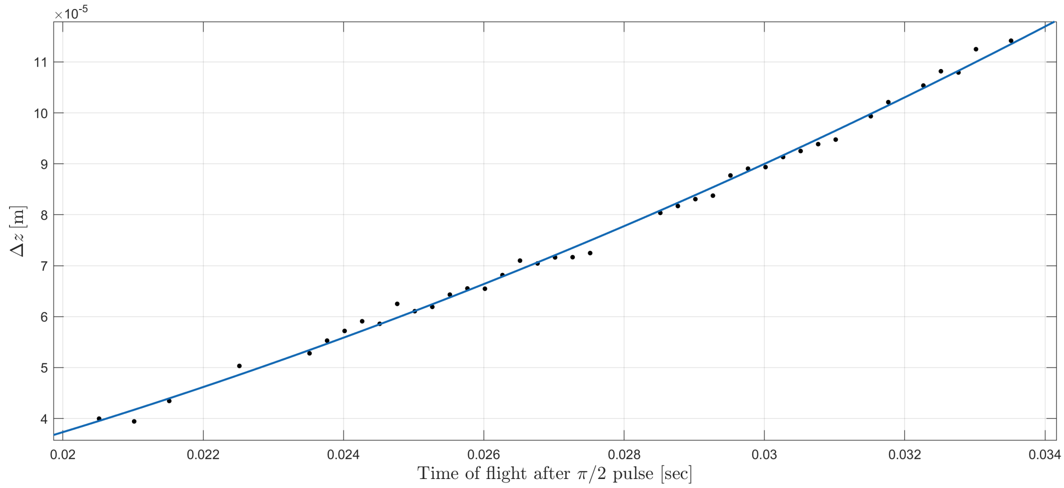

Figure 6.5: Splitting due to ambient magnetic gradient: Spatial SG splitting between the state $|1\rangle$ and $|0\rangle$ due to the ambient gradient, vs the time of flight after the $\pi/2$ pulse. Fitting the data to $0.5a_{ambient}TOF^2$ gives a value of $a_{ambient} = 0.211 \pm 0.005\,\mathrm{m/s^2}$. Taken from [13].

potential is given by

$$V_B(\mathbf{r}, t) = -\mu \cdot B(\mathbf{r}, t).$$

Under the adiabatic approximation, we can assume that the atomic spin projection on the quantization axis, defined by the direction of the magnetic field, is conserved, and including the second-order Zeeman splitting, we get

$$V_B(\mathbf{r}, t) = m_F g_F \mu_B |B(\mathbf{r}, t)| + \alpha_{\mathrm{F,m_F}} |B(\mathbf{r}, t)|^2 \tag{6.31}$$

where $g_F \mu_B / h = 0.70\,[\mathrm{MHz/G}]$ and $\alpha_{\mathrm{F,m_F}}$ is a coefficient that depends on F and m_F, given in table 6.1. Using Eq. 6.31, the values in table 6.1 and the measured transition frequency between $|F = 2, m_F = 2\rangle$ and $|F = 2, m_F = 1\rangle$ of 8.799 MHz we can calculate the magnitude of the bias field $|B| = 12.62\,\mathrm{G}$. To calculate a_{SOZ}, we find the magnetic gradient required to hold the $|F = 2, m_F = 1\rangle$ state against gravity, and use it to get the value of $a_{SOZ} = 0.10\,\mathrm{m/s^2}$.

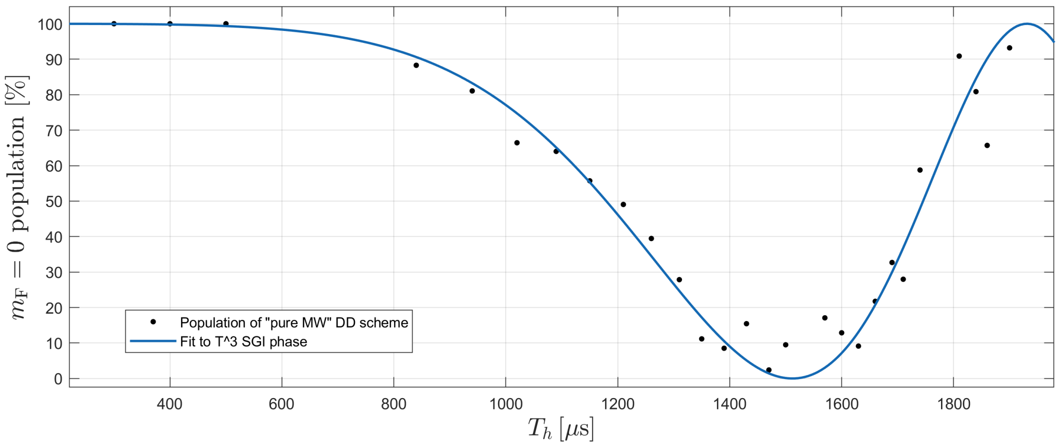

Figure 6.6: T^3 population oscillations due to ambient magnetic gradient: We observe T^3 population oscillations in a pure MW DD scheme, indicating the existence of a magnetic gradient. By fitting the data to $P(\tau_{DD}) = 50 + 50\cos\left[\frac{m}{\hbar}\tau_{DD}^3\left(a_{ambient}^2 + 2ga_{ambient}\right)\right]$, we can estimate the acceleration due to the ambient gradient, and get $a_{ambient} = 0.221 \pm 0.005\,\mathrm{m/s^2}$. Taken from [13].

F \ m_F	0	±1	±2
1	-287.6	-215.7	—
2	287.6	215.7	0

Table 6.1: Values of $\alpha_{\mathrm{F,m_F}}/h$ in units of Hz/G^2, for calculating the second order Zeeman energy in Eq. 6.31.

6.6.2 Magnetic field from a three-wire configuration

The magnetic gradients are produced by a current in the atom chip wires. To suppress phase noise originating from the magnetic field of these wires, we generate a strong magnetic gradient while minimizing the chip's magnetic field by forming a quadrupole field and positioning the atoms close to its zero-field center [45]. Three parallel current-carrying wires form the quadrupole field. Let us derive the field produced by currents through three infinitely-long parallel wires, which is useful for estimating the actual magnetic gradient forces in the experiment. The three wires are oriented along the x-axis, located at $y = -d, 0, d$ (for our chip $d = 100\,\mu$m, see Fig. 6.7). The currents in the outer wires are directed along $-x$ while the central wire current is along $+x$, and the magnitudes of the currents are the same in all three wires. Because the two external wires cancel each other's field in the z direction, the field directly below the central wire ($x = 0$) points in the y direction. An additional strong magnetic bias field B_y^0 is applied. The magnetic field under the center of the chip is

$$\boldsymbol{B}(0,0,z) = B_y^0 \hat{y} + \frac{\mu_0 I}{2\pi}\left[\frac{1}{z} - \frac{2z}{z^2+d^2}\right]\hat{y} \tag{6.32}$$

The gradient of the field's magnitude is directed along the z-axis and is given by

$$\frac{\partial |B(0,0,z)|}{\partial z} = \frac{\mu_0 I}{2\pi}\left[\frac{1}{z^2} + 2\frac{d^2 - z^2}{(d^2+z^2)^2}\right] \mathrm{sign}(B_y(z)\hat{z} \tag{6.33}$$

This expression assumes that the atoms are exactly below the chip center, meaning that the gradient and, thus, the force on the atoms is exerted only in the z direction. The gradient calculated at $z = d$ gives the same result as the single wire configuration because the second term in the brackets zeros out when $z = d$, leaving only the contribution due to the central wire. The direction of the force may be reversed experimentally by reversing the direction of the currents. Eq. 6.32 is not exact as the wires have finite length and finite width; When necessary, the fields generated by the chip wires are numerically calculated using the chip wire parameters. The magnetic field produced by the SG wires on the atom chip, as calculated by such a simulation, is shown in Fig. 6.7.

6.6.3 Magnetic gradient pulses

Taken from the supplementary material of [13].

The pulses of the magnetic gradient are formed by running a current through three parallel wires, with alternating current orientation, forming a magnetic quadrupole capable of producing high magnetic gradients with low magnetic fields. The wires are 2 μm thick, 40 μm wide, and are positioned 100 μm apart (center to center), creating a quadrupole 97 μm below the surface of the chip (see Fig. 3.11). The currents are produced by a homemade current source, with high stability and fast response, controlled by an analog signal input. The current source has a maximum slew rate of 30 mA/μs, a maximum current of 1 A and stability of 100 ppm. We control the current source by an arbitrary waveform generator, which allows us to

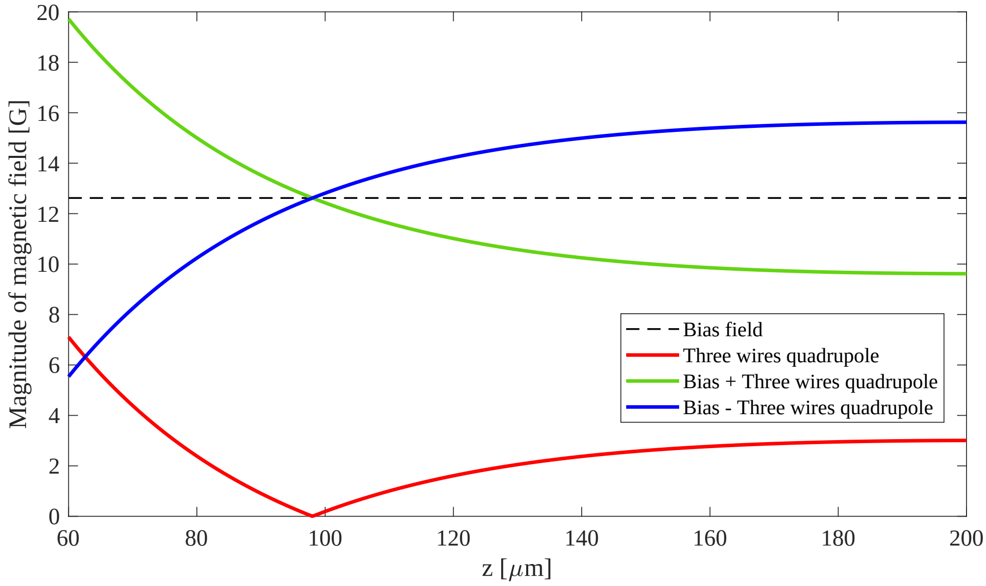

Figure 6.7: The magnetic field produced by the SG wires on the atom chip: The field is calculated numerically using the chip wire parameters, by dividing the wires into a grid of several smaller wires and calculating the field using the Biot–Savart law[1]. The bias field is set to $B_{0y} = 12.6\,[\mathrm{G}]$, $B_{0x} = 0.7\,[\mathrm{G}]$, and the current in the SG wires to 500 mA. The three SG wires create a quadrupole field, with a zero field point at a distance $z_{\mathrm{quad}} = 98\,\mu\mathrm{m}$ from the center of the chip wire (or $97\,\mu\mathrm{m}$ from the chip surface). The sum of the SG wires field and the bias field creates a curved field with a negative/positive curvature, depending on the sign of the current in the SG wires. In our case we aim to apply a force towards the chip on atoms in low-field seeking states. Hence, we use the configuration with the positive curvature depicted in the blue line.

[1]This is done using a Matlab program, written by Yonathan Japha from our group.

create smooth and accurate pulses. To obtain a smooth pulse, we demand that the time derivative $\partial I/\partial t$ is continuous and vanishes at the beginning and end of the pulse. We choose to use a cosine pulse shape, as it fulfills the conditions of a smooth pulse and is analytically solvable when calculating trajectories and phases. The equation describing the current for a pulse starting at t_0, rise and fall times of τ, separated by a duration w of constant current A is given by

$$\mathbf{I}(\mathbf{t}) : \begin{cases} 0 & \text{for } t < t_0 \\ \frac{I_{\max}}{2}\left(1-\cos\left(\frac{\pi(t-t_0)}{\tau}\right)\right) & \text{for } t_0 < t \leq t_0+\tau \\ I_{\max} & \text{for } t_0+\tau < t \leq t_0+\tau+w \\ \frac{I_{\max}}{2}\left(1-\cos\left(\frac{\pi(t-t_0-w)}{\tau}\right)\right) & \text{for } t_0+\tau+w < t < t_0+2\tau+w \\ 0 & \text{for } t \geq t_0+2\tau+w \end{cases} \tag{6.34}$$

The area under such a pulse is $I_{\max}(\tau + w)$. The scheme has two short kick pulses, and one longer holding pulse. The kick pulses have a rise and fall time of $\tau_{\text{kick}} = 40\,\mu\text{s}$ each, with $w = 0$ and $I_{\max} = I_{\text{kick}}$, so that the area of the pulse is $I_{\text{kick}} \cdot \tau_{\text{kick}}$. The longer holding pulse has a rise and fall time of $\tau_{\text{hold}} = 12\,\mu\text{s}$, and a duration $w = T_h - \tau_{\text{hold}}$ of constant current I_{hold} so that the total area of the pulse is $I_{\text{hold}} \cdot T_h$.

The acceleration during the holding pulse is tuned to hold the $|1\rangle$ state against gravity. Measurement of the acceleration of the atoms shows that the required current is $I_{hold} = 23.07 \pm 1.49\,\text{mA}$. To maintain the symmetry of the scheme, the momentum given by the two kick pulses should be equal to the momentum given by the holding pulse, which gives the conditions

$$a_{kick} = \frac{g}{2\tau_{\text{kick}}} T_h \ , \tag{6.35}$$

$$a_{\text{hold}} = g \, . \tag{6.36}$$

To improve the response of the current source and reduce the effect of the ambient gradient in the chamber, we set the current between the pulses to a finite value, which we call the idle current, and set its value to $I_{\text{idle}} = 0.47\,\text{mA}$. The idle is on during the entire interferometer sequence. By including the idle current, we get the following requirements for the currents

$$(I_{\text{kick}} - I_{\text{idle}})\, 2\tau_{\text{kick}} = (I_{\text{hold}} - I_{\text{idle}}) T_h \tag{6.37}$$

$$I_{\text{kick}} = \frac{I_{\text{hold}} - I_{\text{idle}}}{2\tau_{\text{kick}}} T_h + I_{\text{idle}} \tag{6.38}$$

6.6.4 Calibration of the holding current

To calibrate the holding current I_{hold}, we measured the acceleration of the atoms as a function of the current in the SG wires. For each value of the current, we measured the position of the atoms along the z-axis as a function of time while being held, and fitted each data set to a parabola. The holding current is adjusted so that the total acceleration is equal to zero, namely, the acceleration due to the holding pulse cancels the acceleration due to gravity and the residual magnetic gradient in the chamber. The measurement is shown in Fig. 6.8, and yields a value of $I_{\text{hold}} = 23 \pm 1.5\text{mA}$.

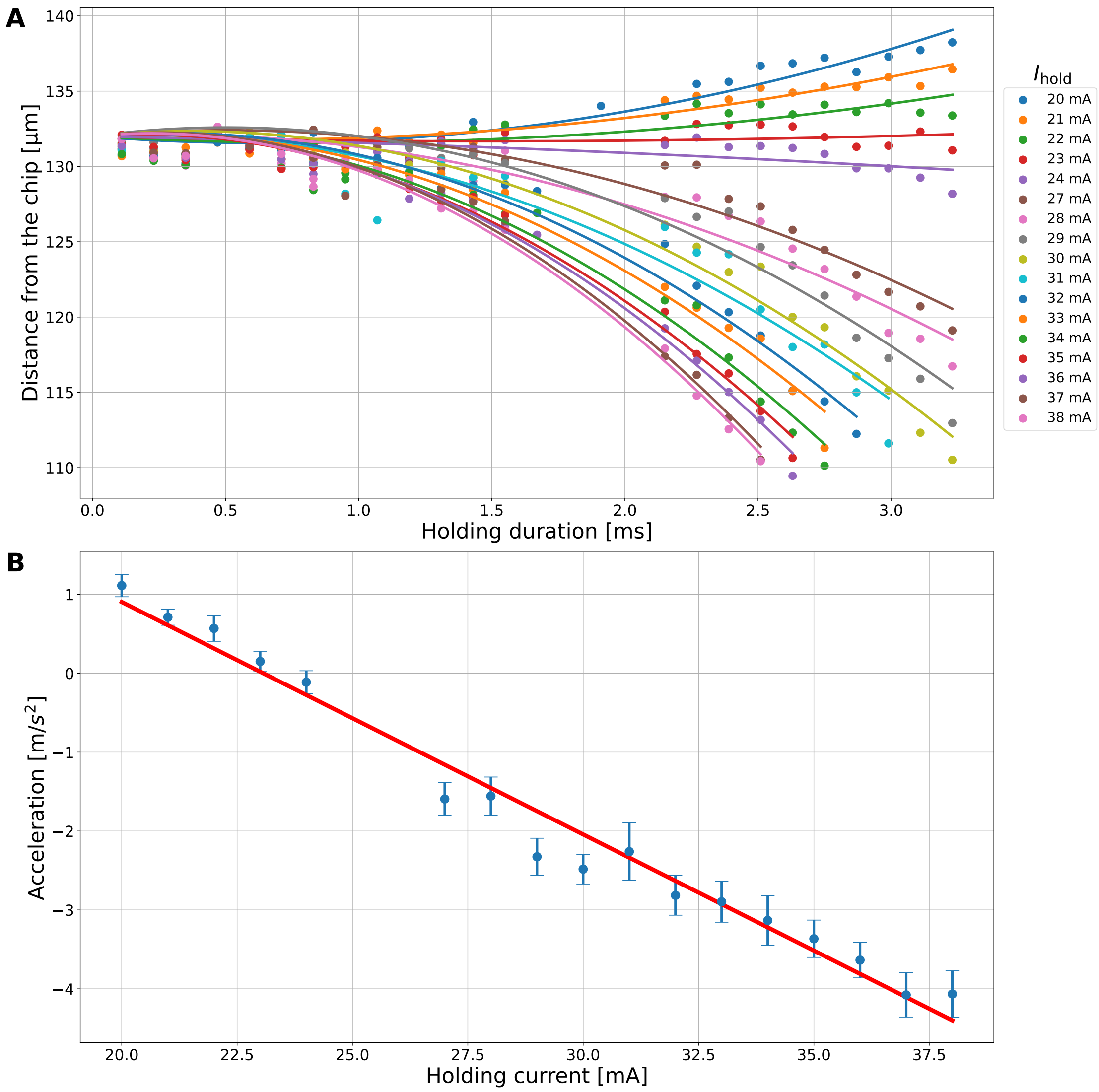

Figure 6.8: Calibration of the holding current: (a) Position along the z-axis vs. time for different holding current values. Each data set is fitted with a parabola of the form $z(t) = z_0 + v_0 t + \frac{1}{2}at^2$, where we set $z_0 = 132$ for all the data sets (note that the chip's position in this measurement was not calibrated to $z = 0$. As we are interested in the shape of trajectories, the constant shift in z is irrelevant). (b) The acceleration of the atoms vs. the holding current. A linear fit predicts a zero acceleration for $I_{\text{hold}} = 23 \pm 1.5\text{mA}$.

6.7 Trap characterization

We characterized the magnetic trap in the experiment. Here we provide details on the trap bottom, trap frequency, and initial position stability.

A measurement of the trap frequency is shown in Fig. 6.10, and the trap bottom is shown in Fig. 6.11. The measurements yield a trap frequency of $1009 \pm 4\,\mathrm{Hz}$, and a trap bottom of $0.425 \pm 0.005\,\mathrm{MHz}$.

6.7.1 Initial position stability

Since the magnetic potential is curved, the magnetic gradient is not constant and varies with position. Consequently, the phase and visibility of the interferometer are sensitive to changes in the atoms' initial position, potentially causing both shot-to-shot instability and long-term drifts in the measurement results.

Our experimental procedure includes evaporative cooling in a magnetic trap generated by a macroscopic Z-shaped wire, which in previous SGI experiments served as the starting point from which the atoms were released. The initial position fluctuations of the atoms in the Z-wire magnetic trap are estimated to be $1-2\,\mu$m. A feasibility study using our numerical simulation showed that with initial position fluctuations of $2\,\mu$m, the signal will be lost after 2-3 full oscillations due to the phase noise, which assured the necessity of a more stable trap.

The z-wire trap has two other significant flaws. First, it introduced drifts (low-frequency noise) in the initial position of the atoms relative to the atom chip as the z-wire leads expand or contract with temperature fluctuations. Second, the high current required for the z-wire (20-90 A) resulted in a slow shut-off of the trap, with a fall time of $400\,\mu s$, and a residual current of 100 mA for 2 ms after shutting off the current. This residual current introduced a transient magnetic gradient that limited the MW and RF Ramsey sequence's coherence time, significantly reducing the SGI's visibility.

On the other hand, the atom chip trap requires less than 1 A, and operates with a battery-powered, high-stability current source that can shut off the current in less than $10\,\mu s$. Moreover, it does not suffer from long-term drifts as it is part of the atom chip itself. Indeed, after switching to the atom chip trap, we observed a significant improvement in the Ramsey sequence's coherence time.

To estimate the stability of the trap position, we measured the shot-to-shot fluctuations of the final position of the trap, resulting in a STD of $0.1\,\mu$m (see Fig. 6.12).

The high positional stability is a key advantage of the atom chip trap over the z-wire trap, enabling improved visibility, enhanced phase stability, and greater spatial splitting compared to previous experiments [15, 114]. The atom chip trap also reduces low-frequency noise (drifts) in the interferometer, enhancing the long-term stability of the phase, allowing for long sessions of data taking (3-6 hours of data for one graph), and high repeatability of the experiment.

6.8 Wave-packet size

Taken from the supplementary material of [13].

Direct experimental measurement of the wave-packet size is a hard task. To begin with, our optical resolution is only $3\,\mu$m. Second, imaging near the chip distorts the image due to diffraction from the chip. Diffraction also originates from the high optical density of the atom cloud. Finally, the magnetic potential of the DKC, as well as the magnetic fields during the SG kicks, are curved as they emanate from the nearby chip wires. These curvatures create lensing (focusing) effects, which result in fast changes in the wave-packet size over time. Given these restrictions, when imaging the wave-packet width we observe a width of $3-4\,\mu$m on the CCD, which indicates that the actual size is most probably below our optical resolution.

A better estimation of wave-packet size is derived using our accurate numerical simulation (Fig. 6.13). The simulation shows that halfway through the interferometer, the wave-packet size is in the range of $1-1.3\,\mu$m. The maximum splitting achieved is thus 6.5 times the wave-packet width.

6.9 The trajectories in the QGI

We imaged the trajectories of the atoms during the interferometer sequence of the QGI, which proved to be a daunting task due to the reasons mentioned above in Sec. 6.8. In addition to the reasons mentioned, which limit the estimation of the wave-packet size, determining the absolute position of the atoms is also affected by "chromatic aberrations," namely a dependence of the measured position on the detuning of the imaging beam. Together with the fast-changing magnetic gradients which are part of the QGI sequence, the imaging accuracy is heavily restricted. Nonetheless, we succeeded in imaging the trajectories of the atoms during the QGI as shown in Fig. 6.14. The measurement also demonstrates the effect of the detuning, as for each detuning, we get not only a shift of the imaged trajectory but also a different trajectory shape. In this imaging process, we observe a maximal separation of the two arms of 6.8 μm, which stands in reasonable agreement with the numerical simulation that predicts a maximal separation of 7.5 μm. The prediction for the trajectories in the numerical simulation is shown in Fig. 6.15.

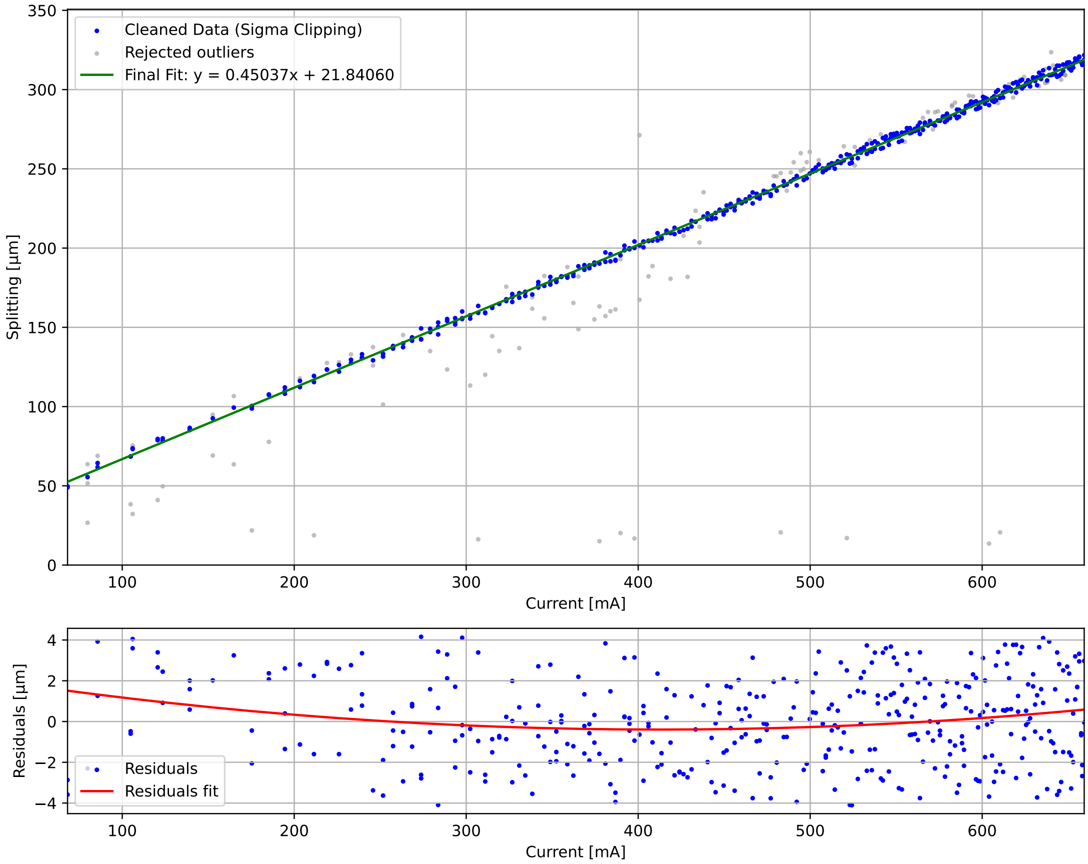

Figure 6.9: Linearity of the kick pulse: Measuring the momentum splitting of the atoms after applying a kick pulse of different amplitudes. The splitting along the z-axis is measured by imaging the atoms after a time of flight of 19.536 ms and fitting each wave packet to a Gaussian. As the fitting process does not always find the two wave packets, we clean the data by removing outliers, using the "Sigma clipping" [122] method with a threshold of 2σ (fitting a linear function, calculating σ as the STD of the points from the fitted line, and rejecting points more than 2σ away from the fit, than repeating the process iteratively until it converges). The blue points represent the data points after removing the outliers, and the gray points represent the rejected data points; most of the rejected points are indeed unsuccessful fits, while others are valid data points with a residual larger than 2σ from the linear fit.

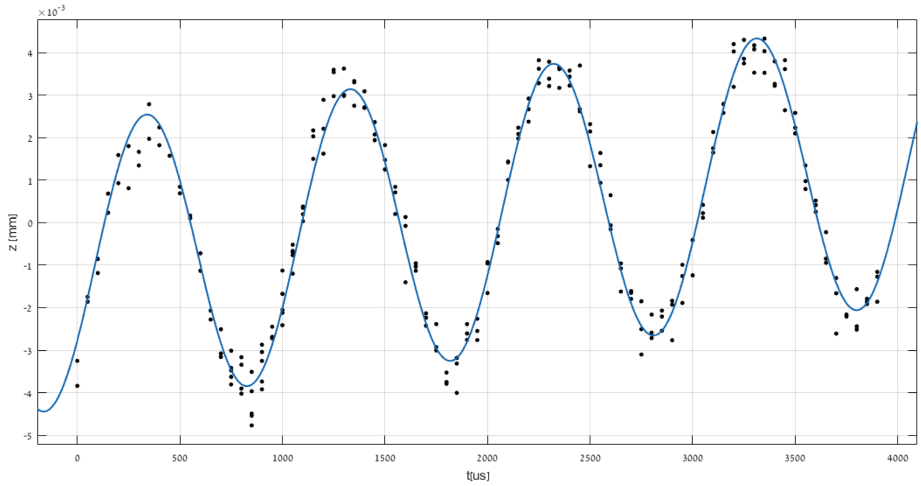

Figure 6.10: Measurement of the trap frequency for the final magnetic trap on the atom chip: We kick the atoms and observe the oscillations in the trap. The position of the atoms along the z-axis vs time shows harmonic oscillations with a frequency of 1009 ± 4 Hz.

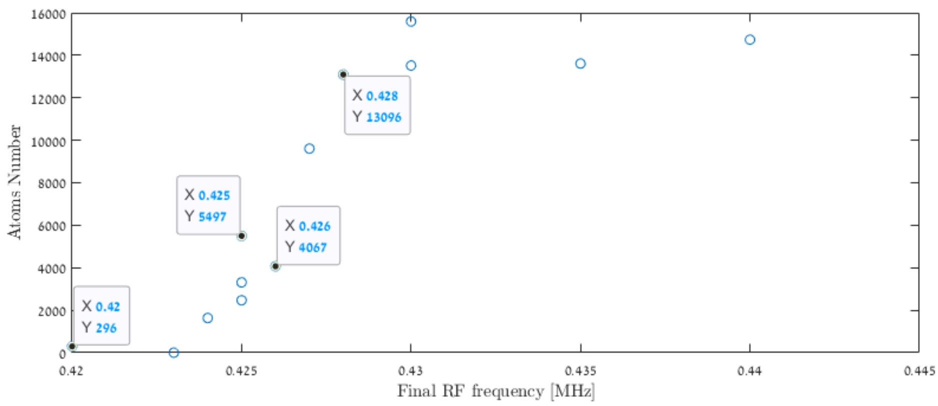

Figure 6.11: Measurement of the trap bottom for the final magnetic trap on the atom chip: The number of atoms as a function of the final RF frequency of the evaporation stage shows a sharp decrease around 0.425 MHz, indicating that the trap bottom is 0.425 ± 0.005 MHz. The atoms were imaged 20 ms after release from the trap.

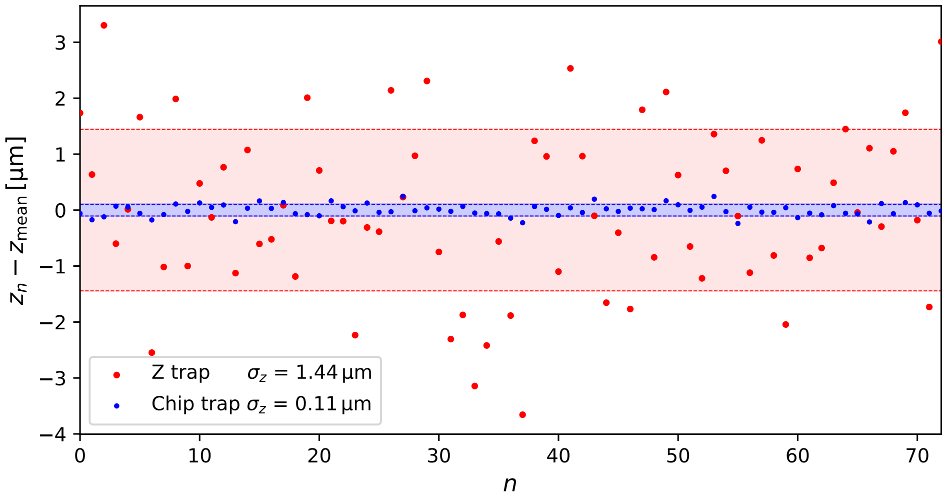

Figure 6.12: Initial position stability: Plotting the shot-to-shot fluctuations of the position of the atoms along the z-axis reveals a STD of 0.1 μm in the atom chip trap, compared to 1.4 μm in the z-wire trap. The high stability of the atom chip trap significantly enhances the visibility and phase stability of the SGI. Note that while the optical resolution is 3 μm, the position of the center of the cloud can be resolved at a much higher precision. The position is calculated from the data of the whole cloud by a 2D-Gaussian fit, which results in precision much better than the optical resolution, which only defines the ability to resolve two nearby spots. Taken from [13].

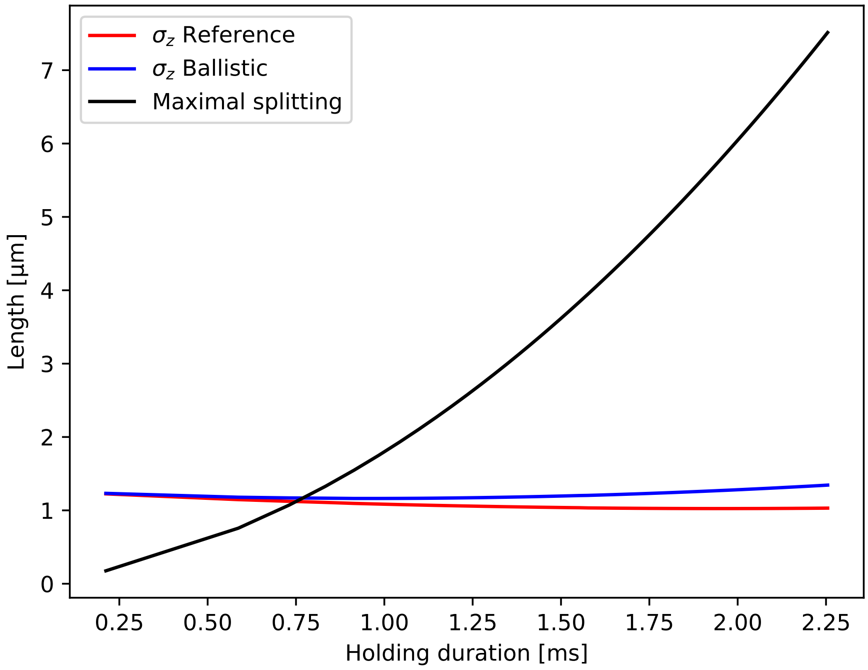

Figure 6.13: Wave-packet size during the QGI: Numerical calculation of the wave packet size and the maximal splitting for different interferometer durations. The wave-packet width is defined by the Gaussian width of the wave packet along the z-axis. At the largest holding duration, the maximal splitting is $7.5\,\mu$m, and the wave-packet widths are $1\,\mu$m and $1.3\,\mu$m, for the reference and ballistic wave packets, respectively. Taken from [13].

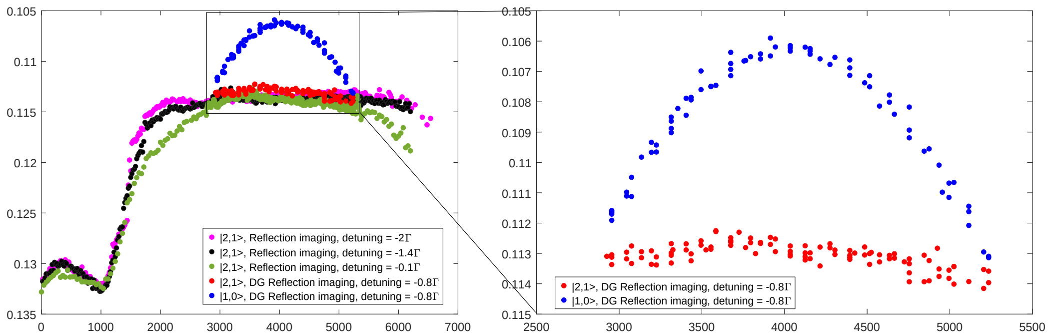

Figure 6.14: Measured trajectories in the QGI: position of the atoms vs time from the trap release. The $|2, 1\rangle$ state was imaged in two different imaging setups, one using absorption reflection imaging, with three different detunings; the second used dark ground reflection imaging, in which the imaging beam is blocked after leaving the vacuum chamber, and only the light scattered by the atoms reaches the CCD. The inset shows the trajectories of the two states in the interferometer, with a maximal separation of $6.8\,\mu$m. The imaging accuracy is heavily restricted due to reasons explained in Sec. 6.8 and 6.9. To image the position of the $|1, 0\rangle$ state, which is a dark state for our imaging beam, we first apply a short $30\,\mu$s pulse of repumper laser to pump the atoms into a bright state.

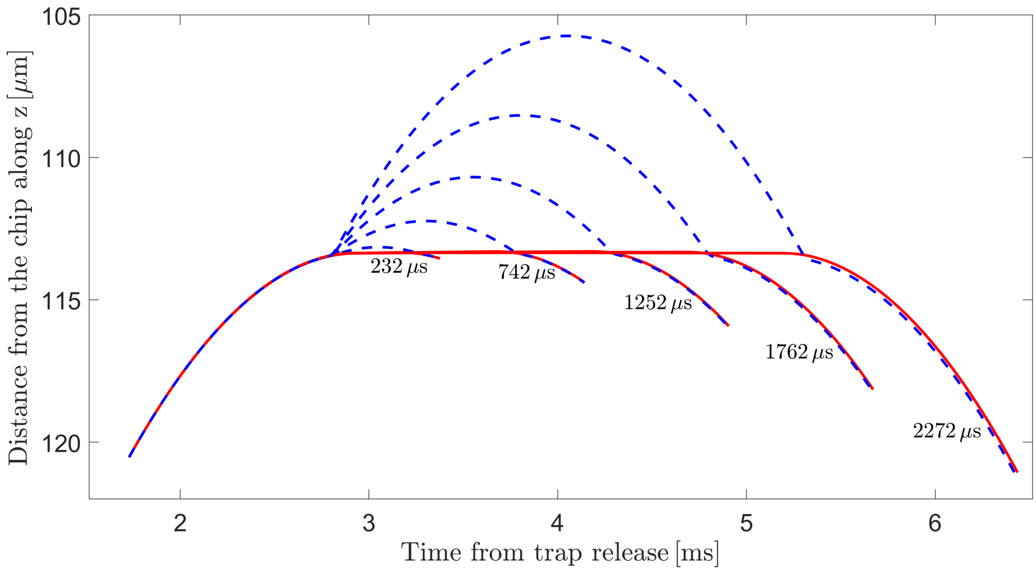

Figure 6.15: Simulated trajectories of the wave packets for different holding durations: The trajectories of the two arms of the interferometer, calculated by the numerical simulation for holding durations $T_h = 232, 742, 1252, 1762, 2272\,\mu$s. Dashed blue lines represent the ballistic trajectory, and solid red lines the static wave packet. At the end of the interferometer, a small spatial splitting can be seen, on the order of $0.1\,\mu$m. For $T_h = 2272\,\mu$s, the spatial splitting between the two arms halfway through the interferometer reaches $7.5\,\mu$m. The trajectories are plotted until the time in which the final (second) $\pi/2$ is applied. Taken from [13].

Appendices

Appendix A

Apparatus details

In this appendix we add two additional figures to Sec. 3.5. In Fig. A.1 we show the atom chip holder with the copper structure that are used for producing the magnetic fields during the 3D-MOT (copper U) and magnetic trap (copper Z). In Fig. A.2 we show the heat management of the atom chip mount, including the heat sink and "super wire".

In Table A.1 we present the calibration of the current source used for the SG coils.

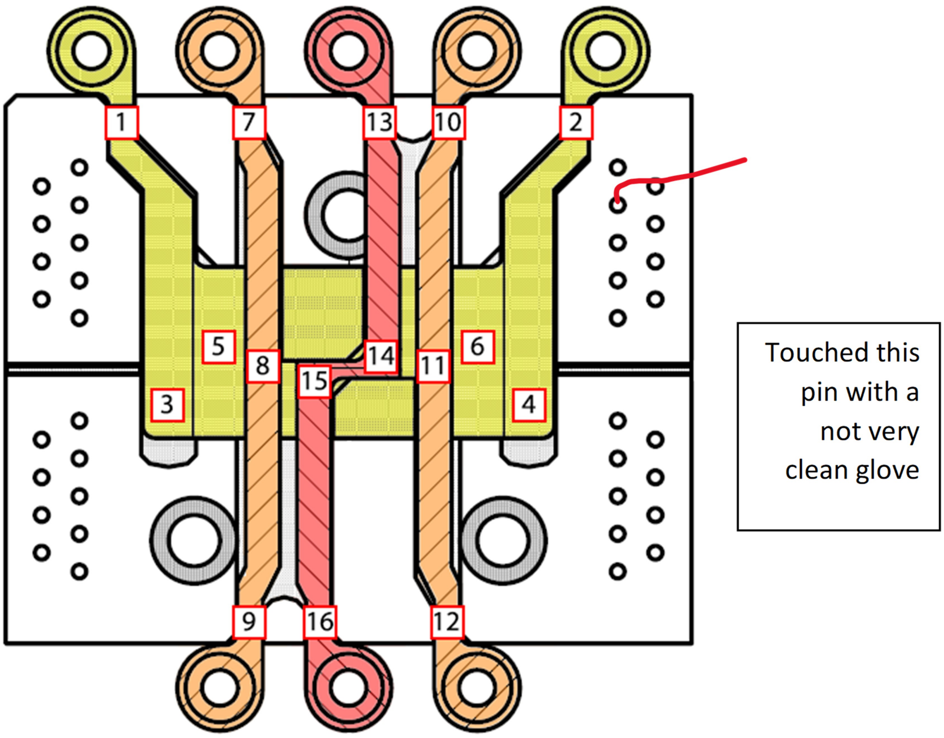

	Copper Z:		**Copper U:**
$\Delta Z_{13} = 279\mu m$	Legs:	$\Delta U_1 = 464\mu m$	Legs:
$\Delta Z_{16} = 306\mu m$		$\Delta U_2 = 386\mu m$	
$\Delta Z_{14} = 270\mu m$	Middle:	$\Delta U_3 = 540\mu m$	Top:
$\Delta Z_{15} = 289\mu m$		$\Delta U_4 = 453\mu m$	
		$\Delta U_5 = 1788\mu m$	Middle:
		$\Delta U_6 = 1719\mu m$	
			Copper Legs:
	Right:		**Left:**
$\Delta L_{10} = 238\mu m$	Legs:	$\Delta L_7 = 305\mu m$	Legs:
$\Delta L_{12} = 322\mu m$		$\Delta L_9 = 304\mu m$	
$\Delta L_{11} = 206\mu m$	Middle:	$\Delta L_8 = 226\mu m$	Middle:

Figure A.1: The MACOR block that holds the copper structure: The atom chip is glued on the MACOR with UHV-compatible epoxy. Careful measurements of the vertical distance between the copper and the surface of the MACOR were performed to determine the safe range of the thermal expansion of the mount. The copper structure is used for producing the magnetic fields during the 3D-MOT (copper U, in yellow) and magnetic trap (copper Z, in red).

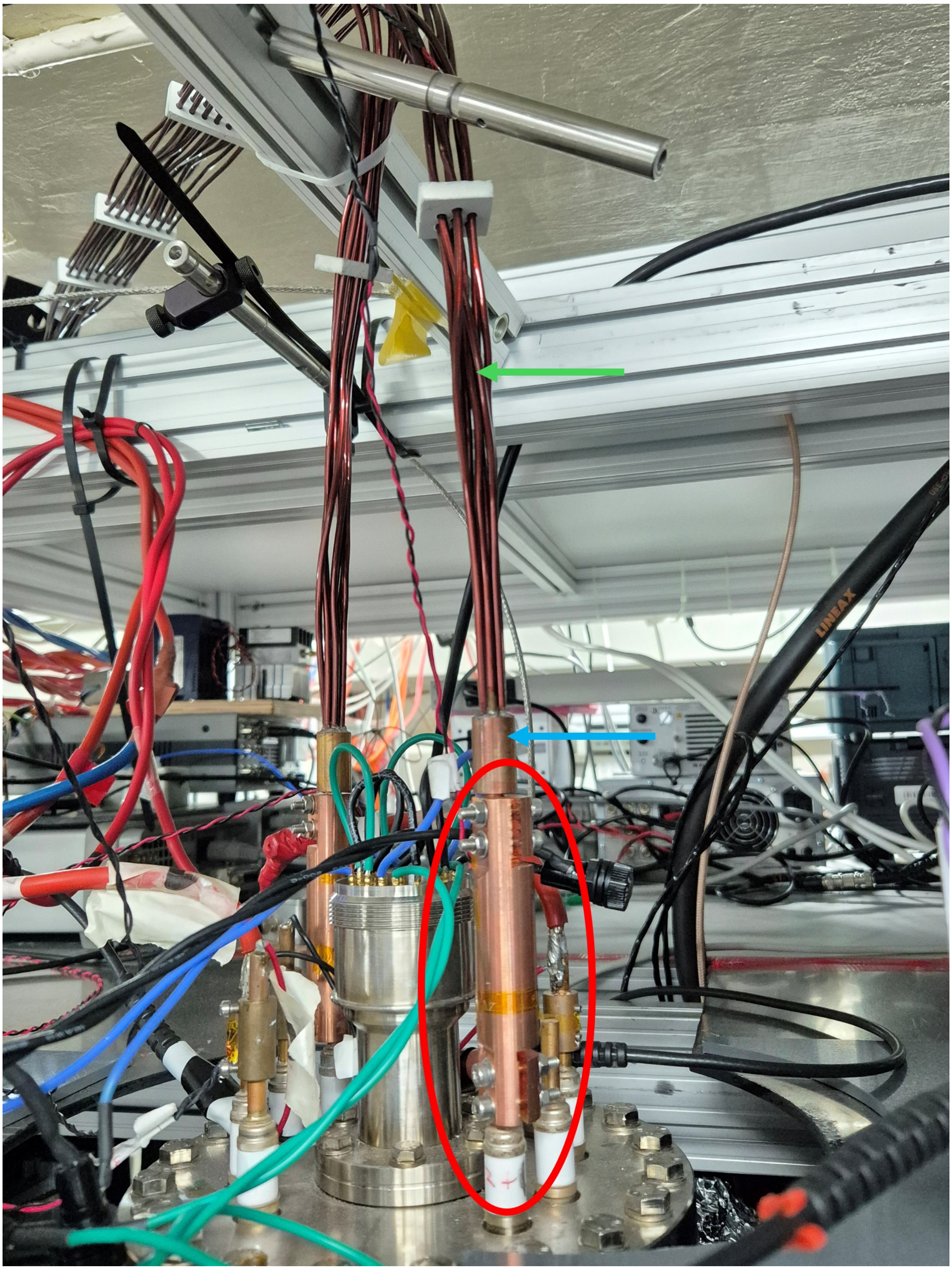

Figure A.2: Heat management for the atom chip mount: A copper heat sink (circled in red) attached to the feedthrough significantly increases the heat capacity and surface area for extracting heat from the vacuum side. The "super wire" (green arrow), made of seven independent Kapton-coated copper wires soldered together at each end (blue arrow), is used to connect the heat sink to the wires leading to the power supply. The super wire can hold a DC current of 90 Ampere with only a one-degree Celsius increase in temperature.

Calibration table for the Stern-Gerlach current source, all units are mA					
I_input	I_measured	Reading error	I_input	I_measured	Reading error
0.000	0.125	0.002	201.049	201.30	0.1
0.200	0.126	0.003	223.173	223.40	0.1
0.250	0.126	0.002	227.676	227.80	0.1
0.260	0.314	0.002	241.568	241.83	0.0
0.270	0.313	0.002	256.407	256.77	0.0
0.300	0.315	0.003	264.804	265.11	0.0
0.400	0.467	0.003	270.433	270.70	0.1
0.600	0.469	0.003	285.564	285.90	0.1
0.800	0.853	0.003	316.552	316.91	0.2
1.000	1.040	0.003	447.347	447.70	0.1
2.000	2.081	0.002	456.213	456.50	0.2
3.000	3.002	0.002	474.948	475.40	0.1
4.000	4.067	0.003	482.990	483.40	0.1
5.000	4.959	0.002	489.834	490.20	0.1
19.826	20.004	0.001	495.351	495.80	0.1
23.000	23.096	0.005	505.024	505.40	0.1
23.100	23.093	0.005	560.021	560.60	0.2
23.200	23.280	0.004	576.662	577.10	0.1
23.300	23.279	0.004	587.667	588.00	0.1
23.400	23.476	0.002	595.567	596.10	0.1
23.500	23.663	0.002	595.842	596.30	0.1
23.600	23.665	0.002	624.478	625.10	0.1
23.700	23.817	0.003	660.337	660.80	0.1
23.800	23.814	0.003	736.768	737.40	0.1
23.900	24.004	0.003	751.584	752.20	0.2
24.000	24.175	0.003	768.703	769.20	0.2
50.620	50.640	0.010	774.373	774.80	0.1
53.933	53.970	0.010	810.468	811.00	0.1
62.846	62.900	0.100	817.034	817.80	0.1
71.225	71.430	0.010	858.214	858.70	0.1
96.663	96.803	0.010	870.771	871.40	0.1
124.546	124.600	0.100	876.150	876.80	0.1

Table A.1: Current source calibration table: The current source used for the SG wires on the atom chip was measured using an ammeter (Keithley 2000 6.5 digit). All values are in mA. The current source is controlled by an analog signal from an arbitrary waveform generator (Agilent 33220A), which receives a digital waveform from the experimental control. To ensure correct calibration and estimate the precision of the source, we measure the output current against the input value from the experimental control. The 14-bit resolution of the digital to analog converter in the Agilent 33220A, with the conversion of input voltage to current in the current source ($\approx 1\,\mathrm{A}/10\,\mathrm{V}$) results in a resolution of 0.18 mA in the current, as can be seen in the table for the measurements in the range of 23-24 mA, where we scan the input every 0.1 mA, but the current moves discretely with jumps of $\approx 0.18\,\mathrm{mA}$.

Bibliography

[1] A. Einstein, "How I created the Theory of Relativity," Physics today **35**, 45–47 (1982).

[2] G. P. Thomson and A. Reid, "Diffraction of Cathode Rays by a Thin Film," Nature **119**, 890–890 (1927).

[3] C. Davisson and L. H. Germer, "Diffraction of Electrons by a Crystal of Nickel," Phys. Rev. **30**, 705–740 (1927).

[4] S. Abend, M. Gersemann, C. Schubert, D. Schlippert, E. M. Rasel, M. Zimmermann, M. A. Efremov, A. Roura, F. A. Narducci, and W. P. Schleich, "Atom interferometry and its applications," in "Foundations of Quantum Theory," (IOS Press, 2019), pp. 345–392.

[5] B. Barrett, A. Bertoldi, and P. Bouyer, "Inertial quantum sensors using light and matter," Phys. Scripta **91**, 053006 (2016).

[6] M. Keil, S. Machluf, Y. Margalit, Z. Zhou, O. Amit, O. Dobkowski, Y. Japha, S. Moukouri, D. Rohrlich, Z. Binstock, Y. Bar-Haim, M. Givon, D. Groswasser, Y. Meir, and R. Folman, "Stern-Gerlach interferometry with the atom chip," Molecular Beams in Physics and Chemistry: From Otto Stern's Pioneering Exploits to Present-Day Feats pp. 263–301 (2021).

[7] R. Folman, P. Krüger, J. Schmiedmayer, J. Denschlag, and C. Henkel, "Microscopic Atom Optics: from Wires to an Atom Chip," Adv. At. Mol. Opt. Phys. **48**, 263 – 356 (2002).

[8] J. Reichel, "Microchip traps and Bose–Einstein condensation," Appl. Phys. B **74**, 469–487 (2002).

[9] J. Fortágh and C. Zimmermann, "Magnetic microtraps for ultracold atoms," Rev. Mod. Phys. **79**, 235–289 (2007).

[10] J. Reichel and V. Vuletic, *Atom Chips* (Wiley-VCH, 2011).

[11] C. Marletto and V. Vedral, "On the Testability of the Equivalence Principle

as a Gauge Principle Detecting the Gravitational t3 Phase," Front. Phys. **8**, 176 (2020).

[12] R. Howl, R. Penrose, and I. Fuentes, "Exploring the unification of quantum theory and general relativity with a Bose–Einstein condensate," New J. Phys. **21**, 043047 (2019).

[13] O. Dobkowski, B. Trok, P. Skakunenko, Y. Japha, D. Groswasser, M. Efremov, C. Marletto, I. Fuentes, R. Penrose, V. Vedral, W. P. Schleich, and R. Folman, "Observation of the quantum equivalence principle for matter-waves," arXiv preprint arXiv:2502.14535 (2025).

[14] O. Amit, O. Dobkowski, Z. Zhou, Y. Margalit, Y. Japha, S. Moukouri, Y. Meir, B. Horovitz, and R. Folman, "Anomalous periodicity in superpositions of localized periodic patterns," New J. Phys. **24**, 073032 (2022).

[15] Y. Margalit, O. Dobkowski, Z. Zhou, O. Amit, Y. Japha, S. Moukouri, D. Rohrlich, A. Mazumdar, S. Bose, C. Henkel, and R. Folman, "Realization of a complete Stern-Gerlach interferometer: Toward a test of quantum gravity," Sci. Adv. **7**, eabg2879 (2021).

[16] W. D. Phillips and H. Metcalf, "Laser deceleration of an atomic beam," Phys. Rev. Lett. **48**, 596 (1982).

[17] Serious-Science, "Magneto-Optical Trap - David Pritchard," `https://youtu.be/znyKn5-_ymE?si=4bLjRAe5Q-EvC_0h&t=188` (2014).

[18] A. Ashkin and J. P. Gordon, "Stability of radiation-pressure particle traps: an optical Earnshaw theorem," Optics letters **8**, 511–513 (1983).

[19] D. E. Pritchard, E. L. Raab, V. Bagnato, C. E. Wieman, and R. N. Watts, "Light traps using spontaneous forces," Phys. Rev. Lett. **57**, 310 (1986).

[20] E. L. Raab, M. Prentiss, A. Cable, S. Chu, and D. E. Pritchard, "Trapping of neutral sodium atoms with radiation pressure," Phys. Rev. Lett. **59**, 2631 (1987).

[21] W. Phillips, "Historical foreword: Jean Dalibard, the magneto-optical

trap, and the ascent of physics with cold atomic gases," Comptes Rendus. Physique **24**, 5–13 (2023).

[22] M. H. Anderson, J. R. Ensher, M. R. Matthews, C. E. Wieman, and E. A. Cornell, "Observation of Bose-Einstein condensation in a dilute atomic vapor," Science **269**, 198–201 (1995).

[23] K. B. Davis, M.-O. Mewes, M. R. Andrews, N. J. van Druten, D. S. Durfee, D. Kurn, and W. Ketterle, "Bose-Einstein condensation in a gas of sodium atoms," Phys. Rev. Lett. **75**, 3969 (1995).

[24] J. B. Fixler, G. Foster, J. McGuirk, and M. Kasevich, "Atom interferometer measurement of the Newtonian constant of gravity," Science **315**, 74–77 (2007).

[25] R. H. Parker, C. Yu, W. Zhong, B. Estey, and H. Müller, "Measurement of the fine-structure constant as a test of the Standard Model," Science **360**, 191–195 (2018).

[26] M. Riedel, M. Kovacs, P. Zoller, J. Mlynek, and T. Calarco, "Europe's Quantum Flagship initiative," Quantum Sci. Technol. **4**, 020501 (2019).

[27] K. Wintersperger, F. Dommert, T. Ehmer, A. Hoursanov, J. Klepsch, W. Mauerer, G. Reuber, T. Strohm, M. Yin, and S. Luber, "Neutral atom quantum computing hardware: performance and end-user perspective," EPJ Quantum Technol. **10**, 32 (2023).

[28] H. Levine, A. Keesling, G. Semeghini, A. Omran, T. T. Wang, S. Ebadi, H. Bernien, M. Greiner, V. Vuletić, H. Pichler, and M. D. Lukin, "Parallel implementation of high-fidelity multiqubit gates with neutral atoms," Phys. Rev. Lett. **123**, 170503 (2019).

[29] W. A. Ertmer, S. T. Seidel, H. Ahlers, D. Becker, M. D. Lachmann, T. Wendrich, and E. M. Rasel, "Space-borne Bose–Einstein condensation for precision interferometry," Nature **562**, 391–395 (2018).

[30] E. R. Elliott, M. C. Krutzik, J. R. Williams, R. J. Thompson, and D. C.

Aveline, "NASA's Cold Atom Lab (CAL): system development and ground test status," npj Microgravity **4**, 16 (2018).

[31] D. W. Keith, C. R. Ekstrom, Q. A. Turchette, and D. E. Pritchard, "An interferometer for atoms," Phys. Rev. Lett. **66**, 2693–2696 (1991).

[32] O. Carnal and J. Mlynek, "Young's double-slit experiment with atoms: A simple atom interferometer," Phys. Rev. Lett. **66**, 2689–2692 (1991).

[33] M. Kasevich and S. Chu, "Atomic interferometry using stimulated Raman transitions," Phys. Rev. Lett. **67**, 181–184 (1991).

[34] M. J. Snadden, J. M. McGuirk, P. Bouyer, K. G. Haritos, and M. A. Kasevich, "Measurement of the Earth's Gravity Gradient with an Atom Interferometer-Based Gravity Gradiometer," Phys. Rev. Lett. **81**, 971–974 (1998).

[35] R. H. Parker, C. Yu, W. Zhong, B. Estey, and H. Müller, "Measurement of the fine-structure constant as a test of the Standard Model," Science **360**, 191–195 (2018).

[36] A. D. Cronin, J. Schmiedmayer, and D. E. Pritchard, "Optics and interferometry with atoms and molecules," Rev. Mod. Phys. **81**, 1051–1129 (2009).

[37] M. Zimmermann, "Interference of matter waves: branch-dependent dynamics, the Kennard phase, and T^3 Stern-Gerlach interferometry," Ph.D. thesis, Universität Ulm (2021).

[38] W. Gerlach and O. Stern, "The experimental proof of directional quantization in the magnetic field," Z. Physik **9**, 349–352 (1922).

[39] D. Bohm, *Quantum Theory* (Englewood Cliffs, N.J. : Prentice-Hall, 1951), pp. 604–605.

[40] B. G. Englert, J. Schwinger, and M. O. Scully, "Is spin coherence like Humpty-Dumpty? I. Simplified treatment," Found. Phys. **18**, 1045–1056 (1988).

[41] J. Schwinger, M. O. Scully, and B. G. Englert, "Is spin coherence like Humpty-Dumpty? - II. General theory," Z. Phys. D **10**, 135–144 (1988).

[42] M. O. Scully, B. G. Englert, and J. Schwinger, "Spin coherence and Humpty-Dumpty. III. the effects of observation," Phys. Rev. A **40**, 1775–1784 (1989).

[43] S. Machluf, Y. Japha, and R. Folman, "Coherent Stern-Gerlach momentum splitting on an atom chip," Nature Commun. **4**, 2424 (2013).

[44] Y. Margalit, Z. Zhou, S. Machluf, Y. Japha, S. Moukouri, and R. Folman, "Analysis of a high-stability Stern-Gerlach spatial fringe interferometer," New J. Phys. **21**, 073040 (2019).

[45] Y. Margalit, "Stern-Gerlach Interferometry with Ultracold Atoms," Ph.D. thesis, Ben-Gurion University of the Negev (2018).

[46] Y. Margalit, Z. Zhou, S. Machluf, D. Rohrlich, Y. Japha, and R. Folman, "A self-interfering clock as a "which path" witness," Science **349**, 1205–1208 (2015).

[47] Z. Zhou, Y. Margalit, D. Rohrlich, Y. Japha, and R. Folman, "Quantum complementarity of clocks in the context of general relativity," Class. Quantum Grav. **35**, 185003 (2018).

[48] B.-G. Englert, "Fringe Visibility and Which-Way Information: An Inequality," Phys. Rev. Lett. **77**, 2154–2157 (1996).

[49] Z. Zhou, Y. Margalit, S. Moukouri, Y. Meir, and R. Folman, "An experimental test of the geodesic rule proposition for the noncyclic geometric phase," Sci. Adv. **6** (2020).

[50] H. J. Metcalf, "Laser cooling and trapping of atoms," J. Opt. Soc. Am. B **20** (2003).

[51] W. Ketterle and N. V. Druten, "Evaporative Cooling of Trapped Atoms," (Academic Press, 1996), pp. 181 – 236.

[52] T. David, "Magnetic interactions of ultra-cold atoms near surfaces," Ph.D. thesis, Ben-Gurion University of the Negev (2009).

[53] S. Machluf, "Building a BEC on an atom chip apparatus," Master's thesis, Ben-Gurion University of the Negev (2009).

[54] O. Amit, "Matter-Wave Interferometry on an Atom Chip," Ph.D. thesis, Ben-Gurion University of the Negev (2020).

[55] Y. Margalit, Z. Zhou, O. Dobkowski, Y. Japha, D. Rohrlich, S. Moukouri, and R. Folman, "Realization of a complete Stern-Gerlach interferometer," arXiv:1801.02708 (2018).

[56] Y. Japha, "Unified model of matter-wave-packet evolution and application to spatial coherence of atom interferometers," Phys. Rev. A **104**, 053310 (2021).

[57] M. Meister, S. Arnold, D. Moll, M. Eckart, E. Kajari, M. A. Efremov, R. Walser, and W. P. Schleich, "Efficient Description of Bose–Einstein Condensates in Time-Dependent Rotating Traps," in "Advances in atomic, molecular, and optical physics," , vol. 66 (Elsevier, 2017), pp. 375–438.

[58] Y. Castin and R. Dum, "Bose-Einstein Condensates in Time Dependent Traps," Phys. Rev. Lett. **77**, 5315–5319 (1996).

[59] O. Dobkowski, "Coherence in the Stern-Gerlach Interferometer," Master's thesis (2020).

[60] C. Overstreet, P. Asenbaum, and M. A. Kasevich, "Physically significant phase shifts in matter-wave interferometry," Am. J. Phys. **89**, 324–332 (2021).

[61] K. Bongs, R. Launay, and M. A. Kasevich, "High-order inertial phase shifts for time-domain atom interferometers," Appl. Phys. B **84**, 599–602 (2006).

[62] J.-F. Schaff, T. Langen, and J. Schmiedmayer, "Interferometry with atoms," Riv. Nuovo Cimento (3) **37**, 509–589 (2014).

[63] M. Zimmermann, M. A. Efremov, W. Zeller, W. P. Schleich, J. P. Davis, and F. A. Narducci, "Representation-free description of atom interferometers in time-dependent linear potentials," New J. Phys. **21**, 073031 (2019).

[64] V. Dugrain, P. Rosenbusch, and J. Reichel, "Alkali vapor pressure modulation on the 100 ms scale in a single-cell vacuum system for cold atom experiments," Rev. Sci. Instrum. **85** (2014).

[65] C. Klempt, T. Van Zoest, T. Henninger, E. Rasel, W. Ertmer, J. Arlt *et al.*, "Ultraviolet light-induced atom desorption for large rubidium and potassium magneto-optical traps," Phys. Rev. A **73**, 013410 (2006).

[66] L. Torralbo-Campo, G. D. Bruce, G. Smirne, and D. Cassettari, "Light-induced atomic desorption in a compact system for ultracold atoms," Sci. Rep. **5**, 14729 (2015).

[67] H. Ammann and N. Christensen, "Delta Kick Cooling: A New Method for Cooling Atoms," Phys. Rev. Lett. **78**, 2088–2091 (1997).

[68] D. A. Smith, A. S. Arnold, M. J. Pritchard, and I. G. Hughes, "Experimental single-impulse magnetic focusing of launched cold atoms," J. Phys. B. **41**, 125302 (2008).

[69] H. Müntinga, H. Ahlers, M. Krutzik, A. Wenzlawski, S. Arnold, D. Becker, K. Bongs, H. Dittus, H. Duncker, N. Gaaloul, C. Gherasim, E. Giese, C. Grzeschik, T. W. Hänsch, O. Hellmig, W. Herr, S. Herrmann, E. Kajari, S. Kleinert, C. Lämmerzahl, W. Lewoczko-Adamczyk, J. Malcolm, N. Meyer, R. Nolte, A. Peters, M. Popp, J. Reichel, A. Roura, J. Rudolph, M. Schiemangk, M. Schneider, S. T. Seidel, K. Sengstock, V. Tamma, T. Valenzuela, A. Vogel, R. Walser, T. Wendrich, P. Windpassinger, W. Zeller, T. van Zoest, W. Ertmer, W. P. Schleich, and E. M. Rasel, "Interferometry with Bose-Einstein Condensates in Microgravity," Phys. Rev. Lett. **110**, 093602 (2013).

[70] T. Kovachy, J. M. Hogan, A. Sugarbaker, S. M. Dickerson, C. A. Donnelly, C. Overstreet, and M. A. Kasevich, "Matter wave lensing to picokelvin temperatures," Phys. Rev. Lett. **114**, 143004 (2015).

[71] C. Deppner, W. Herr, M. Cornelius, P. Stromberger, T. Sternke, C. Grzeschik, A. Grote, J. Rudolph, S. Herrmann, M. Krutzik *et al.*,

"Collective-mode enhanced matter-wave optics," Phys. Rev. Lett. **127**, 100401 (2021).

[72] N. Gaaloul, M. Meister, R. Corgier, A. Pichery, P. Boegel, W. Herr, H. Ahlers, E. Charron, J. R. Williams, R. J. Thompson, W. P. Schleich, E. M. Rasel, and N. P. Bigelow, "A space-based quantum gas laboratory at picokelvin energy scales," Nat. Commun. **13**, 7889 (2022).

[73] S. Myrskog, J. Fox, H. Moon, J. Kim, and A. Steinberg, "Modified "δ-kick cooling" using magnetic field gradients," Phys. Rev. A **61**, 053412 (2000).

[74] S. Kanthak, M. Gebbe, M. Gersemann, S. Abend, E. M. Rasel, and M. Krutzik, "Time-domain optics for atomic quantum matter," New J. Phys. **23**, 093002 (2021).

[75] E. Maréchal, S. Guibal, J.-L. Bossennec, R. Barbé, J.-C. Keller, and O. Gorceix, "Longitudinal focusing of an atomic cloud using pulsed magnetic forces," Phys. Rev. A **59**, 4636 (1999).

[76] L. Dupays, D. C. Spierings, A. M. Steinberg, and A. del Campo, "Delta-kick cooling, time-optimal control of scale-invariant dynamics, and shortcuts to adiabaticity assisted by kicks," Phys. Rev. Res. **3**, 033261 (2021).

[77] S. Machluf, "Coherent Splitting of Matter-Waves on an Atom Chip Using a State-Dependent Magnetic Potential," Ph.D. thesis, Ben-Gurion University of the Negev (2013).

[78] J. Schoser, A. Batär, R. Löw, V. Schweikhard, A. Grabowski, Y. B. Ovchinnikov, and T. Pfau, "Intense source of cold Rb atoms from a pure two-dimensional magneto-optical trap," Phys. Rev. A **66**, 023410 (2002).

[79] K. Dieckmann, R. Spreeuw, M. Weidemüller, and J. Walraven, "Two-dimensional magneto-optical trap as a source of slow atoms," Phys. Rev. A **58**, 3891 (1998).

[80] B. Trok, "Cold Atoms on an Atom Chip," Master's thesis, Ben-Gurion University of the Negev (2024).

[81] J. Rudolph, "Matter-wave optics with Bose-Einstein condensates in microgravity," Ph.D. thesis (2016).

[82] D. A. Steck, "Rubidium 87 D Line Data," (2010).

[83] "Rolling shutter, global shutter ; two principles of exposure," https://www.baumer.com/int/en/service-support/technical-information-industrial-cameras/rolling-shutter-global-shutter-two-principles-of-exposure-/a/rolling-shutter-global-shutter.

[84] SmarterEveryDay, "Why Do Cameras Do This? — Rolling Shutter Explained," https://www.youtube.com/watch?v=dNVtMmLlnoE (2017).

[85] S. J. Park, J. Noh, and J. Mun, "Cold atomic beam from a two-dimensional magneto-optical trap with two-color pushing laser beams," Opt. Commun. **285**, 3950–3954 (2012).

[86] J. Rudolph, W. Herr, C. Grzeschik, T. Sternke, A. Grote, M. Popp, D. Becker, H. Müntinga, H. Ahlers, A. Peters, C. Lämmerzahl, K. Sengstock, N. Gaaloul, W. Ertmer, and E. M. Rasel, "A high-flux BEC source for mobile atom interferometers," New J. Phys. **17**, 065001 (2015).

[87] D. M. Farkas, E. A. Salim, and J. Ramirez-Serrano, "Production of Rubidium Bose-Einstein Condensates at a 1 Hz Rate," arXiv:1403.4641 (2014).

[88] C. G. Darwin, "Free motion in the wave mechanics," Proc. R. Soc. London A. **117**, 258–293 (1927).

[89] E. H. Kennard, "Zur Quantenmechanik einfacher Bewegungstypen," Zeitschrift für Physik **44**, 326–352 (1927).

[90] E. H. Kennard, "The quantum mechanics of an electron or other particle," J. Franklin Inst. **207**, 47–78 (1929).

[91] D. M. Greenberger and A. W. Overhauser, "Coherence effects in neutron diffraction and gravity experiments," Rev. Mod. Phys. **51**, 43–78 (1979).

[92] H. Beyer and J. Nitsch, "The non-relativistic cow experiment in the uniformly accelerated reference frame," Phys. Lett. B **182**, 211–215 (1986).

[93] R. Penrose, "Black holes, quantum theory and cosmology," in "Journal of Physics: Conference Series," , vol. 174 (IOP Publishing, 2009), vol. 174, p. 012001.

[94] R. Penrose, "On the gravitization of quantum mechanics 1: Quantum state reduction," Found. Phys. **44**, 557–575 (2014).

[95] M. Zimmermann, M. A. Efremov, A. Roura, W. P. Schleich, S. A. DeSavage, J. P. Davis, A. Srinivasan, F. A. Narducci, S. A. Werner, and E. M. Rasel, "T3-Interferometer for atoms," Appl. Phys. B **123**, 102 (2017).

[96] C. J. Eliezer and P. G. Leach, "The equivalence principle and quantum mechanics," Am. J. Phys. **45**, 1218 (1977).

[97] G. Rosen, "Galilean Invariance and the General Covariance of Nonrelativistic Laws," Am. J. Phys. **40**, 683 (1972).

[98] D. M. Greenberger, "Some remarks on the extended Galilean transformation," Am. J. Phys. **47**, 35 (1979).

[99] C. Lämmerzahl, "On the equivalence principle in quantum theory," Gen. Relat. Gravit. **28**, 1043 (1996).

[100] L. Viola and R. Onofrio, "Testing the equivalence principle through freely falling quantum objects," Phys. Rev. D **55**, 455 (1997).

[101] T. Kovachy, P. Asenbaum, C. Overstreet, C. A. Donnelly, S. M. Dickerson, A. Sugarbaker, J. M. Hogan, and M. A. Kasevich, "Quantum superposition at the half-metre scale," Nature **528**, 530–533 (2015).

[102] V. Xu, M. Jaffe, C. D. Panda, S. L. Kristensen, L. W. Clark, and H. Müller, "Probing gravity by holding atoms for 20 seconds," Science **366**, 745 (2019).

[103] K. A. Krzyzanowska, J. Ferreras, C. Ryu, E. C. Samson, and M. G. Boshier, "Matter-wave analog of a fiber-optic gyroscope," Phys. Rev. A **108**, 043305 (2023).

[104] J. Henry, "Galileo and the scientific revolution: The importance of his kinematics," Galilaeana: journal of Galilean studies: VIII, 2011 pp. 3–36 (2011).

[105] R. Colella, A. W. Overhauser, and S. A. Werner, "Observation of Gravitationally Induced Quantum Interference," Phys. Rev. Lett. **34**, 1472–1474 (1975).

[106] U. Bonse and T. Wroblewski, "Measurement of Neutron Quantum Interference in Noninertial Frames," Phys. Rev. Lett. **51**, 1401 (1983).

[107] A. Peters, K. Y. Chung, and S. Chu, "High-precision gravity measurements using atom interferometry," Metrologia **38**, 25 (2001).

[108] J. B. Fixler, G. T. Foster, J. M. McGuirk, and M. A. Kasevich, "Atom Interferometer Measurement of the Newtonian Constant of Gravity," Science **315**, 74 (2007).

[109] G. Rosi, G. D'Amico, L. Cacciapuoti, F. Sorrentino, M. Prevedelli, M. Zych, Č. Brukner, and G. M. Tino, "Quantum test of the equivalence principle for atoms in coherent superposition of internal energy states," Nat. Commun. **8**, 15529 (2017).

[110] G. M. Tino, "Testing gravity with cold atom interferometry: results and prospects," Quantum Sci. Technol. **6**, 024014 (2021).

[111] C. D. Panda, M. J. Tao, M. Ceja, J. Khoury, G. M. Tino, and H. Müller, "Measuring gravitational attraction with a lattice atom interferometer," Nature **631**, 515 (2024).

[112] G. D. McDonald, C. C. N. Kuhn, S. Bennetts, J. E. Debs, K. S. Hardman, J. D. Close, and N. P. Robins, "A faster scaling in acceleration-sensitive atom interferometers," Europhys. Lett. **105**, 63001 (2014).

[113] I. Dutta, D. Savoie, B. Fang, B. Venon, C. L. G. Alzar, R. Geiger, and A. Landragin, "Continuous Cold-Atom Inertial Sensor with 1 nrad/sec Rotation Stability," Phys. Rev. Lett. **116**, 183003 (2016).

[114] O. Amit, Y. Margalit, O. Dobkowski, Z. Zhou, Y. Japha, M. Zimmermann, M. A. Efremov, F. A. Narducci, E. M. Rasel, W. P. Schleich, and R. Fol-

man, "T^3 Stern-Gerlach matter-wave interferometer," Phys. Rev. Lett. **123**, 083601 (2019).

[115] G. G. Rozenman, M. Zimmermann, M. A. Efremov, W. P. Schleich, L. Shemer, and A. Arie, "Amplitude and Phase of Wave Packets in a Linear Potential," Phys. Rev. Lett. **122**, 124302 (2019).

[116] C. Bordé, "Atomic interferometry with internal state labelling," Phys. Lett. A **140**, 10–12 (1989).

[117] S. Loriani, A. Friedrich, C. Ufrecht, F. D. Pumpo, S. Kleinert, S. Abend, N. Gaaloul, C. Meiners, C. Schubert, D. Tell, Étienne Wodey, M. Zych, W. Ertmer, A. Roura, D. Schlippert, W. P. Schleich, E. M. Rasel, and E. Giese, "Interference of clocks: A quantum twin paradox," Sci. Adv. **5**, eaax8966 (2019).

[118] F. Hammad, P. Sadeghi, N. Fleury, and A. Leblanc, "Fresh look at the effects of gravitational tidal forces on a freely-falling quantum particle," Int. J. Mod. Phys. D **31**, 2150121 (2022).

[119] F. Di Pumpo, A. Friedrich, C. Ufrecht, and E. Giese, "Universality-of-clock-rates test using atom interferometry with T^3 scaling," Phys. Rev. D **107**, 064007 (2023).

[120] K. A. Whittaker, J. Keaveney, I. G. Hughes, and C. S. Adams, "Hilbert transform: Applications to atomic spectra," Phys. Rev. A **91**, 032513 (2015).

[121] G. G. Rozenman, M. Zimmermann, M. A. Efremov, W. P. Schleich, W. B. Case, D. M. Greenberger, L. Shemer, and A. Arie, "Projectile motion of surface gravity water wave packets: An analogy to quantum mechanics," Eur. Phys. J. Special Topics **230**, 931–935 (2021).

[122] M. Akhlaghi and T. Ichikawa, "Noise based detection and segmentation of nebulous objects," Astrophys. J. Suppl. Ser. **220**, 1 (2015).

השבב האטומי מהווה את ליבת הניסוי, השבב מורכב מחוטים נושאי זרם אשר יוצרו בתהליכי ננו-פבריקציה. השבב האטומי מאפשר שליטה מהירה ומדויקת בשדות המגנטיים ומשרת שתי מטרות. הראשונה, אפנון מהיר ומדויק של הגרדיאנטים המגנטיים הדרושים לניסוי. שנית, הוא מאפשר הכנה מדויקת של האטומים לניסוי, החל מלכידה יציבה, שחרור מבוקר ומהיר, ומיקוד של חבילת הגל האטומית לאחר שחרורה מהמלכודת.

אנחנו מקווים כי ניסוי חדש זה ותוצאותיו, יהוו כלי משמעותי בבחינה של הממשק בין תורת הקוונטים ותורת הכבידה. למשל, לאחרונה הועלתה ההיפותזה כי הפאזה הנ"ל מהווה ביטוי של עקרון השקילות בתורת הקוונטים, והוצעה גם ככלי לבחינת כבידה קוונטית. בנוסף לתוצאות המדידה, אנו מקווים כי ההצגה של ניסוי חדש זה תהווה בסיס לחקר של שאלות יסודיות.

מבנה התזה להלן

פרק 1: מבוא לאינטרפרומטרים של גלי חומר, ולאינטרפרומטר שטרן-גרלך.

פרק 2: רקע תיאורטי לאינטרפרומטר שטרן-גרלך וטכניקות הניסוי.

פרק 3: תיאור של מערך הניסוי, כולל השדרוגים שהוכנסו בו במהלך עבודת הדוקטורט.

פרק 4: תיאור של תהליך הניסוי ליצירת אטומים אולטרה-קרים ועיבוי בוז-איינשטיין.

פרק 5: התוצאה הראשית של עבודה זו – מדידה של הפאזה הקוונטית של חלקיק בנפילה חופשית.

פרק 6: תיאור מפורט של התוצאה הראשית – בהיבטים הניסויים והתיאורטיים שלה.

תקציר

המאמץ האנושי להבין את הטבע סביבנו ואת החוקים המתארים אותו הוא סיפור דרמה מרשים, שבו שזורים תופעות ואנשים כדמויות הראשיות. לא ניתן לספר את הסיפור הזה בלי להזכיר גופים בנפילה חופשית, בין אם זה כדור שהושלך, לכאורה, מהמגדל הנטוי של פיזה, או תפוח שנפל על ראשו של האדם שיגדיר מחדש את מדע הפיסיקה.

החקירות של גלילאו בנוגע לנפילה של גופים מהוות נקודת תפנית בחקר הכמותי של תנועה. חוק הכבידה של ניוטון מכניס לכפיפה אחת את התופעות הארציות של נפילת גופים, והתופעות השמיימיות של תנועת הכוכבים בשמים מעל ראשנו. שנים לאחר מכן, אלברט איינשטיין במאמציו להרחיב את תורת היחסות הפרטית לכדי תורה כללית, חווה פריצת דרך כאשר דמיין אדם בנפילה והבין כי אותו אדם לא ירגיש את משקלו. תובנה זו הובילה לניסוח של עקרון השקילות אשר עומד בבסיס תורת היחסות.

פרק דרמטי נוסף נגלל עם לידתה של תורת הקוונטים, החוזה כי לחלקיקים בעלי מסה ישנן גם תכונות גליות, וניתן לייחס להם אורך גל ולתארם בעזרת פונקציית הגל. התיאוריה חוזה כי אותם "גלי חומר" צפויים להציג את תופעת הסופרפוזיציה, שתוצאותיה הן התאבכות בונה והורסת כתלות בפאזה היחסית בין חלקי הסופרפוזיציה.

התופעה של התאבכות גלי חומר הודגמה לראשונה בשנת 1927 בניסויים שבהם נמדדה תבנית עקיפה של אלקטרונים על ידי תומפסון ורייד (עקיפה של קרן קתודית משכבה דקה), ודוויסון וגרמר (עקיפה של אלקטרונים מגביש ניקל). פיתוחים טכנולוגיים הובילו בהמשך ליצירה של אינטרפרומטר גלי חומר, בו גל חומר מפוצל לשתי קרניים קוהרנטיות, שלאחר מכן מאוחדות בחזרה לקרן אחת ויוצרות התאבכות. אינטרפרומטרים של גלי חומר, ובמיוחד אינטרפרומטרים אטומיים, אפשרו טווח רחב של יישומים טכנולוגיים וחקר של פיסיקה יסודית.

באופן מפתיע, למרות ההיסטוריה הארוכה של ניסויים בגלי חומר, והמאמצים המרובים לאחד את תורת היחסות ותורת הקוונטים, צבירת הפאזה הקוונטית של חלקיק בנפילה חופשית עוד לא נמדדה.

בעבודה זו אנו מציגים אינטרפרומטר אטומי חדשני אשר מודד את צבירת הפאזה של חלקיק בנפילה חופשית. האינטרפרומטר מבוסס על אפקט שטרן-גרלך, וממנף עשור של ניסויים באינטרפרומטריית שטרן-גרלך, בהן הטכניקות הנדרשות פותחו. האינטרפרומטר פועל עם אטומים אולטרה-קרים אשר מפוצלים באופן קוהרנטי לכדי סופרפוזיציה של נפילה חופשית ומנוחה, בעזרת שדות מגנטיים וגלי מיקרו.

העבודה נעשתה בהדרכת פרופסור רון פולמן

במחלקה לפיסיקה

בפקולטה למדעי הטבע

אינטרפרומטריית שטרן-גרלך בגלי חומר

מחקר לשם מילוי חלקי של הדרישות לקבלת תואר ״דוקטור לפילוסופיה״

מאת

אור דובקובסקי

הוגש לסינאט אוניברסיטת בן גוריון בנגב

אישור המנחה ______________________

אישור דיקן בית הספר ללימודי מחקר מתקדמים ע״ש קרייטמן
____

אדר תשפ״ה **מרץ 2025**

באר שבע

<u>אינטרפרומטריית שטרן-גרלך בגלי חומר</u>

מחקר לשם מילוי חלקי של הדרישות לקבלת תואר "דוקטור לפילוסופיה"

מאת

אור דובקובסקי

הוגש לסינאט אוניברסיטת בן גוריון בנגב

אדר תשפ"ה מרץ 2025

באר שבע